Development of a microgel-based extracellular vesicle delivery system for heart repair

Camille Marijon

Submitted in accordance with the requirements
for the degree of Doctor of Philosophy and
Diploma of Imperial College London

Imperial College London
Department of Materials

October 2019

Declaration of originality

This is to declare that:

I. The work included in this thesis was performed by myself unless otherwise stated;

II. Any collaborators who performed experiments or data analysis have been acknowledged;

III. All the published works that have provided information for the development of this thesis have been listed in the references;

IV. The work reported in this thesis was performed at Imperial College London (UK).

Camille Marijon

Copyright declaration

The copyright of this thesis rests with the author and is made available under a Creative Commons Attribution Non-Commercial No Derivatives licence. Researchers are free to copy, distribute or transmit the thesis on the condition that they attribute it, that they do not use it for commercial purposes and that they do not alter, transform or build upon it. For any reuse or redistribution, researchers must make clear to others the licence terms of this work.

Abstract

Cardiovascular diseases are the primary cause of death globally, responsible for approximately 17.5 million deaths per year. In particular, myocardial infarction caused by the obstruction of a coronary artery can lead to heart failure. A growing number of studies have demonstrated that extracellular vesicles (EVs) exhibit great potential as cell-free cardioprotective agents, which could overcome many of the technical, ethical and regulatory hurdles associated with cell-based therapies. However, the beneficial effects of administered EVs are short-lived; a major limitation that could be circumvented using a material-based approach for increased retention and sustained release. Therefore, the main objective of this study was to develop a translational approach for repairing the infarcted heart, in the form of injectable, 'off-the-shelf' EV-loaded synthetic microgels. This platform was designed to improve EV stability and retention time at the site of administration, with sustained and environmentally-responsive release of EVs to the surrounding damaged tissue. Methods for fabricating monodisperse environmentally-sensitive microgels using a microfluidic-based platform were developed, and a first proof-of-concept of the feasibility of loading and releasing EVs from the microgels was demonstrated *in vitro* and *in vivo*.

Acknowledgements

First, I would like to thank my supervisor Prof. Molly Stevens for welcoming me in her group, giving me the opportunity to learn as a scientist and grow as a person, and providing me with such a dynamic and resourceful environment. And I would like to thank her for the support she gave me when I needed it the most. I am also very grateful for the support I had from my second supervisor, Prof. Sian Harding, and for the precious help of my close collaborator Dr. Daniel Stuckey (University College London). I would like to thank my previous supervisor and mentor, Prof. Philippe Menasché, for being such a source of inspiration and for always supporting me. Finally I would also like to thank the UK Regenerative Medicine Platform, the Rosetrees Trust, Armourers and Brasiers and Imperial College London for supporting my work in the last four years.

I would not have been able to do this work without the incredible support from three amazing postdoctoral researchers. I would like to deeply thank Dr. James Armstrong, who truly is a super postdoc, Dr. Stacey Skaalure for always understanding me so well, and Dr. Ioanna Mylonaki for being the only one to understand my obsession with pharmaceutical sciences. I am extremely grateful for all the support they gave me in the lab, in the office and outside of work. I have no words to express how much it meant to me.

I would like to thank all the former and present members of the support team I was lucky to work with in the group: Sabrina Skeete, Alexander Kirby, Melissa Chee, Dr. Benjamin Pierce, Dr. Akemi Nogiwa Valdez, Brittany Rae, Sirli Threumuth, Dr. Thomas Whittaker, Chloe Stockford, Maria João Cruz and Anna Wilhelme. Also, a special thanks to all the people who contributed to my project, Michele Becce for the photolithography, Dr. Adrian Najer for the FCS, Dr. James Armstrong for the confocal fluorescence microscopy, and Jelle Penders and Dr. Qu Chen for the HPF-FS and FIB-SEM. A special thanks also goes to all the people who trusted me with their *in vivo* experiments: Dr. Michaella Kapnisi, Dr. Paola Campagnolo, Dr. Limor Zwi Dantsis and Dr. Stacey Skaalure.

I would like to thank my lovely friends and colleagues for the Stevens' group. Bakul, for all the amazing moments we had and will have together. Maria João for being such a kind and funny human being. Liliana, for her never-ending energy and generosity. Lucia, for being such a lovely person and friend. Raya, for being so helpful and kindhearted. The Italian team, Valeria, Arianna and Alessandra, and also Joyce for all the good moments spent together. The G02C office, which will always be the best office. And my late night buddies, Isaac, Carolyn and Eunjung. Thanks to all the people in all the whatsapp groups I was a part of because I always want to do more stuff together: the Pizza group, No time for coffee (formerly: Coffee?), Climbing, Stevens Social Cycle Club and the Stevens boardgamers. Cheers to all the amazing memories of the trips to Madeira, India, Greece and the USA. And to all the good moments with my friends at lunchtime in the iarea, at Union and Metric and during all four group weekends.

Finally I would like to thank my family, especially my mum, dad and sister who I love very very very much, and all friends from France and Belgium. I cannot wait to spend more time with them!

Publications

Microgel-based extracellular vesicle delivery platform for heart repair.

Marijon C *et al.*

Manuscript in preparation.

Nanoneedle-based integrative gene transfer for epicardial reprogramming.

Campagnolo P, Leonardo V, Brito L, Marijon C, Smart N, Becce M, Sala-Newby G, Mansfield C, Harding SE, Chiappini C, Stevens MM.

Manuscript in preparation.

Near-infrared bioluminescent extracellular vesicles for monitoring controlled release from biodegradable hydrogels.

Skaalure SC, El-Laham R, Marijon C, Nagelkerke A, Whittaker T, Kühn S, Kauscher U, Nele V, Stuckey DJ, Stevens MM.

Manuscript in preparation.

Remote magnetic nanoparticle manipulation enables the dynamic patterning of cardiac tissues.

Zwi-Dantsis L, Wang B, Marijon C, Zonetti S, Ferrini A, Massi L, Stuckey DJ, Terracciano CM, Stevens MM.

Under revision for Advanced Materials.

Microgel-based extracellular vesicle delivery platform for the treatment of myocardial infarction.

Marijon C, Armstrong JPK, Skaalure SC, Mylonaki I, El Laham R, Stuckey DJ, Harding SE, Stevens MM.

Conference abstract for poster presentation at BioMedEng19.

Development of a microgel-based extracellular vesicle delivery system for heart repair.

Marijon C, Armstrong JPK, Skaalure SC, Mylonaki I, El Laham R, Stuckey DJ, Harding SE, Stevens MM.

Conference abstract for poster presentation at TERMIS EU 2019. Third poster prize.

Development of a microgel-based extracellular vesicle delivery system for heart repair.

Marijon C, Armstrong JPK, Skaalure SC, Mylonaki I, Harding SE, Stevens MM.

Conference abstract for presentation at FIRM symposium 2018.

Auxetic cardiac patches with tunable mechanical and conductive properties toward treating myocardial infarction.

Kapnisi M, Mansfield C, Marijon C, Guex AG, Perbellini F, Bardi I, Humphrey EJ, Puetzer JL, Mawad D, Koutsogeorgis DC, Stuckey DJ, Terracciano CM, Harding SE, Stevens MM.

Advanced Functional Materials. 2018 May 24; 28(21): 1800618.

Table of contents

DECLARATION OF ORIGINALITY 2

COPYRIGHT DECLARATION 2

ABSTRACT 3

ACKNOWLEDGEMENTS 4

PUBLICATIONS 6

TABLE OF CONTENTS 7

LIST OF TABLES 11

LIST OF FIGURES 12

LIST OF ABBREVIATIONS 15

CHAPTER 1 LITERATURE REVIEW 17

1. Myocardial infarction and heart repair 18
1.1. From atherosclerosis to myocardial infarction 18
1.1.1. Epidemiology 18
1.1.2. Atherosclerosis 19
1.1.3. Myocardial infarction 21
1.2. Unmet therapeutic need 23
1.2.1. Current therapeutic strategies 23
1.2.2. Biological medicinal products 25
1.2.3. Delivery challenges for heart regeneration 27
2. Extracellular vesicles as therapeutics 31
2.1. Definition and physiological role of extracellular vesicles 31
2.1.1. Paracrine effect vs cell integration 31
2.1.2. EVs as new therapeutic tools 32
2.2. EV production and characterisation 34
2.2.1. EV isolation and purification 34
2.2.2. EV characterisation 36
2.3. EVs for cardiac repair 38
2.3.1. Cardioprotective EVs 38

2.3.2. Current limitations of EV-based therapies 40
3. Hydrogels for drug delivery in cardiac repair 42
3.1. Hydrogel definition and advantages in drug delivery 42
3.2. Hydrogels in cardiac repair 43
3.2.1. Polymers used for heart delivery 43
3.2.2. PEG-based hydrogels 44
3.2.3. Degradable hydrogels for drug delivery 47
3.2.4. Drug loading and release from hydrogels 49
3.3. Microgels for heart delivery 51
3.3.1. Hydrogel delivery approaches for cardiac repair 51
3.3.2. Microgel fabrication processes 53
3.3.3. Microgels for drug delivery in heart repair 55

CHAPTER 2 MICROFLUIDIC PLATFORM FOR THE FABRICATION OF MONODISPERSE INJECTABLE PEG MICROGELS 58

1. Introduction 59
2. Materials and methods 61
2.1. Materials 61
2.2. Methods 61
2.2.1. Mould fabrication using 3D printing (mould v.1) 61
2.2.2. Mould fabrication using photolithography (mould v.2) 62
2.2.3. Chip fabrication using soft lithography 62
2.2.4. Preparation of oil and aqueous phases 63
2.2.5. Microgel fabrication using type-2 chips 65
2.2.6. Microgel phase transfer 67
2.2.7. Injectability 67
3. Results and discussion 69
3.1. Fabrication of mould v.1 and type-1 chips 69
3.2. Fabrication of mould v.2 and type-2 chips 71
3.3. Microgel fabrication 72
3.3.1. Microdroplet generation 72
3.3.2. Microdroplet stabilisation and crosslinking into microgels 75
3.3.3. Microgel fabrication process reproducibility 78
3.4. Validation of microgel washing and phase transfer 78
3.5. Injectability 80
4. Conclusions 81

CHAPTER 3 MMP-SENSITIVE MICROGELS FOR ENVIRONMENTALLY-RESPONSIVE DEGRADATION 83

1. Introduction 84

2. Materials and methods 86
2.1. Materials 86
2.2. Methods 86
2.2.1. Peptide crosslinker: synthesis, purification and characterisation 86
2.2.2. Optimisation of the hydrogel precursor buffer composition 88
2.2.3. Hydrogel characterisation: swelling ratio, crosslinking density and mesh size 89
2.2.4. Microgel preparation, size analysis and storage 91
2.2.5. Microgel cytotoxicity 91
2.2.6. Trypsin and MMP-9-mediated microgel degradation 92
2.2.7. Statistical analysis 94
3. Results and discussion 95
3.1. MMP-2/9 degradable crosslinker synthesis and characterisation 95
3.1.1. Degradable peptide crosslinker synthesis and characterisation 95
3.1.2. Peptide crosslinker degradation by MMP-2/9 96
3.1.3. Buffer optimisation and validation 97
3.1.4. Hydrogel characterisation 99
3.2. Microgel characterisation 101
3.2.1. Microgel size and stability 101
3.2.2. Microgel cytotoxicity 103
3.3. Microgel degradation 106
3.3.1. Trypsin-mediated degradation 106
3.3.2. MMP-9-mediated degradation 110
4. Conclusion 112

CHAPTER 4 ENVIRONMENT-SENSITIVE MICROGELS FOR EV DELIVERY: A PROOF OF CONCEPT 114

1. Introduction 115
2. Materials and methods 117
2.1. Materials 117
2.2. Methods 117
2.2.1. EV purification and characterisation 117
2.2.2. DiD-labelled EV production and characterisation 119
2.2.3. EV uptake 120
2.2.4. EV-loading into patches and microgels 122
2.2.5. EV release and uptake 124
2.2.6. In vivo experiments 124
2.2.7. Statistical analysis 125
3. Results and discussion 126
3.1. DiD-EV preparation and characterisation 126
3.1.1. EV characterisation 126

3.1.2. DiD-EV labelling 127
3.1.3. DiD-labelled EV uptake 129
3.2. DiD-EV loading into microgels 131
3.2.1. EV loading capacity 131
3.2.2. EV-loading into microgels 132
3.2.3. EV release and uptake 135
3.2.4. DiD-labelled EV detection in vivo 139
3.2.5. In vivo evaluation of EV retention using microgels 140
4. Conclusion 144

CHAPTER 5 CONCLUSIONS AND FUTURE WORK 146

REFERENCES 151

List of tables

Chapter 1

Table 1: Phases of cardiac healing and remodelling following a myocardial infarction.

Table 2: Current therapeutic strategies for myocardial infarction.

Table 3: Main cell types used in clinical trials for heart repair.

Table 4: Percutaneous catheter-based intramyocardial injection systems available on the market.

Table 5: EV classification depending on their origin.

Table 6: Preclinical studies using cardiac-committed cell-derived EV.

Table 7: List of completed clinical trials with published results using natural-based hydrogels alone or as a delivery system for heart repair.

Table 8: Preclinical studies using injectable microgels as drug delivery systems for heart repair.

Chapter 3

Table 9: Table of constants used to calculate the swelling ratio, crosslinking density and mesh size.

Table 10: Decreased hydrogel precursors reactivity over time using the initial buffer.

Table 11: Buffer optimisation.

List of figures

Chapter 1

Figure 1: First cause of death by country.

Figure 2: Stages of atherosclerosis.

Figure 3: Heart anatomy and vascularisation.

Figure 4: Delivery routes for targeting the heart.

Figure 5: EV types and biogenesis and internalisation mechanisms.

Figure 6: Main methods used for EV isolation and purification.

Figure 7: Michael addition-mediated thiol-ene reaction.

Figure 8: Examples of degradable moieties used in hydrogel-based drug delivery systems.

Figure 9: Drug loading and release mechanisms.

Figure 10: Hydrogel delivery approaches.

Figure 11: Main methods used for microgel fabrication.

Chapter 2

Figure 12: Types of microfluidic droplet generation junctions used for the preparation of water-in-oil microemulsions.

Figure 13: Microfluidic chip fabrication using soft lithography.

Figure 14: Microfluidic-based microgel fabrication platform.

Figure 15: Microgel washing protocol.

Figure 16: Type-1 chip design.

Figure 17: Type-1 mould and chip fabrication.

Figure 18: Type-2 chip design.

Figure 19: Type-2 mould and chip fabrication.

Figure 20: Optimisation of microdroplet generation.

Figure 21: Optimisation of the outlet tubing length and Span® 80 concentration.

Figure 22: Reproducible microgel fabrication.

Figure 23: Validation of microgel washing and phase transfer.

Figure 24: Injectability of the 10% (v/v) microgel suspension.

Chapter 3

Figure 25: MMP-2/9-mediated degradation.

Figure 26: Peptide degradable crosslinker characterisation.

Figure 27: LC-MS spectra of the cleavage products formed by treating the peptide crosslinker with MMP-2 and -9.

Figure 28: Validation of the new set of buffers.

Figure 29: Estimations of swelling ratio Q, crosslinking density and mesh size.

Figure 30: Microgel stability during storage.

Figure 31: Microgel cytotoxicity.

Figure 32: Microgel degradation using a high concentration of trypsin.

Figure 33: Microgel degradation using a range of nanomolar concentrations of trypsin.

Chapter 4

Figure 34: Microgel degradation using MMP-9.

Figure 35: Overview of the EV labelling using DiD, loading and release strategies.

Figure 36: Characterisation of the fractions obtained following SEC.

Figure 37: Evaluation of the effects of different parameters on the EV labelling and hydrodynamic diameter using FCS analysis.

Figure 38 : Evaluation of the effects of EV labelling and UF-based concentration on particle hydrodynamic diameter, concentration and labelling levels.

Figure 39: DiD-EV uptake by neonatal rat cardiac fibroblasts in culture.

Figure 40: Time sweep performed on crosslinking unloaded and EV-loaded hydrogels.

Figure 41: Confocal images of a non-degradable EV-loaded hydrogel patch, non-degradable unloaded microgels, degradable EV-loaded microgels and non-degradable EV-loaded microgels.

Figure 42: FIB-SEM images of non-degradable EV-loaded microgels.

Figure 43: Images of peptide-crosslinked EV-loaded hydrogels and microgels before and after trypsin-mediated degradation.

Figure 44: Analysis of the degradation products obtained from cc DiD-EV-loaded patches and microgels.

Figure 45: Evaluation of the degradation products obtained from cc DiD-EV-loaded hydrogels and microgels using the EV uptake assay.
Figure 46: *In vivo* tracking following the subcutaneous injection of different dosages of fluorescent cc DiD-EVs.
Figure 47: Subcutaneous injections of cc DiD-EVs and cc DiD-EV-loaded degradable microgels.

List of abbreviations

ACS = acute coronary syndrome

BCA = bicinchoninic acid

bFGF = basic fibroblast growth factor

BM-MNC = bone marrow-derived mononuclear cell

CDC = cardiosphere-derived cell

CPC = cardiac progenitor cell

CPP = counts per particle

Dh = hydrodynamic diameter

EB = enzyme buffer

ECG = electrocardiogram

ECM = extracellular matrix

EM = electron microscopy

EV = extracellular vesicle

FCS = fluorescence correlation spectroscopy

FFJ = flow-focusing junction

FIB-SEM = Focused Ion Beam milling combined with Scanning Electron Microscopy

FS = freeze substitution

GLP-1 = glucagon-like peptide-1

HPF = high-pressure freezing

HPLC = high-performance liquid chromatography

ID = inner diameter

IGF-1 = insulin-like growth factor-1

IHDs = ischemic heart diseases

IR = infrared

LAD = left anterior descending

LC = left circumflex

LC = liquid chromatography

LCA = left coronary artery

MALDI-TOF = matrix-assisted laser desorption/ionization time-of-flight

MI = myocardial infarction

MMP = matrix metalloproteinase

MS = mass spectrometry

MSC = mesenchymal stem cell

MW = molecular weight

NSTEMI = non-ST-elevation myocardial infarction

NTA = nanoparticle tracking analysis

OD = outter diameter

PDMS = polydimethylsiloxane

PEG = poly(ethylene glycol)

RCA = right coronary artery

RPS = resistive pulse sensing

RT = room temperature

SD = standard deviation

SEC = size exclusion chromatography

SMT = standard medical treatment

SPPS = solid phase peptide synthesis

STEMI = ST-elevation myocardial infarction

UF = ultrafiltration

UV = ultraviolet

VEGF = vascular endothelial growth factor

Chapter 1 Literature review

1. Myocardial infarction and heart repair

1.1. From atherosclerosis to myocardial infarction

1.1.1. Epidemiology

Cardiovascular diseases are the number one cause of death worldwide accounting for approximately 31% of global mortality rates [1] (Figure 1). Among them are ischemic heart diseases (IHDs), comprising a clinical spectrum that extends from myocardial infarction (MI) to end-stage heart failure. Despite medical advances that have led to an improvement in post-MI survival, IHDs are responsible for 7.4 million deaths every year and remain a major concern both from a public health and a financial perspective. IHDs are estimated to cost the European Union economy close to 60 billion euros every year, 32% of this amount being due to direct health care costs, 33% to productivity losses, and 35% to the informal care of patients with IHD [2]. Additionally, IHDs are starting to spread to developing countries [3] and continue to increase in incidence in more developed countries, mainly because of population ageing and the increasing prevalence of associated risk factors [4].

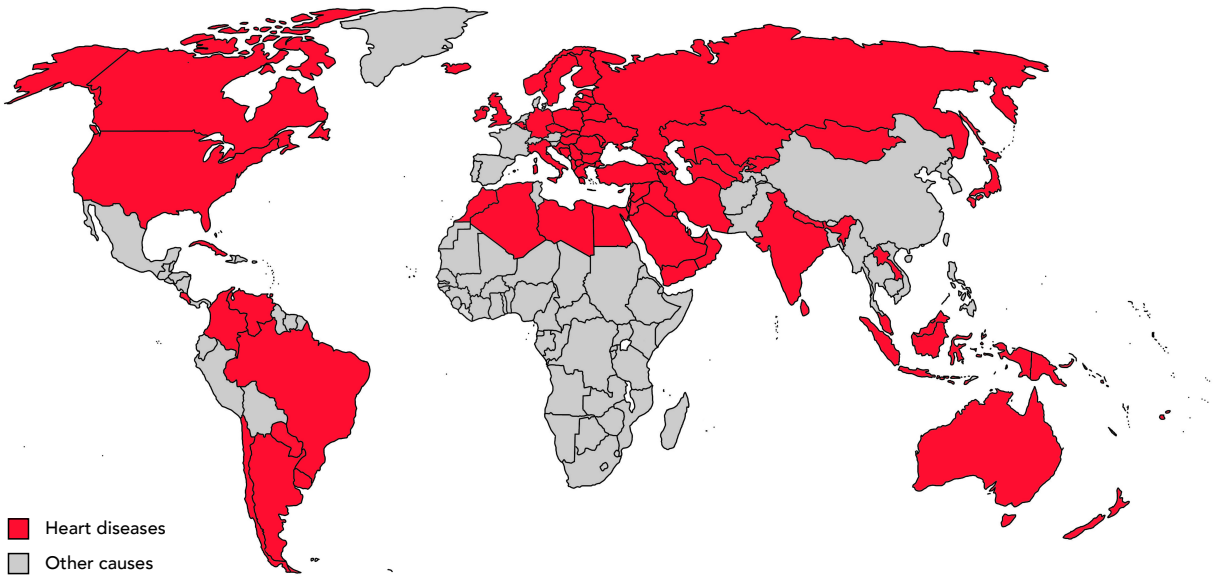
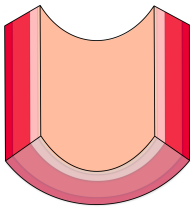


Figure 1: First cause of death by country. Heart diseases are the number one cause of death in countries coloured in red (map adapted from Simran Khosla, GlobalPost, 2014).

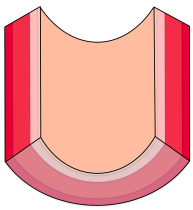
1.1.2. Atherosclerosis

In the vast majority of cases, the underlying cause of MI is atherosclerosis, a condition characterised by the excessive deposition of fatty material (also called atheroma or plaques) in the artery lining, leading to progressive vessel stiffening and lumen obstruction [5]. Atherosclerosis is strongly associated with the presence of cardiovascular risk factors, including non-modifiable risk factors (increasing age, male sex, heredity) and modifiable risk factors (smoking, obesity, sedentary lifestyle, hypertension, diabetes, dyslipidemia). In particular, high serum cholesterol levels have been shown to be strongly correlated with an increased risk of MI [6].

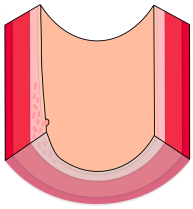
Atherosclerosis is the result of a phenomenon called endothelial dysfunction, in which the the functional phenotype of the endothelium that line the inside of the arteries is altered [7]. It affects predominantly large arteries in areas featuring a turbulent blood flow [8]. These include the coronary arteries in the heart, the femoral arteries in the lower limbs and the carotids irrigating the brain; leading to MI, peripheral artery disease and stroke, respectively. Such arteries, when healthy, contain three layers (Figure 2, top). The inner layer (the tunica intima) is composed of a monolayer of endothelial cells, or endothelium, on top of subendothelial connective tissue and the internal elastic membrane. The middle layer (the tunica media) contains smooth muscle cells and elastic fibres as well as the external elastic membrane. Finally, the outer layer (the tunica adventitia) comprises connective tissue as well as scattered macrophages, fibroblasts, nerves and microvessels. The different stages involved in progressive vessel obstruction, from the accumulation of lipoproteins in the intima to the rupture of a plaque, are described in Figure 2. Except for lesion types I to III, which are clinically silent, it is worth noting that although clinical manifestations and fatal outcomes of MI are most often found with type VI lesions (complicated plaque), there is actually no correlation between the phase and size of a lesion on one hand, and the degree of lumen obstruction and clinical manifestations on the other [9].



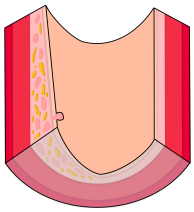
Healthy artery	Tunica intima: endothelial cells, connective tissue, internal elastic membrane Tunica media: smooth muscle cells, elastic fibres, external elastic membrane Tunica adventitia: connective tissue, scattered cells, nerves, microvessels



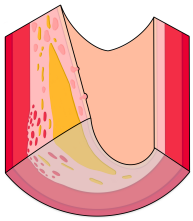
Stage I **"Initial lesion"** (from 1st decade)	Accumulation/oxidation of lipoproteins in the tunica intima Recruitment of monocytes, maturation into macrophages, phagocytosis of oxidised lipoproteins and formation of foam cells



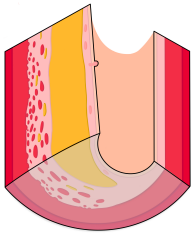
Stage II "Fatty streak"	Accumulation of foam cells and fatty streak formation Recruitment of T cells Migration of smooth muscle cells into the tunica intima and proliferation



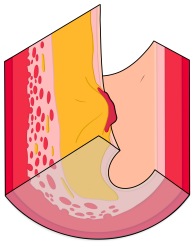
Stage III **"Intermediate lesion"** (from 3rd decade)	Increase in intracellular lipid accumulation Foam cell apoptosis, extracellular accumulation of lipids and formation of lipid pools



Stage IV **"Atheroma"**	Formation of lipid cores Stage IV lesions may evolve towards phase V/VI



Stage V **"Fibroatheroma"** (from 4th decade)	Accelerated recruitment and proliferation of smooth muscle cells Increase in synthesis of collagen and formation of a fibromuscular cap



Stage VI **"Complicated plaque"**	Plaque rupture (surface defect) Thrombosis and hematoma

Figure 2: Stages of atherosclerosis. Healthy arteries comprise three layers: the tunica intima, the tunica media and the tunica adventitia (top). Vessel obstruction is the result of an endothelial cell dysfunction that leads to the abnormal accumulation of lipoproteins, immune cells and smooth muscle cells in the tunica intima, and the formation of a plaque in the artery lining.

1.1.3. Myocardial infarction

A schematic of the anatomy and vasculature of the heart is provided in Figure 3. The heart consists of four chambers, the left and right atria at the top, and the left and right ventricles at the bottom (Figure 3.a). The blood is oxygenated in the lungs, enters the left atrium *via* the pulmonary veins and is sent to the left ventricle, which pumps it out through the aorta into the systemic circulation to supply the organs. The circulated blood then enters the right atrium *via* the venae cavae, is transferred into the right ventricle, which propels it through the pulmonary arteries into the pulmonary circulation, where it will be reoxygenated. The heart walls comprise three layers: the endothelium (inner layer), the myocardium (middle layer) and the epicardium (outer layer) (Figure 3.c). The myocardium is the thickest layer and is predominantly composed of cardiomyocytes, which are responsible for the heart beating.

In the case of MI, the obstructed vessel is a one of the coronary arteries that supply the cardiomyocytes with oxygen and nutrients. The coronary circulation starts with the left and right coronary arteries (LCA, RCA), which arise from the aorta. The LCA further divides into two main branches: the left anterior descending (LAD) and the left circumflex (LC) arteries, which supply the anteroseptal and the left walls of the heart, respectively. The RCA supplies the posterior and right walls of the heart (Figure 3.b and 3.c). The most commonly affected artery in MI is the LAD (~50%), followed by the RCA (~30%) and the LC (~20%) [10]. At the tissue level, vessel obstruction results in oxygen deprivation, known as ischemia, which causes cardiomyocyte necrosis in the area that was originally perfused by the obstructed vessel. This necrotic tissue forms an infarct, which constitutes a permanent damage to the heart. The extent and consequences of this damage will depend on the size of the zone of perfusion, the degree of obstruction, the duration of the impaired coronary blood flow and the presence of collateral vessels [11].

Myocardial infarction manifests itself through the development of an acute coronary syndrome (ACS). This syndrome is characterised by chest pain or discomfort known as angina, which is often described as crushing, aching or burning. This pain is typically continuous and severe, and can irradiate in one or both arms, the jaw, neck, back or

stomach. Other symptoms include dyspnea (shortness of breath), feeling dizzy or lightheaded, digestive symptoms, diaphoresis (sudden heavy sweating), unexplained fatigue and feeling restless or apprehensive. When a patient is brought to the hospital with an ACS, definitive diagnosis of MI is made based on the results of an electrocardiogram (ECG) and a blood test for specific cardiac markers [12]. MI can be categorised into two subtypes depending on the presence of an abnormal "ST" segment elevation on the ECG: non-ST-elevation myocardial infarction (NSTEMI) or ST-elevation myocardial infarction (STEMI). In NSTEMI, the vessel obstruction is transient or near-complete, resulting in the formation of a subendocardial infarct. On the other hand, STEMI is characterised by the complete obstruction of the coronary leading to a transmural infarct (Figure 3.d). Although NSTEMI may look less severe than STEMI, it can actually be just as life-threatening and both conditions are regarded as emergencies.

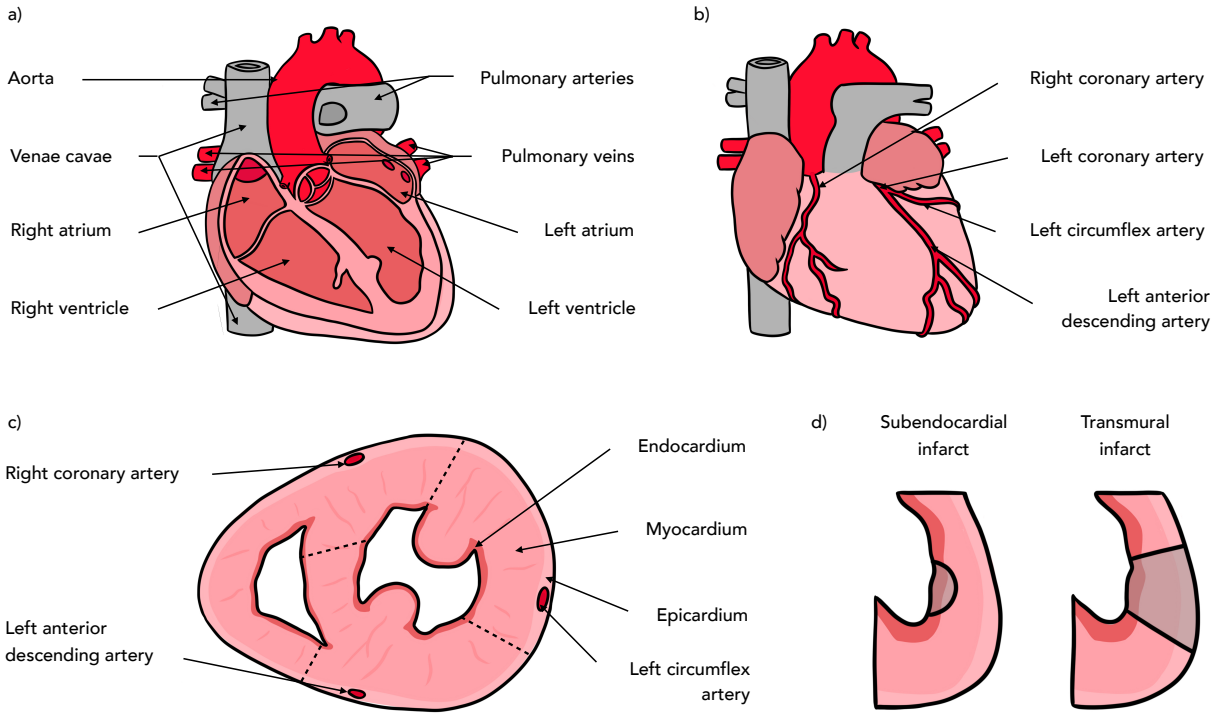


Figure 3: Heart anatomy and vascularisation. a) Longitudinal section showing the four chambers and great vessels of the heart. b) Front view showing the main coronary arteries. c) Cross-section of the heart showing the three main coronary branches supplying the ventricles with blood and their area of perfusion. d) NSTEMI leads to the formation of a subendocardial infarct while STEMI results in a transmural infarct.

In the absence of any medical intervention, the infarct undergoes different healing and remodelling phases, from the development of an acute inflammatory response to the formation of a collagen-rich scar [13] (Table 1). This cascade of reactions is commonly referred to as a maladaptive response given that the heart is inherently unable to regenerate or repair without medical intervention, leading to cardiac complications. These complications occur from the first few days (*e.g.*, arrhythmias, acute heart failure, pericarditis, myocardial rupture) to weeks (*e.g.*, chronic heart failure) following the disease onset. For MI survivors, the infarcted muscle is gradually replaced by a non-contractile fibrotic scar. The extent of the scar will determine the patient's heart pumping ability and long-term survival [14].

Table 1: Phases of cardiac healing and remodelling following a myocardial infarction.

0-7 days	1-3 weeks	2-6 weeks
Phase 1 **Acute inflammation**	**Phase 2** **Proliferation and resolution**	**Phase 3** **Remodelling and scar formation**
Cardiomyocyte necrosis	Myofibroblast proliferation	Formation of a mature scar
Haemorrhage and oedema	Collagen deposition	Myofibroblasts apoptosis
Neutrophil infiltration	Cardiac progenitor cell proliferation	Cardiac hypertrophy
Extracellular matrix breakdown	Angiogenesis	Ventricular wall weakening

1.2. Unmet therapeutic need

1.2.1. Current therapeutic strategies

Myocardial infarction necessitates emergency care, as time-to-treatment is strongly correlated with heart function recovery and survival [15]. Current strategies comprise the reperfusion of the ischemic area, the use of medication to relieve pain, prevent recurring infarcts and reduce the heart oxygen demand, as well as the management of associated risks factors. (Table 2) [12]. Importantly, these strategies are part of a complex system, in which each patient constitutes a special case. As a general rule, a patient with suspected MI will quickly be admitted to an intensive care unit. Once the diagnosis is confirmed, the patient is immediately reperfused and medicated, and kept under close monitoring for an

average of three days [16]. However, patients who are at high risk of reoccurrence or complications are usually transferred to a cardiac rehabilitation service, where they can be further monitored before being discharged. In either case, initial care aims at stabilising the patient and is critical for short and longer-term survival. Thus, it is a requirement that the introduction of additional therapeutic strategies must be compatible with the current standard medical care.

Table 2: Current therapeutic strategies for myocardial infarction.

Initial management for acute coronary syndrome	
Oxygen	Maintain sufficient oxygen saturation
Anti-platelets (*e.g.* aspirin, clopidogrel, abciximab) + Anti-coagulants (*e.g.* heparin, bivalirudin)	Prevent recurring ischemic events
Anti-anginal therapy (*e.g.* nitroglycerin +/- morphine)	Relieve angina pain
Beta-blockers (*e.g.* bisoprolol) + angiotensin-converting enzyme inhibitors (*e.g.* captopril) or angiotensin receptor blockers (*e.g.* candesartan)	Reduce heart workload and oxygen demand
Statins (*e.g.* atorvastatin)	Reduce blood cholesterol levels
Definitive management	
Reperfusion: percutaneous coronary intervention +/- aspiration thrombectomy +/- use of a stent	Revascularise the infarcted area
Fibrinolytic therapy (*e.g.* streptokinase)	
Coronary artery bypass graft	
Long term management	
Management of risk factors: quit smoking, reduce alcohol intake, improve diet, lose weight and exercise regularly, treatment for diabetes and hypertension, if necessary	
Pharmacological therapies: continue angiotensin-converting enzyme inhibitors or angiotensin receptor blockers + beta-blockers + anti-platelets + statins	

Existing therapeutic approaches are purely palliative, as they may only slow down the disease progression but do not reverse any existing damage [17]. In most cases, as the pathology evolves, more medication is needed to maintain the quality of life of the patient, while combinations of treatments are often used. Although survival rates have increased with the introduction of beta-blockers and angiotensin inhibitors [18], no curative therapy exists to replace the damaged tissue and restore the cardiac function.

1.2.2. Biological medicinal products

Cardiac regenerative medicine aims to preserve or restore heart function after an MI, by preventing cardiac tissue damage, enhancing heart repair, or replacing the apoptotic cells. In the last two decades, a whole new class of medicines have emerged under the name of biological medicinal products (biologics in short). Unlike chemically-synthesised medicines that are generally designed to be highly specific to a single receptor or pathway, biologics are biology-inspired treatments. There are three main categories of biologics: cell therapies (*e.g.* adult cells, stem cells), recombinant protein therapies (*e.g.* antibodies, growth factors, cytokines) and gene therapies (*e.g.* recombinant plasmids, miRNAs, transcription factors).

Cell therapy is the one that has by far been the most investigated in the context of heart repair [19, 20]. Early efforts included cell implantation in the heart with the aim to restore the lost cardiomyocytes pool and consequently heart function. The main cell types used in clinical trials are listed in Table 3. The first attempts focused on using autologous non-cardiac cells that were believed to be able to integrate within the damaged tissue, and either replace the necrotic cells or form new blood vessels [21-24]. They also offer the advantage to be relatively easy to isolate from the patient's tissue, blood or bone marrow and, in some cases, expand *in vitro* before delivery. Bone marrow-derived mononuclear cells (BM-MNCs) and mesenchymal stem cells (MSCs) in particular gained a lot of attention. In a randomised clinical trial published by Pokushalov *et al.*, the injection of BM-MNCs into the myocardium of patients who had an MI in the past 12 months combined with the administration of the standard medical treatment (SMT) was able to reduce the one-year mortality rate by 28% compared to the control group treated with SMT alone [22]. In another clinical trial, intracoronary infusion of MSCs was able to increase myocardial viability and perfusion, and improve heart function compared to the administration of a placebo [24]. Although initial results were encouraging, the actual regenerative potential of these cells for cardiac repair remains controversial [25, 26]. As a consequence, many groups started working on a second generation of cardiac-committed cell types, including autologous cardiac stem cells (*e.g.* cardiosphere-derived cells (CDCs)), and pluripotent stem cell-derived cardiomyocytes and cardiac progenitor cells (CPCs). Unlike the first generation,

there is solid evidence that these cell types can differentiate into cardiomyocytes and form functional contractile tissues *in vitro* [27, 28]. Most cell types have now entered clinical trials for the treatment of MI. One study in particular has reported extremely promising results. In a randomised phase I clinical trial involving MI patients, intracoronary infusion of CDCs was shown to decrease the scar mass by 28% after six months [29]. These positive findings support the hypothesis that cell therapy could be a viable option for heart repair.

Table 3: Main cell types used in clinical trials for heart repair.

Cell type	Main sources	Example of clinical trials
First generation: non-cardiac cells		
Skeletal myoblasts	Autologous (muscle tissue)	NCT00102128 (MAGIC) (21)
Bone marrow-derived cells (*e.g.* mononuclear cells)	Autologous or allogeneic (bone marrow)	NCT00841958 (ESCAPE) (22)
Mesenchymal stem cells	Autologous or allogeneic (*e.g.* bone marrow, blood, adipose tissue)	NCT01291329 (WJ-MSC-AMI) (24)
Endothelial progenitor cells	Autologous or allogeneic (*e.g.* blood, umbilical cord blood)	NCT00694642 (PROGENITOR) (23)
Second generation: cardiac-committed cells		
Cardiac stem cells (*e.g.* cardiac progenitor cells, cardiosphere-derived cells)	Autologous (cardiac tissue)	NCT00893360 (CADUCEUS) (29)
Induced pluripotent stem cell-derived cardiomyocytes or progenitors	Autologous or allogeneic (*e.g.* blood, skin)	No completed clinical trial
Embryonic stem cells-derived cardiomyocytes or progenitors	Allogeneic (human embryos)	NCT02057900 (ESCORT) (30)

Although cell therapy has emerged as a highly promising area for cardiac repair, it also presents a number of ethical, regulatory, logistical and safety limitations that still need to be addressed before any potential commercialisation [31]. Although only few clinical trials reported occurrence of severe adverse effects, safety remains a major concern when using living cells. Tumour development arising from injected embryonic stem cells is now well described but care must be taken with all cell types [32]. In addition, implanting pluripotent stem cell-derived cardiomyocytes has been reported to increase the risk of developing arrhythmias, due to improper electrical integration of the grafted cells [33].

Adverse immune reactions are also a concern. Autogenic cell therapy was for long considered the ideal solution for avoiding the risk of graft rejection [34]. However, the process of cell harvesting is often invasive (*e.g.* bone marrow aspiration) and long *in vitro* culture periods are often required to reach sufficient yields, which make autologous cell therapies incompatible for early intervention. In addition, cell quality has been reported to diminish with donor age and co-morbidities, which constitutes a real limitation for MI patients, who tend to be older [35]. On the other hand, allogeneic cells could offer a more suitable clinical option for acute patients as they can be harvested from a donor, expanded *in vitro* and stored as an off-the-shelf product in a cell bank, ready to be used. Nevertheless, although first results of cell therapy studies have initially raised a lot of excitement in the field of cardiac repair, there is a need and opportunity for new cell-free biologics that can replicate the regenerative effects of live cells while overcoming their numerous limitations.

1.2.3. Delivery challenges for heart regeneration

Like any other drug, the efficacy of cardioprotective treatments is highly dependent on their mode of delivery. Safely delivering an adequate amount of bioactive drug into the target site and making it available for an adequate amount of time is essential to maximise any beneficial effect and minimise off-site targeting. Surprisingly, despite the large number of clinical studies using cell therapies, there is still no consensus on key delivery parameters, such as the optimal administration timepoint, the treatment regimen (dosage, number of injections) and the route of delivery. It is possible that unoptimised delivery parameters may have been detrimental to many clinical trials [36, 37].

The human heart only has limited innate capacity for self-repair, which means that it is often unable to compensate for the massive loss of cardiomyocytes following an MI. In fact, increasing evidence suggests that cardiac tissue is able to renew but only at a very low level, and that the rate of cardiomyocyte renewal is reduced with age, from 1% per year at the age of 25 to 0.45% by the age of 75 [38-40]. Regenerative therapies can be developed to harness existing natural repair pathways before remodelling becomes irreversible. In humans, there is an optimal window within the first two weeks after disease onset, however,

this will vary from one patient to another. Interestingly, researchers are developing non-invasive methods for tracking tissue remodelling, which could be used in the context of personalised medicine to tailor regenerative treatments to individual patients [41]. The question of finding the optimal timing of intervention has been investigated in small animals using various cell types. In two similar studies, delivering MSCs one week after MI led to superior results compared to an immediate or later delivery [42, 43]. In a study by Hu *et al.*, left ventricular systolic dimension was significantly decreased in the group treated with MSCs one and two week after MI compared to the control group (0.71 cm and 0.74 cm respectively *vs* 0.85 cm), while no improvement in heart function was observed in the one hour group [42]. Similar trends were observed with infarct size [42]. Interestingly, a significantly greater number of live implanted cells was found in the one week group compared to one hour and two weeks [42], suggesting that the early administration of cells in the infarcted myocardium could lead to higher cell loss rates. These results could be explained by the highest levels of inflammation and hypoxia found in the myocardium in the days following an MI [42, 44]. Similar trends were observed with cardiomyocytes, which outperformed when implanted at two weeks compared to immediately or four weeks after the MI [45]. These results suggest that delivering a cell-based regenerative therapy between one and two weeks after the infarct might indeed be optimal, although this time window may differ between cell types and animal models. These observations have yet to be confirmed in humans [46-48]. However, with regards to the risk-benefit balance, injecting a therapy before three to ten days after disease onset is unlikely to be clinically acceptable, as it may increase the risk of ventricular rupture [49]. On the other hand, waiting weeks before taking action might not give the best chances for the patient's heart to repair. Additional studies are needed to confirm these hypotheses.

The second area of improvement is the delivery route used to target the heart. Three main approaches have made their way to the clinics: intracoronary infusion, transepicardial injection and transendocardial injection (Figure 4). Intracoronary infusion is the least invasive technique and can be used in almost any MI patient at any timepoint. This systemic approach uses a catheter, similar to the one used during reperfusion, to inject drugs directly into the coronary system. Due to its practicality, this route is by far the most widely used for

administering cell therapies to IHD patients. However, injecting a drug directly into the bloodstream can lead to a suboptimal bioavailability in the target tissue and accumulation in other organs [50]. Moreover, systemic routes are incompatible with microparticle-based approaches, because of the risk of embolisms.

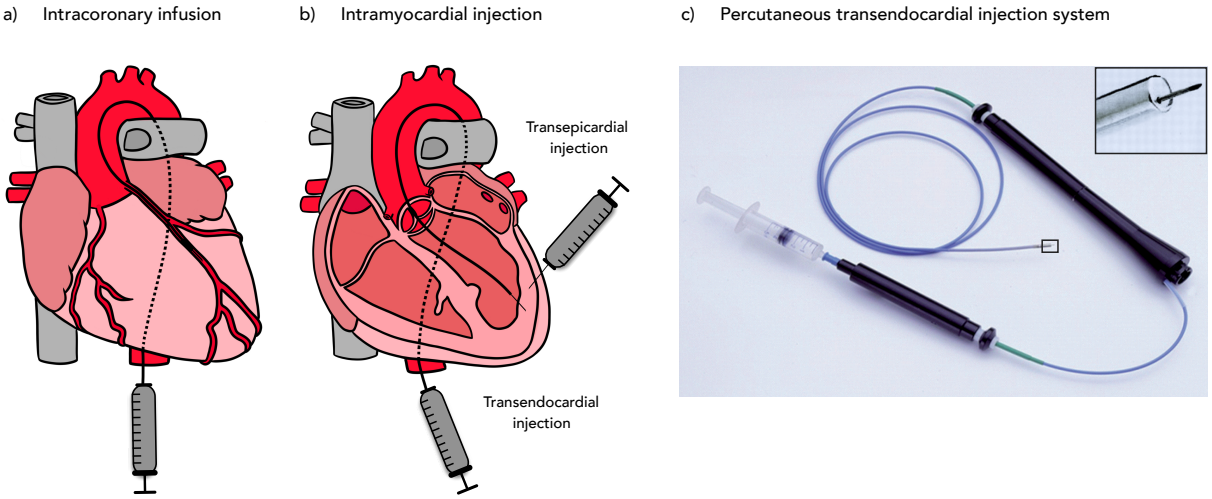


Figure 4: Delivery routes for targeting the heart. a) Intracoronary infusion. A catheter is inserted in one of the femoral artery up to the coronary system *via* the aorta and used to inject the therapy directly into the coronary blood stream. b) Intramyocardial injection. Therapies can either be administered during an open-chest surgery by transepicardial injection or percutaneously using a catheter-based transendocardial injection system. The latter is inserted into the ventricle cavity *via* the aorta and uses a curved needle to inject the therapy into the heart wall. c) Example of a percutaneous catheter-based transendocardial injection system (Myostar™) (51).

Alternatively, drugs can be delivered locally into the target tissue, which maximises the drug bioavailability and minimises the risk of side effects. However, intramyocardial injections can be rather challenging to perform, especially in an already damaged heart. These injections can be aided by mapping tools that allow targeting of specific regions of interest [51], usually the infarct border zone, where repair pathways are the most active [52]. Intramyocardial injections can be subdivided into two categories depending on the approach: from the outside of the heart (transepicardial) or from the inside of the heart (transendocardial). Transepicardial injections typically require an open-chest surgery to access the heart and inject the drug using a syringe and needle. Although using such invasive approaches can be acceptable in later stages of the disease, especially when combined with other interventions such as a bypass surgery, minimally-invasive options are needed when targeting the acute patient population. Transendocardial injections combine

the advantages of using a percutaneous catheter-based approach with a local intramyocardial injection. In this technique, a medical device comprising a catheter is introduced into the circulation *via* the femoral artery, up to the ventricle cavity, where a curved needle can be deployed to inject the therapeutic into the heart wall. Five devices are currently available on the market and used in clinical trials (Table 4).

Table 4: Percutaneous catheter-based intramyocardial injection systems available on the market.

Device	Company	Needle gauge	Needle inner diameter	Example of clinical trial
C-cath$_{EZ}$™	Celyad	28G	0.184 mm	NCT01768702
Myostar™	Biosense Webster	27G	0.210 mm	NCT01556022
Stiletto™	Boston Scientific	26G	0.260 mm	NCT00090714
Myocath™	U.S. Stem Cell	25G	0.260 mm	NCT00054678
Helix™	Biocardia	25G	0.260 mm	NCT01087996

The development of mapping tools combined with percutaneous catheter approaches has opened new avenues for the treatment of IHD patients. In particular, the combination NOGA®/Myostar™ has been used in multiple clinical trials to deliver cells [53-57] or a gene therapy [58]. In fact, a successful first-in-man study was performed on acute MI patients, suggesting that the early administration of regenerative therapeutics using catheter-based devices is a feasible approach for the treatment of MI [59].

2. Extracellular vesicles as therapeutics

2.1. Definition and physiological role of extracellular vesicles

2.1.1. Paracrine effect *vs* cell integration

Cell therapy treatments involving cell transplantation to promote localised tissue regeneration have been found to act through two distinct mechanisms. They can engraft and integrate within the host tissue to provide support and replace the lost cells [60]. Alternatively, they can secrete paracrine factors that interact with endogenous pathways of the resident cells [61]. The two mechanisms can be concurrent. However, in the case of cell-based therapies targeting IHDs, numerous studies have reported the rapid loss of implanted cells within the first few days following their injection, suggesting that the longer-term functional benefits of such treatments could not be attributed to stem cell survival but rather to the secretion of factors promoting endogenous healing [62, 63].

This so-called paracrine hypothesis led to extensive analysis of the cell secretome to identify the mechanisms and actors responsible for the positive effects observed [64]. Although the composition of secreted products can change depending on the cell type and environmental conditions [65], it is possible to categorise them into two main families: soluble factors and extracellular vesicles (EVs). Soluble factors include all molecules (*e.g.*, growth factors, chemokines and cytokines) that are released as free entities in the extracellular compartment. They can induce various responses through their interaction with specific receptors on target cells and some factors are well known for having major roles in tissue homeostasis. However, it has become increasingly evident that one or a few soluble factors could not recapitulate the effects of complex signalling pathways involved in tissue regeneration. As a result, gene and recombinant protein therapies have not yet been able to meet their expectations in the field of cardiovascular diseases [66].

On the other hand, many groups working to identify the therapeutic effectors of regeneration have indicated that EVs are likely to have a major role [67]. In 2008, Timmers *et al.* showed that conditioned media obtained from human MSCs were able to reduce infarct size by 60% in a pig model of MI. In addition, fractioning experiments revealed that the cardioprotective effect was due to products exceeding 1000 kDa (or 100-300 nm), indicating that EVs may be responsible for the observed improvement rather than soluble factors [68]. In another report, CPCs with decreased secretion of exosomes, a subtype of EVs, failed to reproduce the beneficial effects of purified CPC-derived EVs *in vitro* and in a mouse model of MI [69].

2.1.2. EVs as new therapeutic tools

All major cell types release EVs both under physiological and pathological conditions, including primary adult cardiac cells, such as cardiomyocytes [70, 71], endothelial cells [72] and fibroblasts [73]. The term 'extracellular vesicles' includes different entities that can be classified into three main categories depending on their biogenesis: exosomes, microvesicles and apoptotic bodies (Table 5, Figure 5) [74].

Table 5: EV classification depending on their origin.

EV type	Size	Biogenesis
Exosomes	30-100 nm	Exocytosis of endosomal vesicles called multivesicular bodies
Microvesicles	100-1000 nm	Cellular membrane budding
Apoptotic bodies	50-5000 nm	Release by apoptotic cells as blebs

EVs are delimited by a lipid bilayer similar to the cell membrane and participate in cell-to-cell communication. They are able to carry various components such as proteins, lipids and genetic material (DNA, mRNA, miRNA and ncRNA), which they can deliver to target cells by direct membrane fusion [75], receptor binding-mediated signalling pathways [76] or endocytosis [77], leading to a change in their phenotype and/or function [78]. Interestingly, EVs have been shown to play important roles in numerous situations such as tissue repair [74], immunomodulation [79], neurotransmission [80] and tumour progression [81].

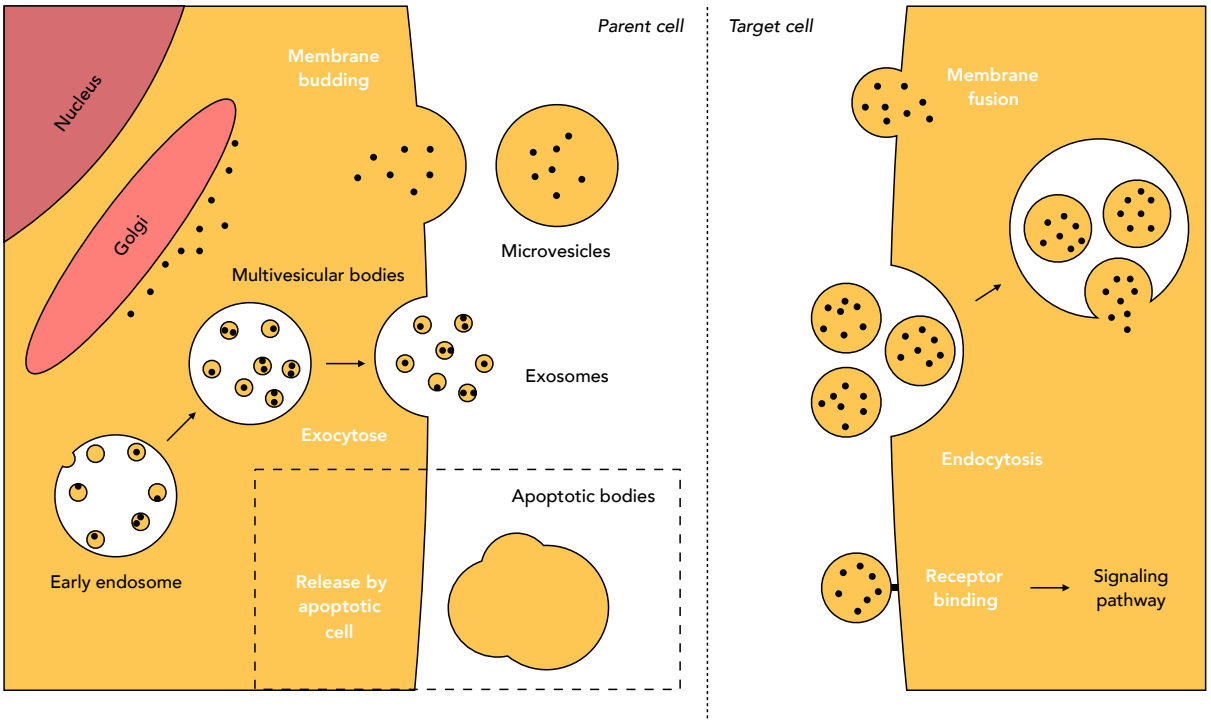


Figure 5: EV types and biogenesis and internalisation mechanisms. Exosomes are released by exocytosis of multivesicular bodies while microvesicles are formed through membrane budding. Apoptotic bodies are released by apoptotic cells as blebs (left). EVs can be internalised by target cells *via* membrane fusion, endocytosis or receptor-binding mechanisms (right).

EV-based treatments could circumvent many of the limitations associated with cell therapy. For instance, EVs avoid several of the safety risks inherent to the use of living cells described in 1.2.2. Indeed, as non-replicating, non-viable entities, EVs are completely deprived of the essential living properties that make a cell potentially harmful [82]. In addition, evidence suggests that EVs may be hypoimmunogenic. In a study published by Mirotsou *et al.* in 2015, repeated subcutaneous injections of xenogeneic EVs induced a reduced immune reaction compared to the injection of the parent cells, while the administration of allogeneic EVs did not induce any significant reaction [83]. EVs also offer a number of advantages with regard to their production process [84]. Specifically, EVs can be produced from large numbers of cells in culture and isolated using common purification steps, such as filtration and chromatography. First reports have shown that they can then be stored at 4°C, -80°C or freeze-dried using non-toxic cryopreservatives and stored for a few days to weeks with no significant change in their morphology, although cargo stability must also be taken into consideration [85-88]. In addition, using parent cells as biofactories could drastically reduce the production costs compared to cell therapy products [84]. As a result,

EV-based therapies offer a promising option for the development of new regenerative treatments.

2.2. EV production and characterisation

2.2.1. EV isolation and purification

Therapeutic EVs are usually isolated from conditioned cell culture media or bodily fluids. Conditioned media is obtained by cultivating cells in specific conditions that allow accumulation of cell-secreted products, including soluble proteins and EVs. However, many cell culture media use serum to support cell growth, which itself contains EVs [89]. It is thus recommended to work with chemically-defined media or use EV-free serum, which can be purchased or prepared by EV-depleting serum using ultracentrifugation- [90] or ultrafiltration-based protocols [91]. Cells that require serum can also be cultivated in their usual media and serum-starved only when harvesting EVs.

EVs can be isolated from conditioned media using different biophysical and biochemical properties, such as size, density, surface charge and surface markers. The most commonly used methods are described Figure 6. Differential centrifugation, which has for a long time been the most common EV preparation method, uses high speed centrifugation to pellet compounds based on their size and density. However, it has been shown to induce EV damage and aggregation [92-95] and protein contamination [92]. Density gradient centrifugation, a similar technique, uses a dense medium to form a gradient and separate compounds based on their density only. This method is more gentle on the EVs and co-purify contaminants to a lower degree. However, both of these centrifugation-based techniques are currently relatively time-consuming and not scalable for clinical use. Ultrafiltration (UF) allows separation of EVs from soluble compounds using a filtration membrane with specific pore size, on which pressure (*e.g.* centrifugal force) is applied. Smaller molecules pass through the membrane pores while EVs and bigger molecules are retained in the upper compartment [96]. Size exclusion chromatography (SEC) uses a column filled with porous resin beads to separate compounds based on their size [97].

Larger compounds, such as EVs, advance between the resin beads and are eluted first, while smaller compounds, such as soluble proteins, are retained in the resin pores and take longer to be eluted. Being both size-based methods, UF and SEC present the risk of contamination with similar-sized particles such as protein aggregates. Immunocapture is particularly useful for isolating EV subpopulations expressing a specific marker, which can be limiting when studying the general population of EVs. Finally, precipitation is a widely used method in commercial kits. It uses a precipitating agent (often a polymer) to separate EVs from the media. However, contamination with protein and precipitating agent limits its use when pure samples are required.

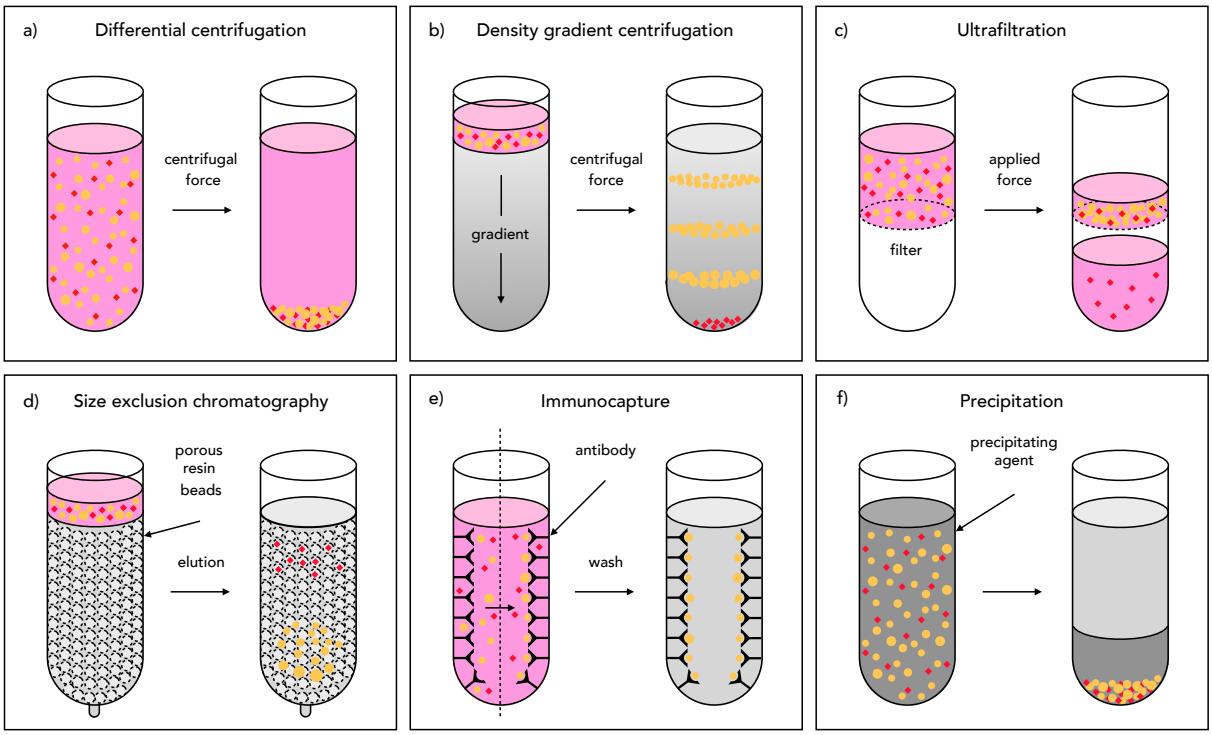


Figure 6: Main methods used for EV isolation and purification. These methods aim at isolating the EVs (orange) from conditioned media or bodily fluid (pink) and removing contaminants such as proteins (red). a) Differential centrifugation uses high speed centrifugation to pellet compounds based on their size and density. b) Density gradient centrifugation uses a dense medium to form a gradient (grey scale) and separate compounds based on their density. c) Ultrafiltration allows a size-based separation of compounds using a filtration membrane with specific pore size on which pressure (often centrifugal force) is applied. d) Size exclusion chromatography is a size-based separation methods that uses a column filled with porous resin beads. e) Immunocapture uses immobilised antibodies to bind compounds expressing specific surface markers. f) Precipitation uses polymer-based precipitating agents (dark grey) to precipitate compounds and separate them from the media.

Although some protocols are more effective than others at removing contaminants, none of these methods have yet been established as the gold standard in the field. Moreover, combining multiples methods to improve efficiency can be challenging as EV purification often comes at a cost of a decreased yield and increased chances of damaging the EV. UF combined with SEC has recently been shown to be very efficient for the purification and concentration of functional EVs [98-100]. UF was reported to be able to concentrate EV suspensions up to 240-fold [89] and could be replaced by tangential flow filtration, a similar membrane-based separation technique, for industrial scale production [101]. The concentrate can then be processed by SEC, has been shown to provide a reproducible 40-90% EV recovery and allows EVs to be efficiently separated from soluble proteins [102]. It is also relatively quick and inexpensive to run and can be scaled up for clinical use [84]. Finally, given the dilution of the EV sample during SEC, a second UF step may be necessary to concentrate the purified EV fractions into a smaller volume before use.

None of the discussed isolation methods is currently able to isolate a pure population of EVs with 100% recovery. In fact, their performance depends on a multitude of parameters that are not systematically reported in publications. In an effort to improve the quality and reliability of reported results, the International Society of Extracellular Vesicles (ISEV) has published recommendations on the minimal requirements for the definition of EVs [103]. A platform (EV-TRACK) was also launched for the transparent data reporting and centralisation of knowledge related to EV research [104].

2.2.2. EV characterisation

Isolation, purification and concentration should be accompanied by a proper characterisation of the resulting EVs. Different techniques can be used for imaging, sizing and quantification, as well as characterising their content and functionality. The gold standard for imaging EVs is electron microscopy (EM), a technique that uses a high voltage electron beam as a source of illumination. Indeed with a resolution of 1-3 nm for transmission EM, these methods can be used to visualise EVs, from their formation in the parent cell to their internalisation by target cells [105]. EV samples can be prepared for EM

using classic cell and tissue preparation methods based on fixation, resin embedding, sectioning and staining [106]. However, better preservation of the EV ultrastructure can be achieved using high-pressure freezing and freeze substitution in place of fixation [107]. EM is also the method of choice to investigate the presence of EVs or protein aggregates and validate any newly-optimised isolation methods.

Two techniques are commonly used for sizing and quantifying EV populations. Nanoparticle tracking analysis (NTA) can be used to measure the hydrodynamic diameter and concentration of suspended nanoparticles by tracking their Brownian motion using a dark field microscope. Resistive pulse sensing (RPS) uses the Coulter principle applied to nanoparticles passing through a pore. None of these methods, however, are able to distinguish EVs from other nanoparticles. NTA can be coupled with fluorescence to enable more specific analysis of labelled EV populations [108]. NTA is also more practical for the analysis of polydisperse samples, for which RPS would require multiple measurements using different pore sizes [109].

Characterising EVs also requires measuring their composition and assessing functionality. RNA content can be investigated using transcriptome sequencing, quantitative polymerase chain reaction (qPCR) and northern blotting [110]. Standard methods such as bicinchoninic acid (BCA) assays, western blotting and enzyme-linked immunosorbent assays (ELISA) are widely used to investigate EV protein content as well as protein contaminants [111]. In the next few years, flow cytometry could become a very powerful technique for single EV surface markers analysis and characterisation [112, 113]. Improvement in instrument sensitivity as well as determination of adequate surface markers and labelling techniques are still required before this method can reach full potential. Recently, metabolomics has emerged as a new omics approach to study small molecules (<1500 Da) content including lipids, sugars, nucleotides and amino acids [114]. The biological function of EVs can be assessed using functional cell-based assays that are tailored to their effects and intended use. Finally, animal models can be used to study EV biodistribution and targeting within living systems.

2.3. EVs for cardiac repair

2.3.1. Cardioprotective EVs

Most cell types discussed in Part 1 are now being investigated to determine whether the EVs they secrete can reproduce these therapeutic effects. Two EV types in particular seem to stand out, those derived from MSCs and cardiac-committed cells.

MSCs represent a very interesting EV source for cardiac repair, and offer many advantages over other cell types. First, they can be relatively easily isolated from various tissue sources, including bone marrow, adipose tissue, placenta and umbilical cord, and rapidly expanded *ex vivo*. MSCs are multipotent stem cells that can differentiate into cells of mesenchymal lineages, including osteoblasts, chondrocytes and adipocytes [115], but also into other cell types such as neurones, skeletal muscle cells, endothelial cells and vascular smooth muscle cells [116]. Studies have shown MSCs to have immunomodulatory properties [117]. This offers the opportunity for allogeneic MSCs to be used as bioreactor cells for the production of EVs that can be safely administered to unmatched patients [53]. This property offers substantial practical advantages in a clinical setting, when autologous products are not compatible with a rapid treatment administration or ineffective due to disease-induced cell dysfunction. Accumulating preclinical data have found that EVs derived from MSCs demonstrate promising therapeutic effects in many conditions, including MI [68, 118-122], in which they were shown to be able to reduce infarct size [118-122]. In particular, in a study published by Zhao *et al.* in 2016, MSC-derived EVs, purified by UF and gradient density centrifugation, significantly improved heart function in a rat model of MI, while EV-deprived conditioned media had hardly any effect. In the same study, EVs were also reported to reduce cardiac fibrosis, prevent cardiomyocyte apoptosis and promote cell proliferation in the infarct border zone [121].

As discussed in Part 1, cardiac-committed cell therapies have raised a lot of interest due to their commitment in the cardiac lineage. Interestingly, recent reports indicate that EVs derived from cardiac stem cells [123-128] and pluripotent cell-derived CPCs [129] and

cardiomyocytes [130] can recapitulate the effect of parents cells. An exhaustive list of all published preclinical studies using cardiac committed cell-derived EVs is provided in Table 6. As a matter of fact, all studies but one showed that the injection of second generation EVs into the infarcted heart could improve cardiac function and prevent remodelling. In 2017, a study by Gallet *et al.* reported that the NOGA®-guided intramyocardial injection of EVs obtained from CDCs was able to improve heart function, preserve ventricular volumes and reduce scar size, as well as increase blood vessel density and cardiomyocyte proliferation in a porcine model of MI [127]. Although all of these studies used EV isolation protocols that may not effectively remove all protein contaminants, another study by Ibrahim *et al.* looked at the effect of inhibiting exosome secretion by CDCs to provide evidence that CDC-derived EVs were responsible for the observed beneficial outcomes [125].

Table 6: Preclinical studies using cardiac-committed cell-derived EV.

EV source	Delivery route	EV purification	Model	Ref.
Cardiosphere-derived cells	Transepicardial intramyocardial injection	Precipitation	Mouse	(125)
Cardiosphere-derived cells	NOGA®-guided transendocardial intramyocardial injection	Precipitation	Pig	(127)
Cardiac progenitor cells	Transepicardial intramyocardial injection	Precipitation	Rat	(124)
Cardiac progenitor cells	Transepicardial intramyocardial injection	Ultracentrifugation	Rat	(126, 128)
Cardiac progenitor cells	Transepicardial intramyocardial injection	Precipitation	Mouse	(123)
Induced pluripotent stem cell-derived cardiomyocytes	Epicardial collagen patch	Precipitation	Rat	(130)
ESC-derived progenitor cells	Transepicardial intramyocardial injection	Ultracentrifugation	Mouse	(129)

These positive findings bring new opportunities for developing cell-free cardioprotective therapies that provide similar benefits compared to implanting live cells. EVs have now started to be investigated in patients for the treatment of stroke (NCT03384433), wound healing (NCT02565264), cancer (NCT01294072, NCT03608631), macular regeneration (NCT03437759), endocrinology (NCT03493984, NCT02138331) and even for vaccination (NCT0115928). Clinical trials using EV-based treatments for cardiac repair are to be expected in the next few years.

2.3.2. Current limitations of EV-based therapies

Although the discovery of EVs has opened new opportunities for the development of cell-free cardiac regenerative therapies, their efficacy has yet to be established in a clinical setting. To advance towards first-in-man trials, a better understanding of the biology of EVs as well as the development of standardised production protocols and EV delivery systems is crucial.

EVs are a very heterogeneous population, with poorly-understood biological functions. Collective efforts should be focused on a better understanding of their mechanism of action and pharmacokinetics, as well as identifying the main actor (*e.g.* EV subtype, specific cargo) of the functional benefits observed. Further investigations should provide greater evidence of their therapeutic potential and safety.

Developing standardised protocols for EV isolation and characterisation that account for the variability within EV samples, as well as between batches and donors, is also essential [131]. Industrial-scale methods using good manufacturing practices (GMP)-grade EV, as well as quality control and validation procedures will be also needed in order to facilitate their clinical translation [132]. Finally, commercialisation of new EV-based therapeutics will require categorisation into the existing advanced therapy medicinal products (ATMP) regulatory framework. Although new EV-specific rules might not be necessary, explicit guidelines covering the manufacturing and clinical evaluation of EV-based drugs may be needed [133].

Although injecting EV suspensions has proven to be a feasible option and showed encouraging first results, more sophisticated drug delivery systems are being investigated. Indeed, the performance of EV-based therapeutics is directly subject to their bioavailability within the targeted tissue for the adequate amount of time. Yet, in the vast majority of cases, EV-based products are administered as single treatment, which does not align with the timeline and complexity of regenerative processes involved in cardiac repair. It is thus hypothesised that increasing EV bioavailability may be able to induce a clinical improvement. Additionally, numerous publications have reported the administration of EVs

by systemic routes. These practices were shown to result in a majority of EVs being uptaken by the liver and spleen [134], which could explain their limited efficacy. On the other hand, intramyocardial injection of EVs was reported to be more efficient at targeting the damaged tissue [134]. Similarly to cell therapy, the EV delivery route has a considerable impact on EV targeting and retention at the site of injury. A study comparing the different routes of delivery using radiolabeled cells found that ~11% of the cells injected into the myocardium were retained, whereas only <3% of them were found in the tissue after intracoronary infusion [50]. These overall low retention rates can be caused by many factors, including leakage of the cell suspension out of the tissue just after injection, which is directly correlated to the volume injected [135]. In addition, implanted cells also need to resist the harsh environment of the infarcted heart, especially when administered in the acute phase, in which inflammation and oxidative stress levels are extremely high [44]. Although EVs might not be as sensitive to the environment as cells, optimising their administration modalities to maximise bioavailability is essential. Developing new systems for local delivery could help enhance stability as well as provide a sustained release that would better fit the requirements of long-standing physiopathological processes, such as tissue damage following MI [136].

3. Hydrogels for drug delivery in cardiac repair

3.1. Hydrogel definition and advantages in drug delivery

Hydrogels are 3D crosslinked polymer networks that can absorb large amounts of water. This high water-content allows hydrogels to closely mimic the native extracellular matrix (ECM) found in the body. Hydrogels can be formed *via* either physical or chemical crosslinking [137]. Physical crosslinking is a reversible interaction involving non-covalent bonds, such as hydrophobic interactions, ionic/electrostatic interactions or hydrogen bonding. By contrast, chemical crosslinking involves the formation of covalent linkages between reactive functional groups. Commonly used chemical crosslinking reactions are the Diels-Alder reaction, the Schiff base reaction and Michael-type additions, while covalent linkages can also be formed using free radical polymerisation, enzymatic crosslinking and click chemistry. Compared to physically-crosslinked hydrogels, covalently-crosslinked hydrogels generally have greater mechanical properties, provide better control over the hydrogel properties (*e.g.*, crosslinking density) and allow easier functionalization. These properties are beneficial for the development of controlled delivery systems [138].

At equilibrium, hydrogels contain 90-99% water, making them excellent candidates for the design of highly permeable networks for tissue engineering and drug delivery [137]. When immersed in aqueous solution, water will first bind to hydrophilic groups of the polymer and constitute the primary bound water. This first step induces swelling of the hydrogel and exposure of the hydrophobic groups, which will interact with water to form the secondary bound water. Bound water is considered a constituent part of the hydrogel structure and can generally only be removed under extreme conditions. Additional water can then be absorbed due to osmotic forces (free water or bulk water) and to the presence of interstices within the hydrated network (interstitial water).

Hydrogels present numerous advantages when used as a platform for drug release. They provide a certain level of drug protection against clearance and degradation by forming a

physical barrier against the local microenvironment. Pore size can be tuned to hinder immune cells infiltration into the network or inhibit rapid drug diffusion, resulting in an improved local retention at the site of delivery and an increased stability and bioavailability [139]. Depending on the polymer and crosslinking method used, hydrogels can be intrinsically degradable or synthesised to undergo programmed degradation under certain conditions (*e.g.*, pH, presence of catabolic enzyme) [140]. These properties can enable the local and controlled release of the bioactive cargo and potentially enhance its therapeutic effects, while avoiding the need for repeated deliveries. Finally, due to their ECM-like properties, hydrogels can be used as a support for cell recruitment and proliferation in the context of tissue regeneration [141].

3.2. Hydrogels in cardiac repair

3.2.1. Polymers used for heart delivery

Hydrogels have been extensively used to enhance the beneficial outcomes of cardiac regenerative biological therapies, either by the implantation of patches on the epicardium [30] or by the injection of hydrogels into the myocardium [142]. Both natural and synthetic-based hydrogels have been used in the context of cardiac repair. Natural polymers are found in nature and are made of proteins (*e.g.* collagen, fibrin, gelatin) or polysaccharides (*e.g.* alginate, hyaluronic acid, agarose, dextran, chitosan). They are usually biodegradable and highly bioactive, however, they have limitations that include poor mechanical properties and immunogenic potential [143]. Table 7 provides an exhaustive list of the completed clinical trials with published results that used natural hydrogels alone or as a delivery system for heart repair. Although alginate-based hydrogels in particular have shown promising preliminary results in humans, there is still insufficient data to demonstrate clinical safety. For example, in the AUGMENT-HF clinical trial, in which an calcium-alginate hydrogel was injected in the ischemic ventricle wall to provide mechanical support to the heart, mortality rate and incidence of adverse effect were increased in the group treated with hydrogel and SMT compared to the control group treated with SMT only (145-147). However, statistically significant functional improvements were reported in the treated

patients compared to the control group as measured by cardiopulmonary exercise testing, 6-minute walk test distance and New York Heart Association (NYHA) assessment. More studies are needed to confirm the potential benefits of such treatments.

Table 7: List of completed clinical trials with published results using natural-based hydrogels alone or as a delivery system for heart repair.

Material	Cargo	Delivery route	Phase	NCT (acronym)	Ref.
Alginate	None	Intracoronary infusion	N/A	NCT01226563 (PRESERVATION-1)	(142, 144)
Alginate	None	Transepicardial intramyocardial injection	II II/III	NCT00847964 NCT01311791 (AUGMENT-HFI)	(145-147)
Fibrin	Human embryonic stem cells-derived cardiovascular progenitors	Epicardial patch	I	NCT02057900 (ESCORT)	(30)
Gelatin	Basic fibroblast growth factor	Epicardial patch	I	NCT00981006 (ALCADIA)	(148)

In contrast, synthetic polymers offer high versatility and tunability, and present a high level of standardisation and consistency during production, resulting in limited batch-to-batch variation. They also offer great flexibility for chemical modification and provide a degree of control over chemical composition, physical features and mechanical properties [143]. For instance, synthetic systems can be made degradable and bioactive by incorporating functional groups onto the polymer backbone [149]. Although synthetic hydrogels have been extensively studied for cardiac repair in smaller animals [143], they have yet to be used in humans. The main representatives of this class of polymers are poly(ethylene glycol) (PEG), poly(acrylic acid) (PAA), poly(vinyl alcohol) (PVA) and poly(*N*-isopropylacrylamide) (PNIPAAM), polyacrylamide (PAAm).

3.2.2. PEG-based hydrogels

PEG is a non-ionic, hydrophilic polymer synthesized by ring-opening polymerisation of ethylene oxide. This polymer shows a high level of biocompatibility, which makes it relatively inert when implanted in living systems (*e.g.* animal models) [150]. This is due to its

anti-fouling property, which repels non-specific protein adsorption and cell adhesion [151-154]. In particular, the reduced adhesion of inflammatory cells decreases the chances of fibrous capsule formation, a common adverse effect of implanted materials [155]. Moreover, many PEG formulations have already been approved by the Food and Drug Administration (FDA), which enables relatively fast translational potential. Since the first proof-of-concept of PEGylation by Davis *et al.* in 1977 [156], PEG has been extensively employed to enhance the solubility, modify the pharmacokinetic profile and reduce the immunogenicity of drugs or drug vectors [157, 158].

The most basic structure of PEG is linear PEG diol, with two terminal hydroxyl groups. However, PEG hydrogels are typically synthesized *via* covalent crosslinking of PEG macromers with reactive chain ends [138, 159]. In particular, thiol-ene reactions between a thiol and an alkene are commonly used (Figure 7.a). This chemistry offers relatively rapid reaction kinetics under mild conditions, well-defined reaction mechanisms and products that are compatible with cells and other biological molecules. In addition, the process of introducing thiols and alkenes onto monomers is relatively facile compared to the introduction of other functional groups [160]. Given its high yield, rate and stereoselectivity, the thiol-ene reaction meets the conditions of a click chemistry reaction. Moreover, the reaction rate can easily be tuned to fit the needs of the application [161]. For instance, a maleimide group will typically offer faster crosslinking kinetics than a vinyl sulfone, an acrylate or a norbornene [162] (Figure 7.b).

Thiol-ene reactions can proceed *via* two main reaction mechanisms, a radical-based reaction or a Michael-type addition. In radical-mediated thiol-ene chemistry, crosslinking is initiated by the generation of radicals by thermal energy, redox reactions or photo-cleavage of initiator molecules [161]. Photocrosslinking is a particularly interesting approach, as it provides spatial, temporal and kinetic control over the crosslinking reaction by controlling the degree of light irradiation [163]. Although this type of reaction is advantageous for *in situ* gelation and micropatterning, it also leads to the presence of network non-idealities that affect drug release and material properties, as well as the presence of radicals that can damage the encapsulated drugs and surrounding tissue [164].

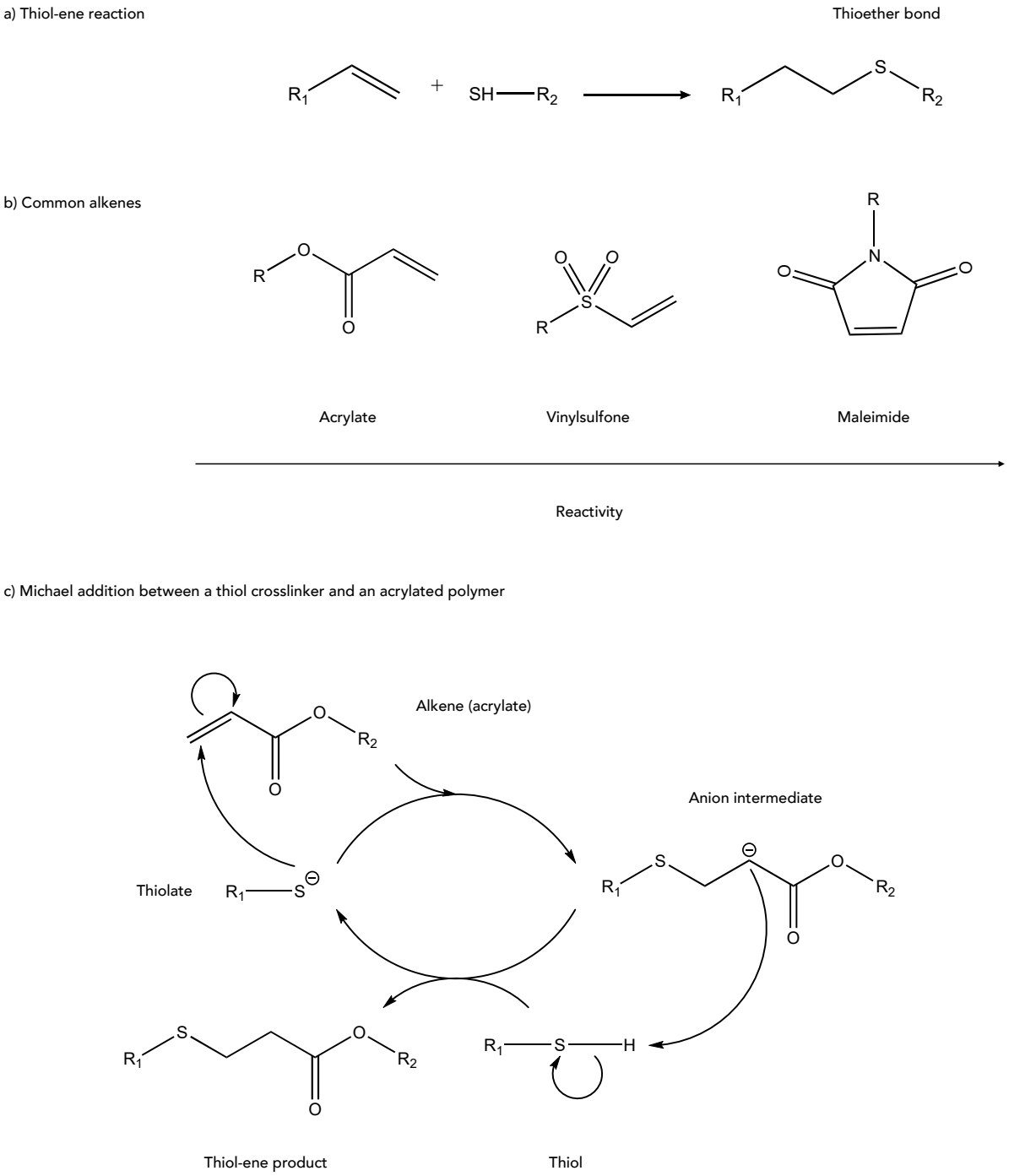


Figure 7: Michael addition-mediated thiol-ene reaction. a) Thiol-ene reaction. A thiol group reacts with an alkene to form a thiol-ene product comprising a thioether bond. b) Common alkenes. Acrylate, norbornene, vinylsulfone and maleimide groups are common alkenes used to functionalised polymers. Reactivity will be dependent on the environment and other groups surrounding the double bond. c) Michael addition between a thiolated crosslinker and an acrylated polymer. A thiolate anion, that acts as a nucleophile, attacks the electrophilic β-carbon of the alkene to form a carbon-centred anion intermediate. The latter can then abstract a proton from a conjugate acid to generate the thiol-ene product. R1 and R2 are the polymer backbone.

The second type of reaction is the Michael-type addition (Figure 7.c). This reaction occurs under ambient conditions with negligible amounts of catalyst, which is generally a base or a nucleophile. In thiol-ene Michael additions, a base abstracts a proton from a thiol, forming a thiolate anion that acts as a nucleophile and attacks the electrophilic β-carbon of an alkene to form a carbon-centred anion intermediate. The latter can then abstract a proton from a conjugate acid to generate the thiol-ene product, regenerating the original base and allowing for the reaction to continue until one of the reactive functional groups is consumed. The Michael addition produces fewer structural defects in the network and provides more precise control over the gel crosslinking density and material properties [165]. In addition, this reaction does not require radicals and is typically free of byproducts, making it a good candidate for protein, cell and EV encapsulation.

3.2.3. Degradable hydrogels for drug delivery

PEG-based crosslinked hydrogels exhibit a variety of highly tailorable properties, including crosslinking kinetics, mechanical properties (*e.g.* stiffness), porosity, and degradability. These can be tuned depending on the polymer and the manufacturing process used and optimised for controlled therapeutic delivery [166-169]. Hydrogel biodegradation is attractive as means of both releasing the therapeutic cargo over time and eliminating the implanted materials from the tissue following delivery. PEG is not intrinsically biodegradable. However, degradability can be conferred to PEG-based hydrogels using blends or crosslinkers that are susceptible to hydrolysis, photodegradable or enzyme-sensitive [167-170] (Figure 8).

Hydrolysis is the most commonly used degradation mechanism in hydrogels, in which a molecule of water causes scission of functional groups, such as anhydrides, esters and amides. In order to obtain hydrolytically-degradable PEG hydrogels with physiologically-relevant degradation kinetics, researchers typically use blends of PEG and hydrolysis-sensitive polymers, such as poly(lactic acid) (PLA), poly(glycolic acid) (PGA) or poly(caprolactone) (PCL) [171]. Alternatively, hydrolysis can act on the PEG crosslinkers. For example, ester bonds are present in the polymer backbone when using acrylated polymers

for crosslinking, which can enable hydrogel degradation without the need to introduce another polymer. While hydrolysis is an effective strategy for sustained hydrogel degradation and release of therapeutic agents, the rate of degradation is relatively slow *in vitro* and *in vivo* [172] and cannot be tuned once the hydrogel is fabricated.

In contrast, using photodegradable linkages allow precise spatial and temporal control over degradation [173]. This method has been used to study cell-material interactions and manipulate cells *in vitro* [174]. Different wavelengths are used including visible, ultraviolet and infrared (IR) light. Using visible and ultraviolet light (UV) to trigger gel degradation is limited by their tissue penetration capacity *in vivo*, meaning it cannot be used on deeper organs, while IR is more cytocompatible and offers better penetration depth [175].

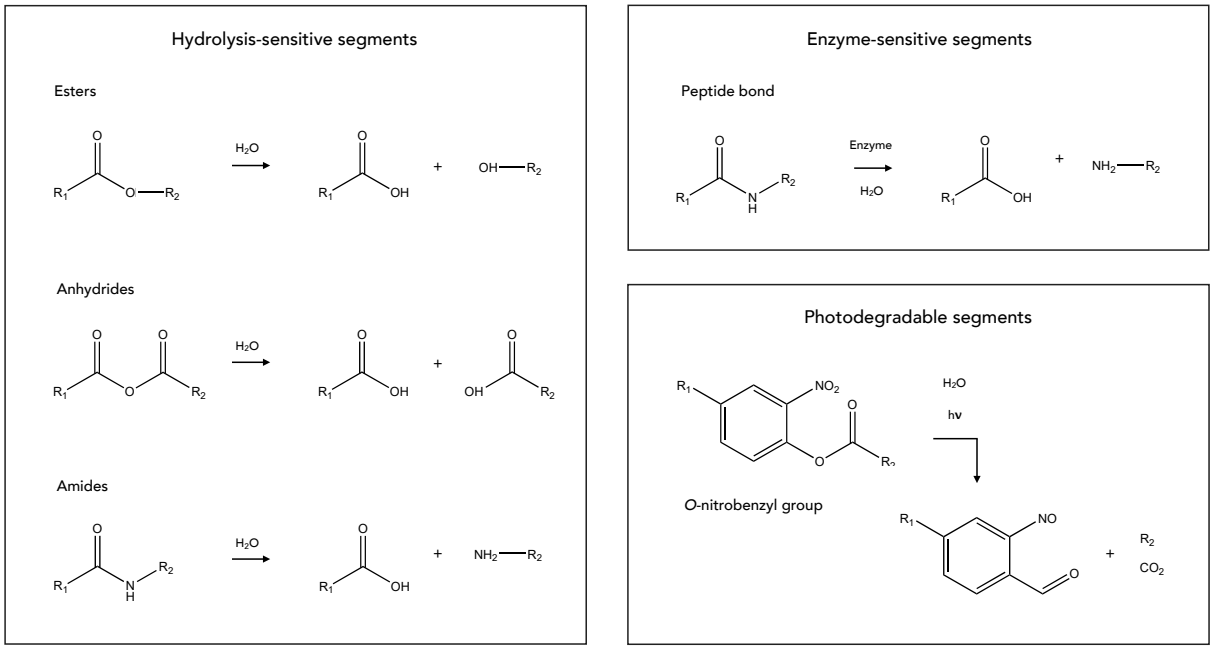


Figure 8: Examples of degradable moieties used in hydrogel-based drug delivery systems. Hydrogels can be made biodegradable using blends or crosslinkers that are susceptible to hydrolysis (*e.g.* esters, anhydrides, amides), enzyme-sensitive (*e.g.* peptide sequence) or photo-degradable (*e.g. o*-nitrobenzyl-based groups).

Using enzyme-degradable segments provides control over the release rate of the therapeutic cargo without the need for an external trigger. Synthetic peptides based on the structure of natural substrates can be incorporated into the hydrogel structure, allowing degradation to be regulated by enzymes naturally present in the target tissue [176]. In

addition, hydrogel degradation rate can be tuned by modifying the crosslinker sequences as well as the ratio degradable/non-degradable linkages. Hubbell and co-workers pioneered this approach by incorporating matrix metalloproteinase (MMP)-sensitive crosslinkers into hydrogels *via* Michael addition [177, 178]. MMP-2 and MMP-9 have been shown to be upregulated in the heart for up to a month after an MI [41, 179, 180]. Utilising a hydrogel that can be degraded by these enzymes could provide an environmentally-sensitive response to aid the kinetics of cargo delivery [181]. Indeed, MMP-2/-9-sensitive crosslinkers have been synthesized and used to create responsive and controlled delivery systems in which degradation is induced by the presence of these enzymes [182].

3.2.4. Drug loading and release from hydrogels

Drugs can be loaded into hydrogels *via* three main strategies, which can be selected depending on the size and biochemical properties of the drug itself as well as the desired release mechanism [183] (Figure 9.a).

Entrapment is the most straightforward method for loading drugs into hydrogels, especially when the pore size is smaller than the drug size. Drugs can be loaded into pre-crosslinked hydrogels using concentration gradients. Although this method is very simple to setup, it does not allow accurate control over the drug loading and release profile [171]. Alternatively, molecules can be loaded *in situ* by mixing with the hydrogel precursors before crosslinking. This method allows relatively easy loading of single or multiple drugs in high amounts within the same hydrogel but bears the risk of undesired reactions between the precursors and the drug. Drug entrapment often comes with a major challenge, which is burst release, a phenomenon in which a portion of the loaded drug is quickly released upon hydrogel implantation [184, 185].

Burst release can be avoided by using the second loading method, drug-polymer tethering, which uses covalent links between the drug and the polymer [171]. In the majority of cases, the drug and/or the polymer need to be modified to incorporate the functional handles that allow conjugation (*e.g.* thiols, acrylates, azides). Functionalization and tethering can result in

reduced bioactivity for the drug [186]. Tethering is often used for therapeutics that are too small to be entrapped or when the diffusion is too rapid for the desired application [183]. Finally, affinity binding can be used to associate the drug with the hydrogel network using reversible interactions such as hydrophobic or electrostatic interactions [183].

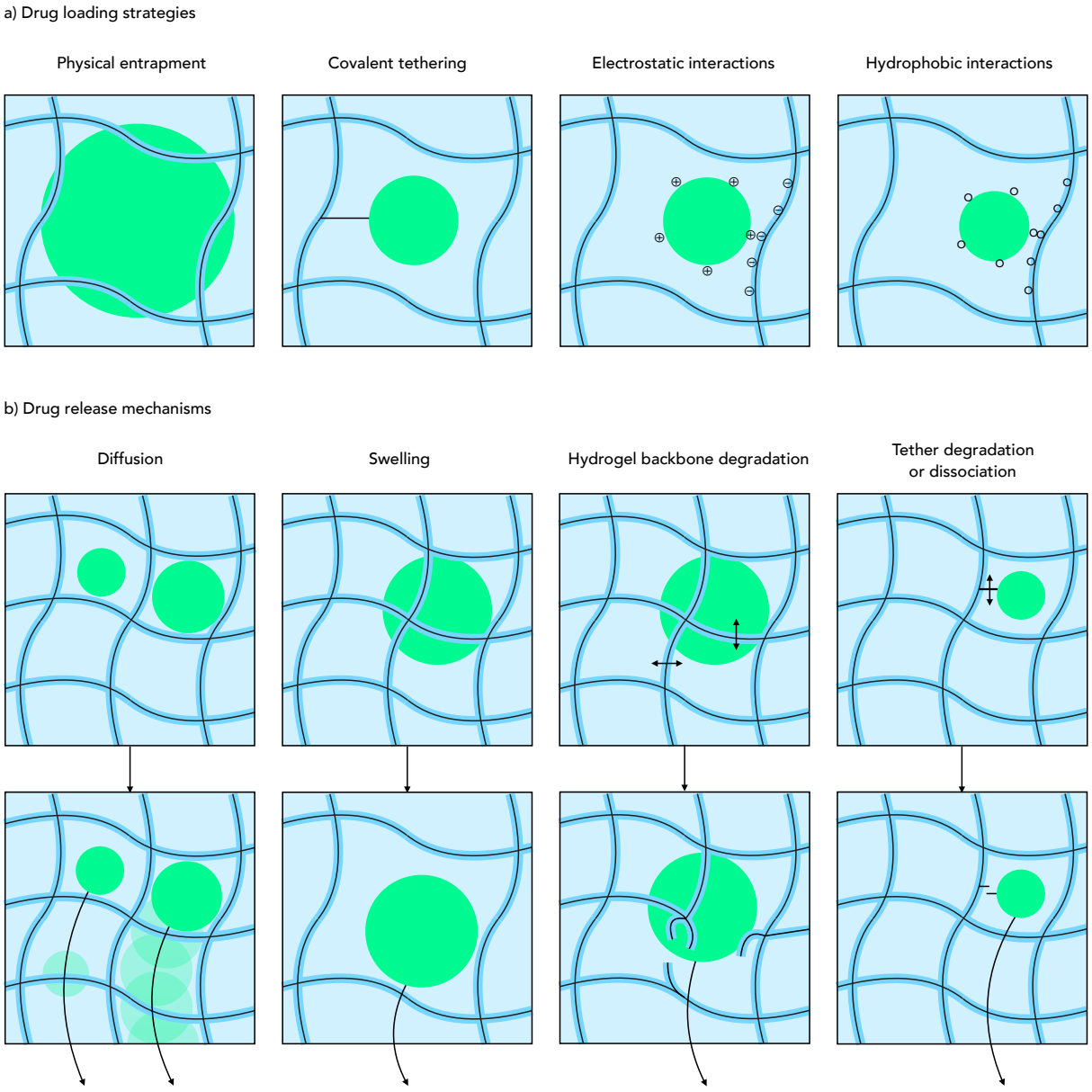


Figure 9: Drug loading and release mechanisms. a) Drugs with a size bigger than the mesh size can be loaded into hydrogels by physical entrapment. Alternatively, drugs can be tethered to the polymer backbone using covalent tethers, electrostatic interactions or hydrophobic interactions. b) Release mechanisms are dependent on the drug size and biochemical properties, the polymer and the loading strategy used. Drugs with a size smaller than the mesh size will be able to diffuse rapidly while drugs with a size similar to the mesh size will have a slower diffusion pattern. For entrapped and tethered drugs, drug diffusion will occur upon swelling of the hydrogel, backbone degradation, dissociation and/or tether degradation.

Release mechanisms are dependent on the drug size, biochemical properties of the drug and the polymer and loading strategy used [183] (Figure 9.b). In all cases, release is completed by Fickian diffusion of the drug through the pores of the hydrogel into the surrounding tissue. Drugs with a size smaller than the mesh size will be able to diffuse rapidly while drugs with a similar size will show slower diffusion patterns. In the case of entrapped drugs, release will occur upon swelling and/or backbone degradation, while tethered drugs will be release through cleavage of the degradable covalent linkages and/or backbone degradation [187]. Finally, for reversibly bound drugs, interactions are typically in a dynamic equilibrium, meaning that a concentration gradient of free drug is formed from the inside to the outside of the hydrogel. As a consequence, release is achieved when the surrounding concentration of drug is lower than the loaded concentration. Additionally, bound drugs can be released in the presence of affinity competitors that challenge the interaction drug/polymer.

3.3. Microgels for heart delivery

3.3.1. Hydrogel delivery approaches for cardiac repair

Hydrogels are commonly used for drug delivery as macroscopic patches that are prepared *in vitro* and implanted onto the epicardium by a surgical procedure [30, 148] (Figure 10). Although this approach can be advantageous for some applications, it may not be the best option for cardiac repair. As discussed in Part 1, administering a treatment by surgery has many implications. Open-chest surgeries are major interventions that require general anaesthesia, heavy post-operative medication and long recovery times, which greatly limits the range of patients that can benefit from such treatments.

An alternative to epicardial patches are injectable hydrogels used in intramyocardial delivery. There are four types of injectable hydrogels. The first one takes advantage of the liquid-to-gel transition to crosslink chemical and physical hydrogels *in situ* after injection of the precursors into the target area [145-147]. Although most gelation triggers used are considered to be compatible with living tissues, injecting chemical reagents into an already

damaged tissue may not be the safest approach, especially when those generate radicals [188]. In addition, the shape of the gel formed is not controllable and consistent between patients, leading to systematic differences in its surface area and degradation profile. Finally, these strategies require the fine tuning of the crosslinking reaction within the tissue to allow for the gelation to happen after the precursors have been injected and before the precursors and cargo are diluted into the extracellular space.

The second type of injectable hydrogels are macroporous hydrogels, which can be prepared *in vitro* and compressed into a smaller volume to be injected into the tissue using a needle. Macroporous hydrogels can be prepared using various methods such as electrospinning, 3D-printing, cryogelation, gas foaming or templating [189]. Although this type of hydrogel can demonstrate the advantage of being prepared *in vitro*, cytotoxicity challenges may arise from solvents and additives used in the preparation processes.

The third category of injectable hydrogels is shear-thinning hydrogels, which can be crosslinked through self-assembly of peptides, proteins, blends, colloidal systems or block copolymers [190]. Shear-thinning hydrogels feature the ability to flow under shear stress (shear-thinning) and recover initial elastic modulus upon relaxation (self-healing). Shear-thinning behaviour allows pre-formed hydrogels with desired physical properties to be delivered by application of shear stress during injection. Although self-healing may be much faster than crosslinking reactions found in *in situ* gelling systems, fine optimisation of the shear-thinning and self healing kinetics are crucial to allow efficient injection while avoiding precursors and drug leakage from the targeted site.

Microgels and nanogels typically consist of spherical gels with a diameter ranging from approximately 10 to 100 nm (nanogels) and 10 to 100 μm (microgels). This category of injectable hydrogels has many advantages over the macroscopic hydrogels discussed above. First, they are produced and combined with therapeutic drugs *in vitro* before their administration as an off-the-shelf product, which provides opportunities for quality control testing and prediction of the drug release kinetics. They can be delivered by a simple injection without inducing any shear stress that could potentially damage the therapeutic

cargo and provide a fast response to environmental changes. Finally, they may be able to better conform to the targeted tissue and may be less prone to capsule formation compared to macroscopic hydrogels that are more invasive to the tissue [155]. Microgels are particularly interesting for drug delivery as they can be loaded with significant amounts of large elements such as EVs. They are also large enough not to diffuse or be phagocytosed [191, 192].

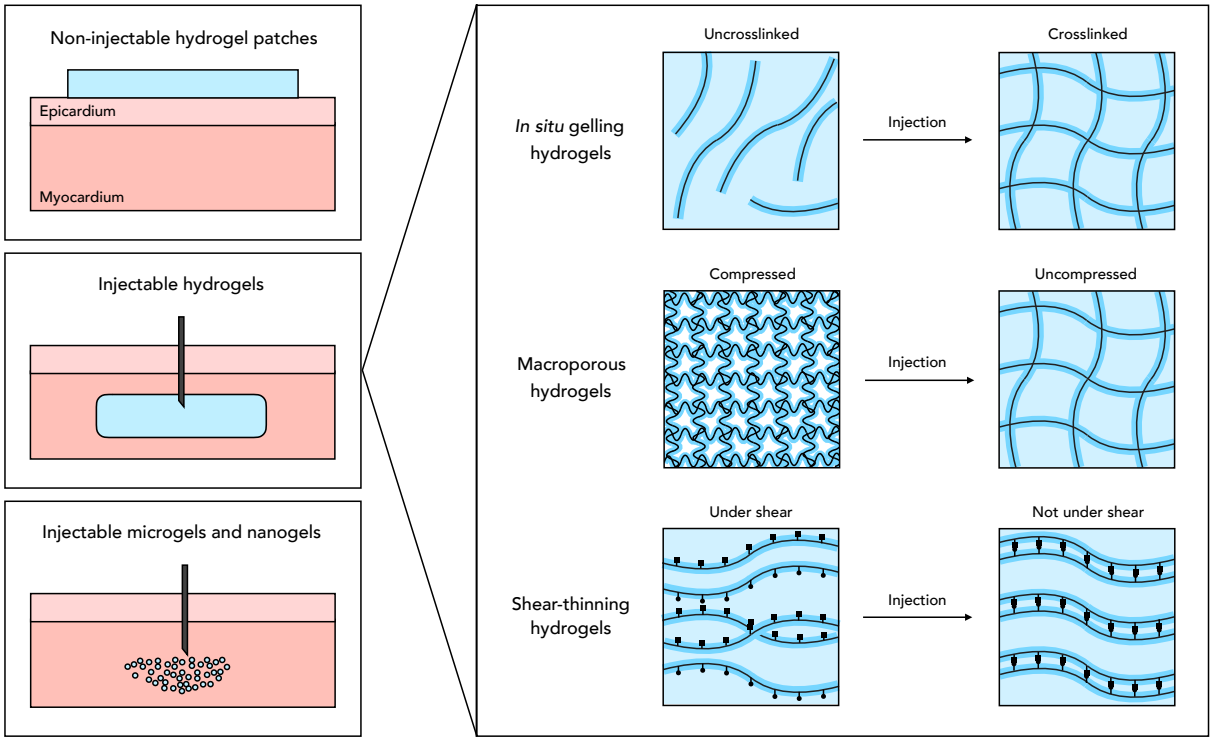


Figure 10: Hydrogel delivery approaches. Pre-made hydrogels can be surgically implanted *in vivo* (*e.g.* epicardial patch). Alternatively, minimally invasive approaches have been developed. The hydrogels precursors can be injected in the tissue for *in situ* gelation. Macroporous hydrogels can be compressed into a smaller volume to allow their insertion into the tissue. Shear-thinning hydrogels become injectable upon application of of shear stress and self-heal within the tissue. Injectable microgels and nanogels can be prepared *in vitro* and injected as is in the tissue.

3.3.2. Microgel fabrication processes

Microgels can be fabricated using various methods that can be selected depending on compatibility with chosen chemistry and crosslinking method (Figure 11). Emulsification can be used in which an aqueous phase containing the hydrogel precursors is mixed with an oil phase. A water-in-oil microemulsion can be stabilised using a small amount of surfactant, and the microdroplet can be crosslinked to form microgels. This method allows for the

production of industrial-scale microgel batches and the average particle size can be tuned by changing the mixing and surfactant concentration. However, the microgel size is generally polydisperse [193, 194]. This can be addressed by using microfluidics, a method in which microdroplets are formed continuously using a microfluidic chip and collected into a reservoir once crosslinked. Although this method is not as high-throughput as bulk emulsification, it offers higher control over the microgel size and is excellent for making highly monodisperse particles [195].

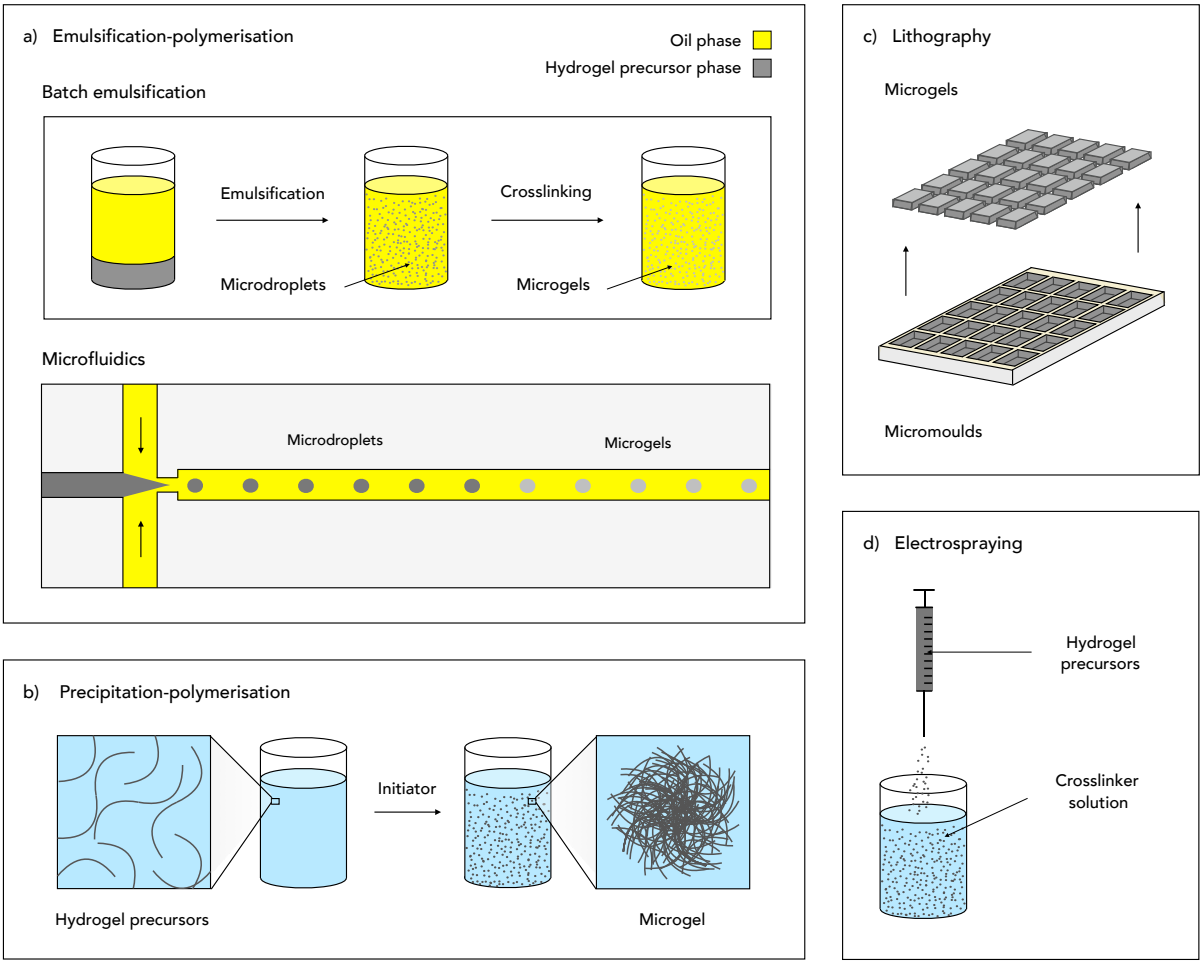


Figure 11: Main methods used for microgel fabrication. a) Emulsification-polymerisation uses an oil phase and an aqueous phase containing the hydrogel precursors to make a water-in-oil microemulsion in which the microdroplets crosslink to form microgels. Large amounts of microgels can be prepared *via* batch emulsification (top), while highly monodisperse microgels can be prepared using microfluidics (bottom). b) In the precipitation-polymerisation methods, a small amount of initiator is added to a hydrogel precursors solution, leading to the formation of small microgels ranging from 100 nm to 5 µm in diameter. c) Microgels of various size and shape can be prepared by lithography using micromoulds in which the hydrogels precursors are crosslinked. d) Electrospraying can be used to form ionic microgels simply by spraying polymer into a crosslinker solution.

An alternative method is precipitation polymerisation, in which the polymer and crosslinker are dissolved in an aqueous phase. Crosslinking is triggered by addition of a small amount of initiator, which induces nucleation of particles. Although this method is often used for producing small particles ranging from 100 nm to 5 μm, it cannot be used to form larger microgels [196, 197]. Larger particles can be made using lithography, a method in which hydrogels are templated using moulds. This technique is often used in combination with photo-polymerisation (photolithography). Although this method is particularly low throughput, it offers the possibility to form microgels that can be shapes other than spheres, which cannot be achieved with other methods [198]. Finally, electrospraying can be used to form ionic microgels simply by spraying polymer into a crosslinker solution. This method is widely used for making alginate microgels as it is relatively easy to implement and does not require any specific equipment [199].

3.3.3. Microgels for drug delivery in heart repair

Microgels have been used to deliver a variety of therapeutic cargos, including cells [200], growth factors [201], small molecules [202], polymeric nanoparticles [203] and bioactive lipids [204]. However, only a few preclinical studies have reported their application as delivery systems for heart repair, including five in large animal models (Table 8). With regards to cell embedding strategies, two preclinical studies demonstrated that the administration of alginate-encapsulated engineered human MSCs into failing pig hearts resulted in a functional improvement and a reduced infarct size [200, 205]. Two other studies reported the use of microgels as carriers for therapeutic proteins in porcine models of IHD and showed that sustained release of basic fibroblast growth factor (bFGF) with or without vascular endothelial growth factor (VEGF) from alginate-based microgels resulted in an improvement in myocardial perfusion [201, 206]. These findings are evidence of the feasibility of using microgels and provide insight into the potential efficacy of such treatments.

Although microgel-based delivery systems have been used to deliver synthetic liposomes [207-209], they are yet to be widely applied to the EV field. To the best of our knowledge,

only one study has to date looked at loading EVs into microgels [210]. Published in 2019, this study showed the feasibility of entrapping osteoblast-derived EVs in alginate microgels fabricated using an electrospraying technology. These degradable microgels were shown to be able to sustainably release the EVs *in vitro* over a period of twelve days by diffusion through the pores, independently of any external trigger. Other publications reported the encapsulation of EVs into hydrogels for multiple applications, including bone and cartilage regeneration [211, 212] and limb ischemia [213]. Interestingly, no publications have yet reported the association of EVs and hydrogels for delivery to the heart.

Table 8: Preclinical studies using injectable microgels as drug delivery systems for heart repair.

Material	Microgel fabrication	Cargo	Delivery route	Model	Ref
Cell delivery					
PNIPAM	Batch emulsion-polymerisation	Cardiac stromal cells	Transepicardial intramyocardial injection	Mouse	(215)
Gelatin	Batch emulsion-polymerisation	Cardiac progenitor cells	Transepicardial intramyocardial injection	Mouse	(216)
Alginate	Not disclosed	GLP-1 producing mesenchymal stem cells	Intracoronary infusion	Pig	(200, 205)
Protein delivery					
Alginate	Electrospraying	bFGF/VEGF	Epicardial attachment	Pig	(201)
Alginate	Electrospraying	bFGF	Not disclosed	Pig	(206)
Gelatin	Batch emulsion-polymerisation	IGF-1/VEGF	Transepicardial intramyocardial injection	Rat	(214)
Alginate	Electrospraying	IGF-1/HGF	Transepicardial intramyocardial injection	Rat	(217)
Gelatin	Batch emulsion-polymerisation	bFGF	Comparison of multiple routes	Rat	(218)
Gelatin	Batch emulsion-polymerisation	bFGF	Transepicardial intramyocardial injection	Rat	(219)
Gelatin	Batch emulsion-polymerisation	bFGF	Transepicardial intramyocardial injection	Dog	(220)

The discovery of EVs has opened new avenues for the development of novel cell-free regenerative therapies. Adequate bioavailability within the targeted tissue may be achieved by their entrapment into biodegradable hydrogels. EVs loaded into PEG hydrogels formed

by a Michael addition thiol-ene reaction could be released by hydrolysis of ester bonds present on the polymer backbone followed by Fickian diffusion of the EVs through the pores. In addition, incorporating MMP-degradable moieties provides enhanced stimuli-responsive release capabilities. Finally, using injectable microgels as an EV delivery system for heart repair could reduce the risks for the patient, facilitate the administration procedure for the doctor and allow researchers and industries to reach a broader spectrum of patients, including acute MI patients.

Chapter 2 Microfluidic platform for the fabrication of monodisperse injectable PEG microgels

1. Introduction

As mentioned in Chapter 1, microgels can be prepared using emulsion-polymerisation, a method in which an aqueous phase containing the hydrogel precursors is mixed with an oil phase to form a water-in-oil microemulsion. In such systems, the aqueous microdroplets are the dispersed phase and can be stabilised within the continuous oil phase using a small amount of surfactant [221] before they are crosslinked to form microgels. Microfluidics-based emulsification methods are advantageous for the fabrication of highly monodisperse microgels, which can be used to encapsulate drugs and cells [195, 210, 222]. Microfluidics-based methods can be subdivided into two categories [223]. In passive methods, the simple introduction of an immiscible fluid into another leads to the formation of droplets. Active methods, on the other hand, are aided by an additional energy input. More specifically, droplet generation can be manipulated by applying additional forces (*e.g.* electrical, magnetic, thermal) or modifying intrinsic forces (*e.g.* fluid velocity, viscosity, interfacial tension, density).

For both categories, microdroplets are generally formed by the injection of two immiscible phases into microfluidic chip comprising a droplet generation junction. This junction can present different geometries [224] (Figure 12). In cross-flow systems (or T-junctions), the aqueous phase is injected into the oil phase at an angle. This geometry was first proposed by Thorsen *et al.* in 2001 [225] and is now the most widely used type of junction. In co-flow geometries, the oil phase channel surrounds the aqueous phase channel, resulting in the two streams meeting in parallel at the droplet generation junction. Finally, in flow-focusing junctions (FFJs), the two phases are hydrodynamically focused, which causes the aqueous phase to be squeezed by the oil phase from two opposing channels. With this last geometry, microdroplet size is determined by the relative flow rates, as well as the channel dimensions, phase viscosities and surfactant concentration [221, 222, 226]. This multitude of parameters offers a high level of control over microdroplet size and allows for the formation of smaller microdroplets compared to other geometries [223].

The development of a microfluidics-based platform for the production of monodisperse injectable PEG-based microgels is presented in this chapter. More specifically, the design of a microfluidic chip comprising a FFJ as well as the methods used for its fabrication were optimised to allow the reproducible fabrication of monodisperse microgels with a diameter between 20 and 100 µm. The effect of the relative flow rates, the concentration of surfactant and the microfluidic setup on microgel size and dispersity was investigated. Because large amounts of microgels are required for *in vitro* and *in vivo* studies, emphasis was placed on tailoring the setup to ensure the production of microgels with high yields. Finally, a protocol for transferring the fabricated microgels into an aqueous phase was developed to provide adequate microgel storage and usage conditions.

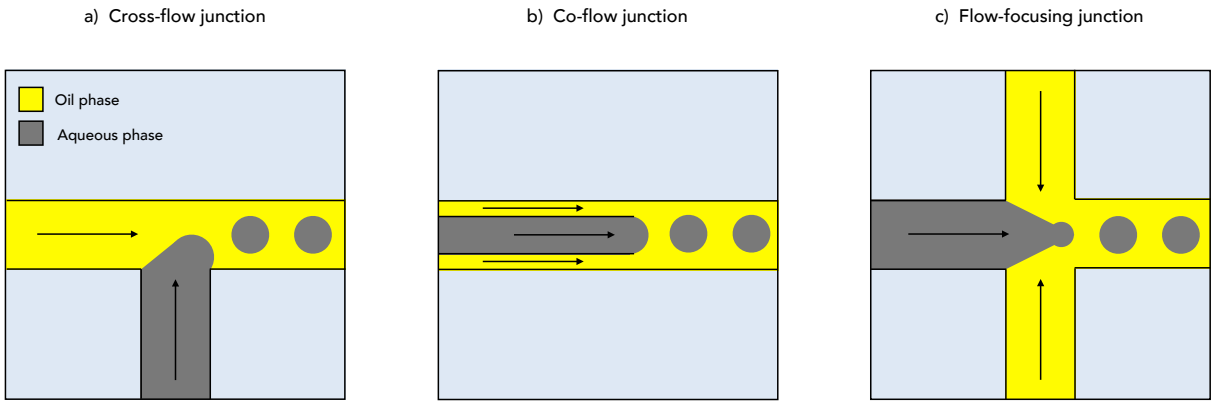


Figure 12: Types of microfluidic droplet generation junctions used for the preparation of water-in-oil microemulsions. a) In cross-flow junctions, the aqueous phase is injected into the oil phase at an angle. b) In co-flow junctions, the oil and aqueous phases streams meet in parallel. c) In flow-focusing junctions (FFJs), the two phases flow are hydrodynamically focused to form microdroplets.

2. Materials and methods

2.1. Materials

Dimethyl sulfoxide (DMSO) (41639), HEPES solution 1M (H0887), hydrochloric acid (HCl) solution 1.0 N (H9892), mineral oil (M5310), PEG dithiol crosslinker (717142, average M_n 1000), sodium acetate buffer solution 3M (S7899), sodium chloride (NaCl) solution 5 M (S5150), sodium hydroxide (NaOH) solution 1.0N (S2770), Span® 80 (S6760) and Trichloro(1H,1H,2H,2H-perfluorooctyl)silane 97% (448931) were purchased from Sigma-Aldrich. Alexa Fluor™ 488 C5 Maleimide (A10254, MW 720.66), Antibiotic-Antimycotic (A/A) 100X (15-240-062), phosphate-buffered saline (PBS) without calcium and magnesium 1X (14-190-144), isopropyl alcohol (IPA) (33539), Penicillin-Streptomycin (P/S) 10,000 U/mL (15-140-148) and *n*-pentane 99+% extra pure (170070025) were purchased from Fisher Scientific. 8-arm PEG-acrylate (tripentaerythritol) (MW 20740) was purchased from JenKem Technology USA. SYLGARD™ 184 Silicone Elastomer Kit (634165S) was purchased from VWR. Photoresist SU-8 2150 and SU-8 developer were purchased from MicroChem. VeroClear was provided by the 3D-printing facility. Aquapel glass treatment was purchased from Amazon UK.

2.2. Methods

2.2.1. Mould fabrication using 3D printing (mould v.1)

Mould v.1, which contained 8 type-1 chips in a tray, was designed on SolidWorks® (Dassault Systèmes) and an STL file was generated. The mould was 3D printed with VeroClear material using a Connex3 Object500 3D printer (Stratasys). Printer specifications include a horizontal layer thickness down to 16 µm and a typical deviation from STL dimensions of ±100 µm for dimensions under 100 mm. Mould v.1 was then treated with Aquapel to form a hydrophobic coating.

2.2.2. Mould fabrication using photolithography (mould v.2)

A 2D negative mask of mould v.2, which comprised 14 type-2 chips, was designed on SolidWorks® and sent as a DWG file to JD Photo Data. A negative 101.0 x 101.0 x 1.5 mm low-reflective, chrome-coated glass photomask was fabricated and used to prepare an SU-8 master *via* UV photolithography. Master preparation was performed by Michele Becce (Imperial College London). A silicon wafer (boron p-doped, resistivity 1-30 Ω m, 4'' diameter, University Wafers) was oxygen-plasma cleaned at 300 W for 5 min. The wafer was then spin-coated with photoresist SU-8 2150 at 1800 rpm for 30 s. This was followed by soft-baking, which was performed in two steps: first, at 65°C for 6 min, then at 95°C for 40 min (both steps on hotplates, by Heidolph and UniTemp, respectively). After the second step, the wafer was quenched at room temperature (RT), for 1 min. The mask pattern was transferred to the photoresist using an MA6 mask aligner (Suss Microtec), with UV light for a total of 40 s at 7.09 mW/cm^2. A post-exposure bake was then performed, in two steps: first, at 65°C for 5 min, then at 95°C for 13 min (both steps on hotplates, by Heidolph and UniTemp respectively). This was followed by development in SU-8 developer, first for 15 min, oscillating the solution on a rocking platform (VWR), then for 1 min, static, in fresh SU-8 developer. The patterned wafer was then washed with IPA and blow-dried with N_2. The in-plane dimensions of the developed photoresist features were checked with an optical microscope (Nikon), while the height of the features was checked with a Dektak 6M stylus profiler (Veeco). The patterned wafer was baked at 130°C on a hotplate (Stuart) for 15 min, oxygen plasma-treated (0.5 mbar, power setting of 4.5 for 2 min) (Plasma Prep 5, Gala-Instruments) and vacuum-coated with trichloro(1H,1H,2H,2H-perfluorooctyl)silane 97% and adhered to a plastic dish to form mould v.2.

2.2.3. Chip fabrication using soft lithography

Chips were fabricated by soft lithography using SYLGARD™ 184 Silicone Elastomer Kit, a two-part polydimethylsiloxane (PDMS)-based elastomer (Figure 13). A 10:1 weight ratio mixture was prepared with the base elastomer and curing agent, and poured into the mould to form a layer approximately 3 mm thick. The layer was then degassed in a vacuum

desiccator and cured in an oven (Memmert) at 60°C for 90 min to form the top patterned layer of the chips. The layer was peeled off the mould and the individual chips were cut to size and perforated to form the inlets and outlet using a biopsy punch (Miltex® 1 mm D6345 from Williams Medical Supplies for the inlets, Core sampling tool 0.5 mm 69039-05 from Electron Microscopy Sciences for the outlet). A 2 mm-thick bottom unpatterned layer was prepared by adding the same mixture to a large plastic dish. This layer was degassed in a vacuum desiccator and cured in an oven (Memmert) at 60°C until slightly sticky (approximately 40 min). Chips were then assembled by placing the top patterned layers facing down onto the slightly sticky bottom unpatterned layer. The assembly was placed in an oven (Memmert) at 60°C to finish curing and seal the two layers of the chips. Finally, individual bilayered chips were cut to size and peeled off the plastic dish.

2.2.4. Preparation of oil and aqueous phases

Optimisation of the oil phase composition is described in 3.3.2. Briefly, an oil phase was prepared by mixing various amounts of Span® 80 (sorbitane monooleate) with mineral oil, with the solution stored at RT. Optimisation of the composition of the hydrogel precursors solutions is described in Chapter 3. A HEPES buffer was prepared with 150 mM HEPES and 75 mM NaCl in MilliQ water, with the pH adjusted to 7.4 using NaOH and HCl solutions. A sodium acetate buffer was prepared with 10 mM sodium acetate and 140 mM NaCl, with the pH adjusted to 5.0 using NaOH and HCl solutions. Both buffers were stored at 4°C. A 1 mM stock solution of Alexa Fluor™ 488 C5 Maleimide was prepared in DMSO, stored at -20°C and used at a final concentration of 10 nM to make fluorescent microgels. The hydrogel composition was set to 10 wt% polymer with a thiol:acrylate crosslinking molar ratio of 1:1. The PEG-acrylate solution was prepared by dissolving the 8-arm PEG-acrylate 20K polymer in HEPES buffer. The PEG dithiol crosslinker solution was prepared by dissolving PEG dithiol crosslinker in sodium acetate buffer, and adding Alexa Fluor™ 488 C5 maleimide.

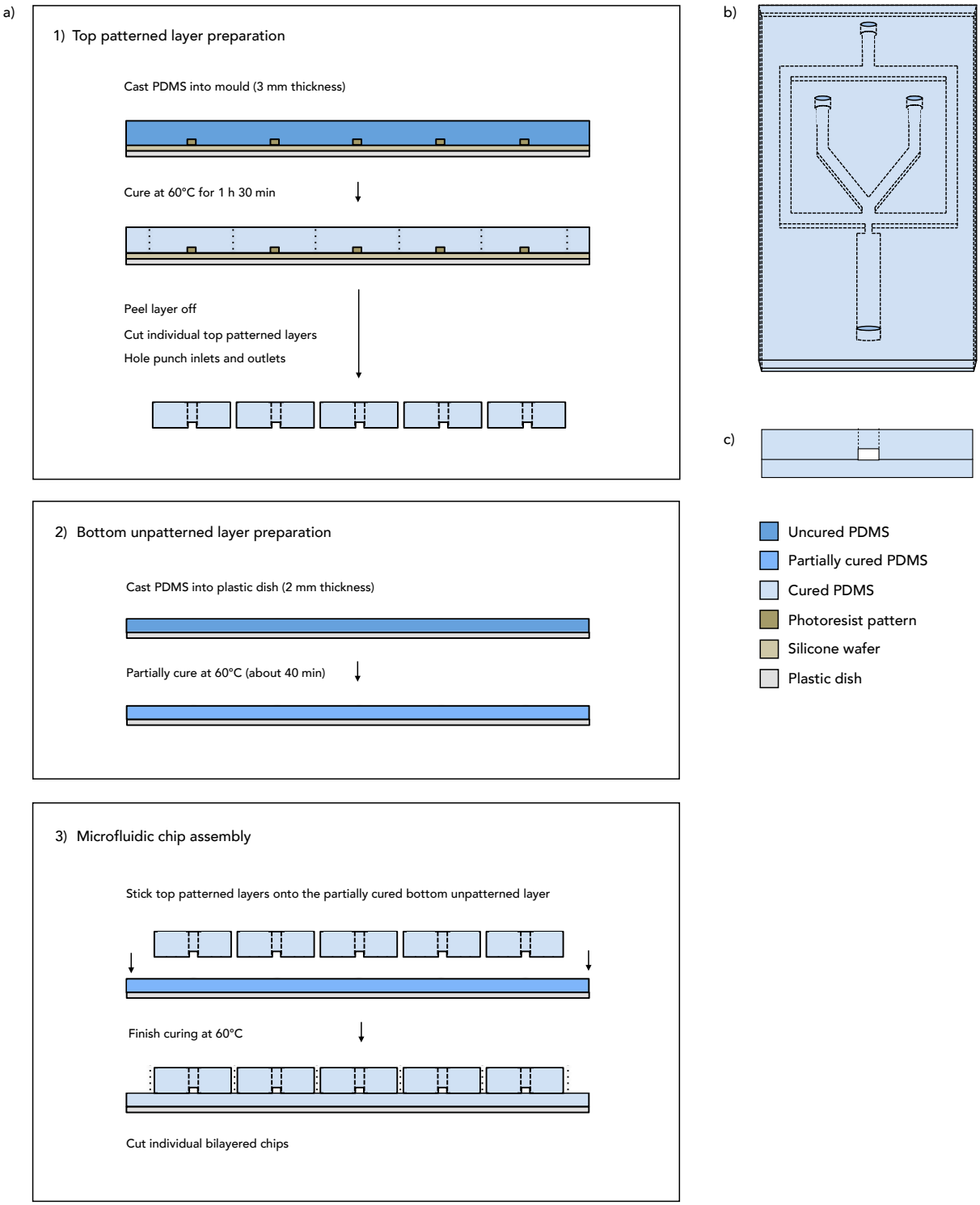


Figure 13: Microfluidic chip fabrication using soft lithography. a) Steps of the fabrication of the patterned and unpatterned sides followed by their assembly to form a microfluidic chip. b) Top view of the chip showing the flow focusing pattern and c) cross-section of a microfluidic chip.

2.2.5. Microgel fabrication using type-2 chips

A schematic of the microfluidics platform is provided in Figure 14. The microfluidic chip was set-up onto a microscope glass slide under an inverted microscope (objective x10, Olympus) to allow visualisation of the channels. A 25 mL Hamilton Gastight glass syringe (26212, Sigma Aldrich) filled with the oil phase was attached onto a first Fusion 100 Touch dual-channel syringe pump (KR Analytical) and connected to the chip using a tubing connector and a 50 cm-long piece of tubing (15249134, Portex Fine Bore LDPE tubing 800/100/120, Smiths Medical, OD 1.09 mm, ID 0.38 mm, Fisher Scientific). The oil phase flow rate was set to 100 µL/min to fill and prime the chip channels, and reduced to the desired final value. The outlet tubing (10793527, Portex Fine Bore LDPE tubing 800/100/100, Smiths Medical, OD 0.61 mm, ID 0.28 mm, 0.5 to 3.5 m length, Fisher Scientific), which was wrapped around a 100 mL borosilicate 3.3. glass bottle (VWR) to keep it in place, and then connected and the system was run for approximately 5 min to allow the outlet tubing to be filled and the flow to stabilise. Two 500 µL glass syringes with a 22G blunt needle (509914, Sigma Aldrich) containing the hydrogel precursor solutions were assembled on a second Fusion 100 Touch dual-channel syringe pump (KR Analytical) and connected to the chip using tubing connectors and 50 cm-long pieces of tubing (15249134, Portex Fine Bore LDPE tubing 800/100/120, Smiths Medical, OD 1.09 mm, ID 0.38 mm, Fisher Scientific). The hydrogel precursor flow rate was set to 2-5 µL/min until microdroplets started forming at the FFJ, and then reduced to the desired final value and left for 10 min to allow the outlet tubing to be filled with the microemulsion and the flow to stabilise. The end of the outlet tubing was placed into a collection tube (Kimax centrifuge tube, Z254851, with polytetrafluoroethylene septa in cap, 27515, Sigma Aldrich) containing 500 µL of oil phase, attached onto a shaking vortex (Fisherbrand™, speed 3) using a foam tube holder. At the end of the microgel collection time (generally 2 h), microgels were left under agitation for another 15 min. Microgels were then washed using the protocol described in 2.2.6. and stored at 4°C until further use. Microdroplet and microgel size were analysed by image analysis (Fiji) of images acquired using an inverted microscope (objective x10, Olympus).

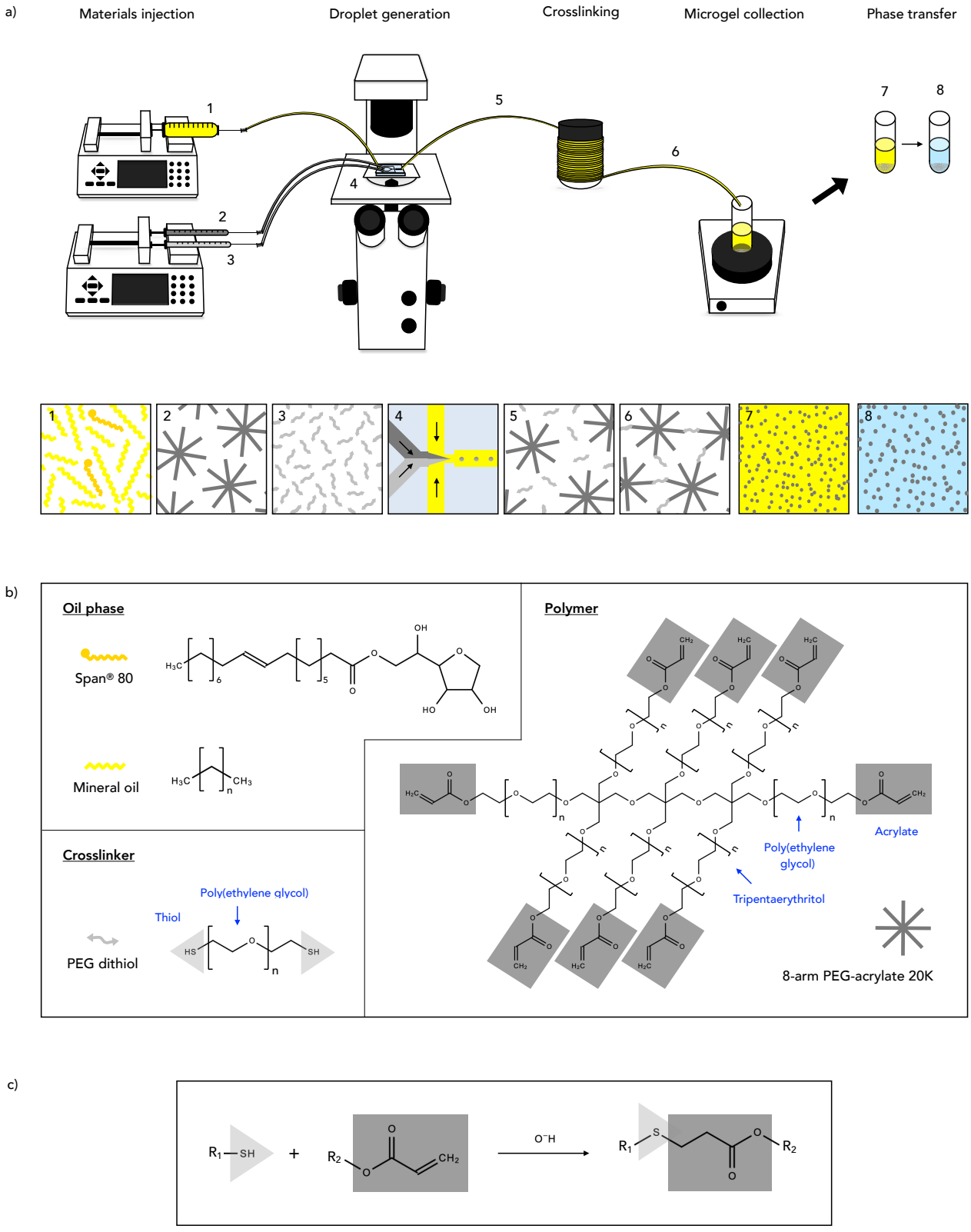


Figure 14: Microfluidic-based microgel fabrication platform. a) Overall schematic of the platform with key elements and steps involved in the microgel fabrication process. The oil phase (1) composed of mineral oil (yellow) and 10% (v/v) Span® 80 (orange) is injected through a first inlet. The two hydrogel precursor solutions are injected *via* separate inlets: the 8-arm PEG-acrylate 20K (dark grey) in HEPES buffer on one side (2) and the PEG dithiol crosslinker (light grey) in sodium acetate buffer on the other side (3). The oil phase and hydrogel precursor streams meet at the FFJ (4) to generate water-in-oil microdroplets. The microdroplets travel within the outlet tubing where they crosslink (5 to 6) to form microgels, which are collected and transferred into an aqueous phase (7 to 8). b) Chemical structure of the hydrogel precursors. c) Thiol-ene crosslinking reaction.

2.2.6. Microgel phase transfer

Microgels, which were collected as a suspension in the oil phase, were subjected to a series of washes. Pentane was added to the collection tube containing the microgel suspension (volumetric ratio 9:1), which was then vigorously shaken and left static for 2 min to allow the microgels to settle to the bottom of the tube. The same volume of supernatant was removed and the sequence of steps (Figure 15.a) repeated 3 more times. At the end of the last pentane wash, PBS containing 1% (v/v) A/A and 1% (v/v) P/S (PBS-antimicrobials) was added to the tube, which was shaken vigorously to aid microgel phase transfer and left for 1 h at RT to let the two phases separate. The top oil phase was then removed, first by aspirating with a pipette and then by letting the residual oil evaporate under a chemical fume hood overnight. This was followed by a 30 min centrifugation at 3000 rpm to pellet the microgels. The supernatant was then removed and the microgels washed a second time in PBS-antimicrobials (Figure 15.b). The final pellet was resuspended in PBS-antimicrobials at a concentration of 10% (v/v).

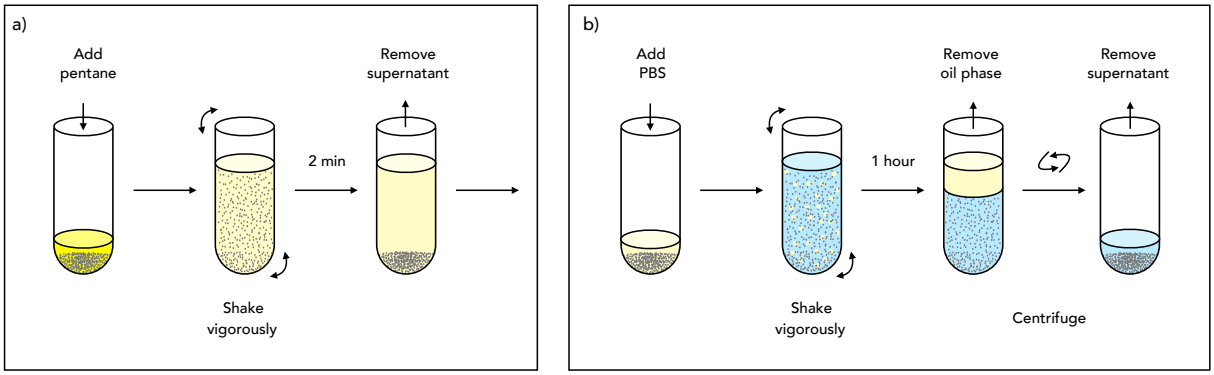


Figure 15: Microgel washing protocol. Microgels were washed four times in pentane (a) followed by two times in PBS-antimicrobials (b). The final pellet was then resuspended in PBS-antimicrobials, at a final concentration of 10% (v/v)

2.2.7. Injectability

The capacity to inject the 10% (v/v) suspension without damaging the microgels was evaluated using two methods. First, images of microgels before and after injection through

a 29G x 12.7 mm needle (0.5 mL MicroFine™+ Insulin syringe, needle inner diameter 184 µm, BD) were taken using an inverted microscope (Olympus, 4X objective lens). Secondly, viscosity measurements were performed on an MCR 302 rheometer (Anton Paar) with a 50 mm sandblasted plate (47708, Anton Paar) and 25 mm sandblasted parallel plate (3997, Anton Paar), using a gap of 100 or 200 µm and a shear rate comprised between 0.01 and 100 1/s.

3. Results and discussion

3.1. Fabrication of mould v.1 and type-1 chips

Mould v.1 was designed to be fabricated by 3D printing. The overall chip geometry was inspired from a report by Siltanen *et al*. [195] (Figure 16). In this geometry, the oil phase is injected through a first inlet, which is connected to a channel that separates into two branches. The two channels run along the sides of the chip before turning at a 90° angle towards the FFJ. The hydrogel precursor solutions, which react upon mixing, are injected into the chip *via* two separate inlets. The two streams are mixed within a serpentine mixing zone leading to the FFJ. The latter was adapted from a publication by Dang *et al.*, which reported the successful fabrication of photocrosslinked poly(ethylene glycol) methyl ether acrylate-based microgels with a diameter of approximately 60-140 µm [227]. Channel dimensions were replicated from the literature except for the orifice width (Figure 16, dimension y), which was set to 100 µm instead of 50 µm to better suit the resolution capacity of the 3D printer. Finally, the FFJ is followed by a wider channel, which allows the microdroplets to stabilise before exiting the chip through the outlet. All features were extruded to a height of 200 µm.

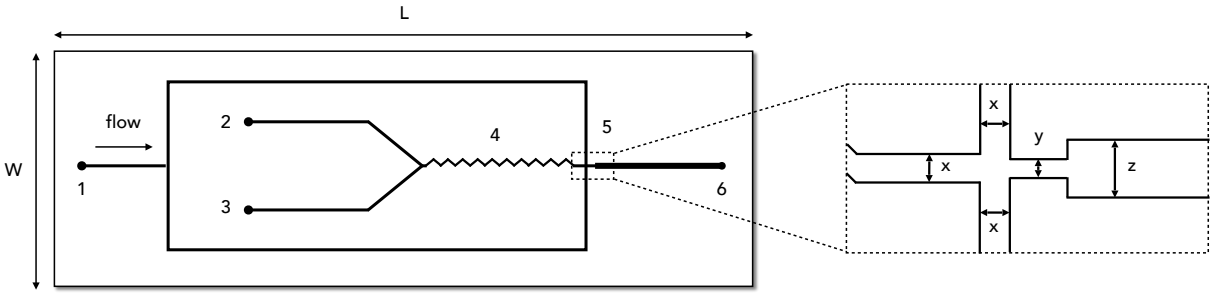


Figure 16: Type-1 chip design. The oil phase is injected through inlet 1 into channels that run along the sides of the chip and turn at a 90° angle towards the FFJ (5). The hydrogel precursor solutions are injected through inlets 2 and 3, mixed within the serpentine mixing zone (4) and squeezed by the oil phase at the FFJ (5) to form water-in-oil microdroplets. These microdroplets exit the chip through the outlet (6). The dimensions of input design of the chip and FFJ are the following: L = 5 cm, W = 2 cm, x = 120 µm, orifice width y = 100 µm, outlet channel width z = 300 µm.

A mould comprising 8 type-1 chip patterns was designed on SolidWorks® (Figure 17.a) and 3D printed (Figure 17.b). Chips were fabricated by soft lithography using PDMS (Figure 17.c). A representative photograph of the resulting FFJ is provided in Figure 17.d. Intended channel dimensions are indicated with discontinuous lines. Chips formed using the 3D-printed mould presented inaccurate features compared to the input design, including uneven and often wider channels, and the absence of an orifice at the FFJ. These results can be attributed to the relatively low resolution of the 3D printer employed to make the mould, which uses a material jetting technology. Higher resolution could be achieved by using a photopolymerisation-based 3D printer, which has been shown to be able to replicate features in the submicron size range [228].

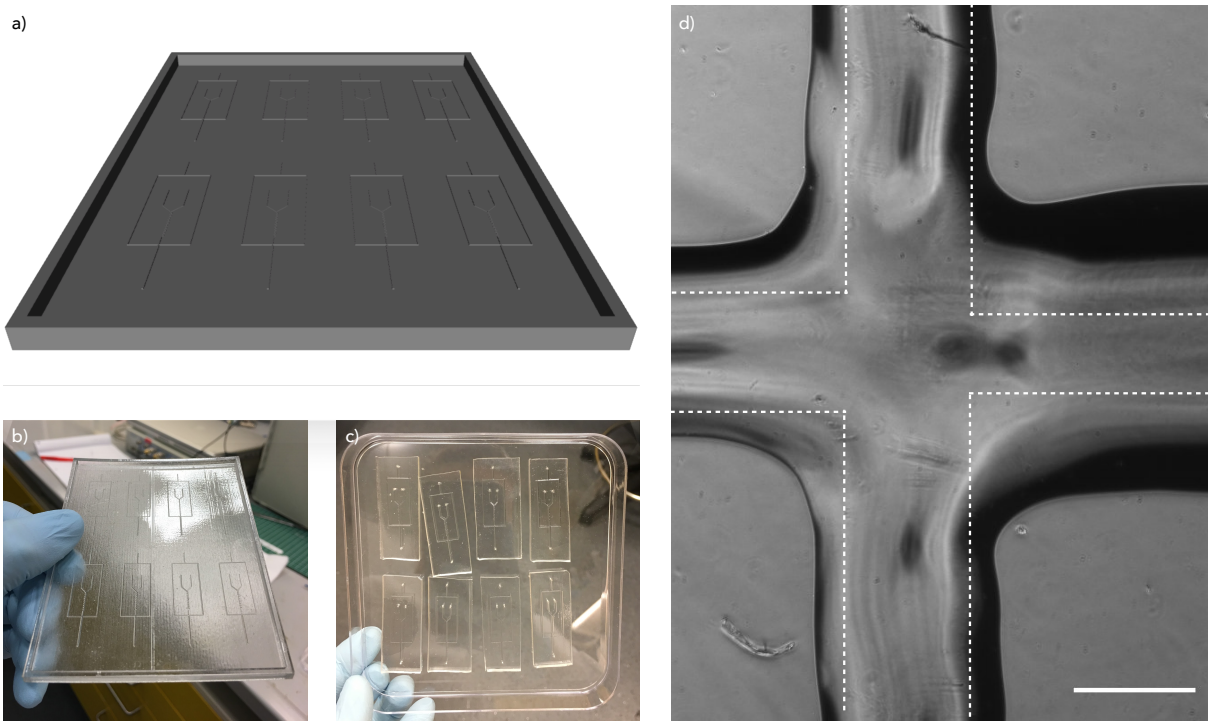


Figure 17: Type-1 mould and chip fabrication. A mould comprising 8 type-1 chip patterns was designed on SolidWorks® (a) and 3D printed (b). Chips were fabricated by soft lithography using PDMS (c). The resulting FFJ geometry presents inaccurate channel dimensions compared to the input design, which is indicated with discontinuous lines (d, scale bar = 100 µm).

3.2. Fabrication of mould v.2 and type-2 chips

A second chip pattern was designed based on the observations made from the type-1 chip (Figure 18). As 3D printing failed to provide appropriate resolution, photolithography was used for type-2 chips; a method offering superior resolution that should allow for more faithful fabrication of the design features during the mould preparation process. The orifice width was thus reduced to the size originally found in the reference publication, of 50 µm [227]. Finally, the serpentine mixing zone located between the intersection of the two hydrogel precursor channels and the droplet generation junction was removed. Although the absence of mixing features before the FFJ could result in the formation of uneven microdroplets, the relatively slow crosslinking kinetics combined with the presence of angles (*e.g.* between outlet channel and outlet tubing) and curvatures (*e.g.* outlet tubing) in the system should enable sufficient mixing prior to microdroplet crosslinking. Removing the mixing zone had two benefits: i) smaller chip size enabled the fabrication of 14 chip patterns in the same mould, instead of 8 with the previous design; ii) reducing the distance between the junction of the two hydrogel precursor channels and the FFJ reduced the chance for the chip to clog by fragments of hydrogel crosslinking before the junction.

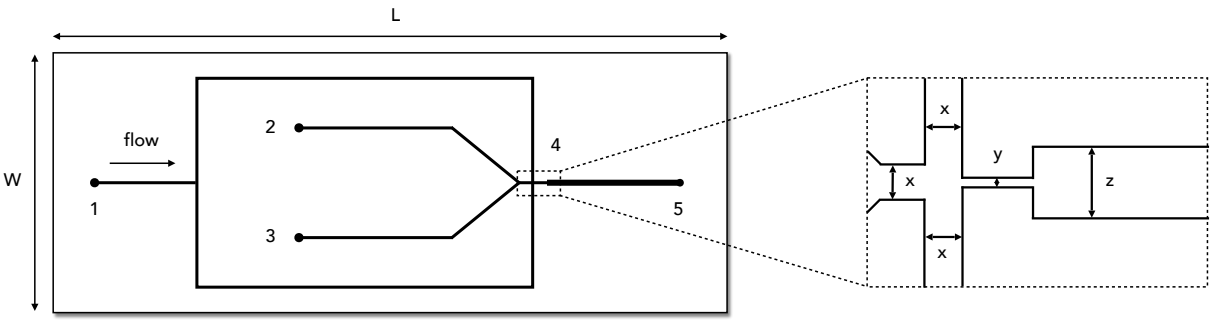


Figure 18: Type-2 chip design. The oil phase is injected through inlet 1 into channels that run along the sides of the chip and turn at a 90° angle towards the FFJ (4). The hydrogel precursor solutions are injected through inlets 2 and 3, and squeezed by the oil phase at the FFJ (4) to form water-in-oil microdroplets. These microdroplets exit the chip through the outlet 5. The dimensions of input design of the chip and FFJ are the following: L = 3 cm, W = 2 cm, x = 120 µm, orifice width y = 50 µm, outlet channel width z = 300 µm.

A photomask comprising 14 type-2 chip patterns was designed on SolidWorks® (Figure 19.a) and used to prepare a patterned silicone wafer using photolithography, with a feature height of 140 µm. The patterned wafer was adhered into a plastic dish to make a mould with elevated edges (Figure 19.b). This mould was then used to prepare microfluidic chips by soft lithography using PDMS (Figure 19.c). This combination of methods allowed the reproducible production of high-quality chips that presented well-defined channels of correct dimensions as seen in the representative micrograph of the FFJ provided in Figure 19.d.

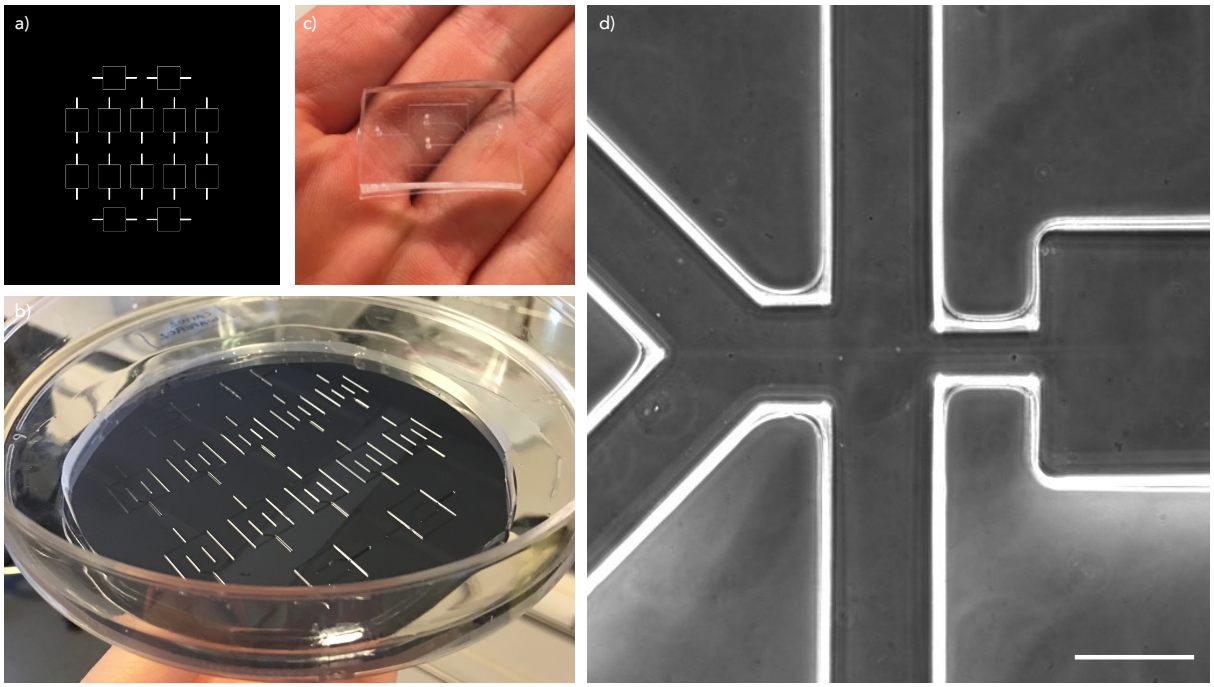


Figure 19: Type-2 mould and chip fabrication. A photomask comprising 14 type-2 chip patterns was designed on SolidWorks® (a) and used to pattern a silicone wafer using photolithography, which was adhered into a plastic dish to form a mould (b). Chips were fabricated by soft lithography using PDMS (c) and showed well-defined and reproducible channels (d, scale bar = 100 µm).

3.3. Microgel fabrication

3.3.1. Microdroplet generation

The aim of the following experiments was to generate stable monodisperse microdroplets that could be crosslinked to form microgels in the targeted 20-100 µm size range. To

account for microgel swelling upon transfer from the oil phase into an aqueous media, the targeted microdroplet diameter was arbitrarily set to 80 µm or smaller.

In flow-focusing-type junctions, microdroplet size is determined by the oil phase flow rate (Q_O), the aqueous phase flow rate (Q_W), their ratio (Q_W/Q_O) and other factors [222, 226]. A fixed amount of surfactant (10% (v/v) Span® 80) and tubing length (2.5 m) were used throughout the following studies. Q_O and Q_W were varied to investigate the possibility of forming microdroplets in the targeted microdroplet size range. Flow instabilities were visually observed with ratios Q_W/Q_O below 0.008. More specifically, the oil phase showed a tendency to flow from the FFJ back into the hydrogel precursor channel. On the other hand, ratios equal to or greater than 0.008 resulted in the formation of microdroplets at the FFJ, of which the size was proportional to the ratio used (Figure 20.a to 20.c). Indeed, this ratio Q_W/Q_O directly determined the amount of each fluid present at the FFJ at a given point in time (t). As a consequence, when the flow rates were changed but their ratio kept constant, microdroplet size did not change. As seen in Figure 20.d, using a ratio Q_W/Q_O of 0.017 resulted in the generation of monodisperse microdroplets in the targeted size range.

In an ideal system where 100% of the hydrogel precursor solution is converted into microdroplets, the yield is directly proportional to the flow rates of the hydrogel precursors. It can thus be calculated by multiplying Q_W by 2, since both precursor solutions participate in droplet formation (Figure 20.e). Producing microdroplets with the highest throughput possible is essential as large amounts of microgels are required for *in vitro* and *in vivo* experiments. Increasing the yield without affecting microdroplet size was achieved by increasing both flow rates while maintaining their ratio. However, this is limited by the capacity of the system to bear the pressure created by the injections of fluids into semi-rigid channels. With Q_W/Q_O between 0.017 to 0.033, it was assumed that the oil phase constituted the majority of the volume flowing through the system, and therefore the effect of varying Q_W could be considered negligible. Setting Q_O above 30 µL/min resulted in a pressure build-up within the chip, causing the tubing to disconnect or the chip to leak. On the other hand, using oil phase flow rates lower than or equal to 30 µL/min led to the continuous formation of monodisperse microdroplets for at least 2 h without any

interruption. Based on these observations, the combination of Q_O = 30 µL/min and Q_W = 0.5 µL/min (Q_W/Q_O = 0.017) was chosen for all following experiments. These parameters resulted in the stable generation of microdroplets with an approximate diameter of 75 µm and a yield of 1 µL/min.

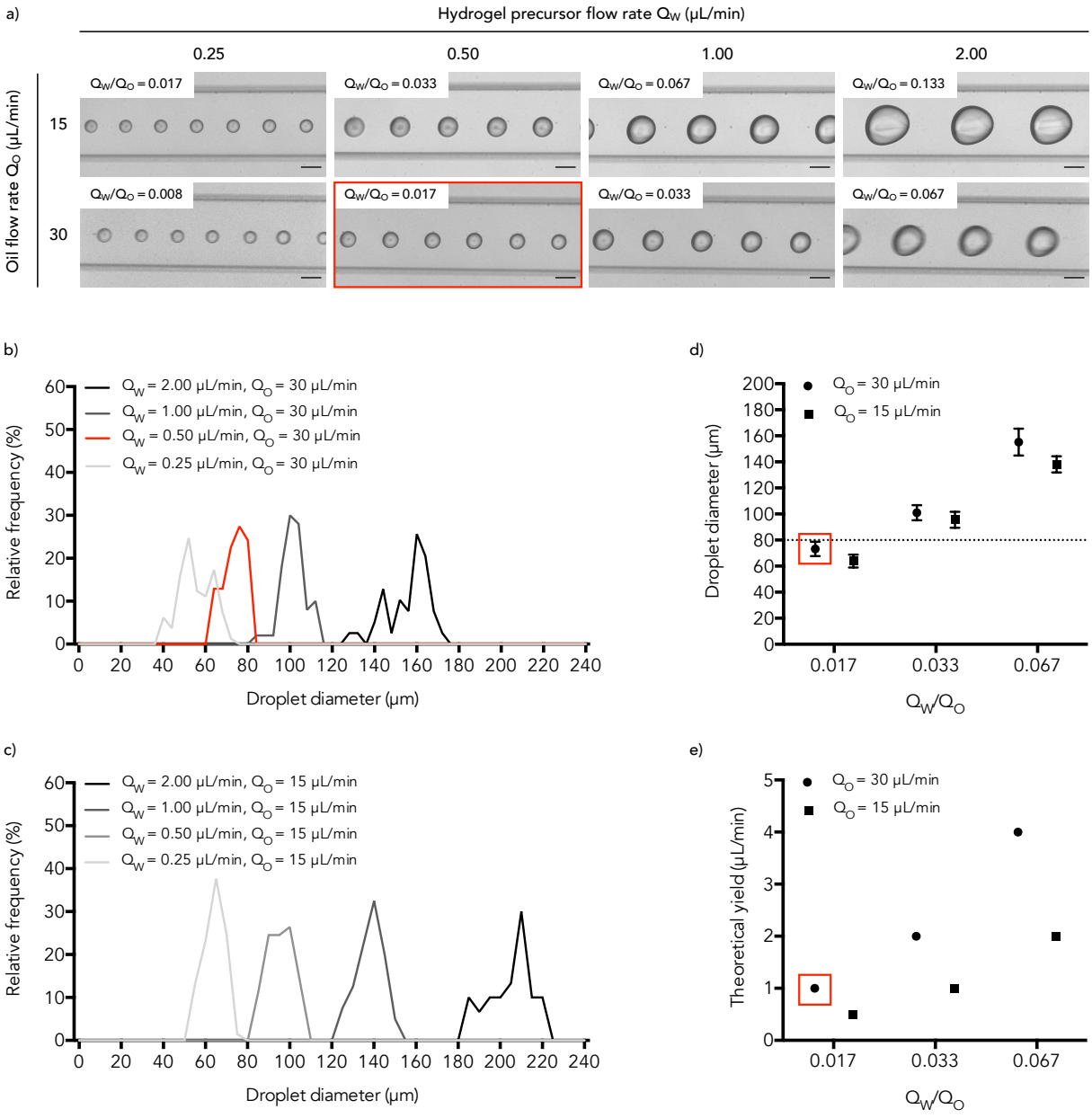


Figure 20: Optimisation of microdroplet generation. Microdroplet size was tuned by varying Q_O, Q_W and Q_W/Q_O. The chosen combination is indicated in red. a) Representative micrographs of microdroplets in the outlet channel. Size of microdroplets assessed by image analysis, formed with an oil flow rate of b) 30 µL/min and c) 15 µL/min. d) Microdroplet size as a function of Q_W/Q_O. The discontinuous lines indicate the targeted microdroplet size. e) Theoretical yield as a function of Q_W/Q_O.

3.3.2. Microdroplet stabilisation and crosslinking into microgels

The ability of the microdroplets to form microgels was then investigated. This required stabilisation of the microemulsion until completion of crosslinking within each microdroplet. The selected hydrogel formulation uses a Michael-type addition between an acrylated polymer and a thiolated crosslinker, a process that is initiated upon mixing of the two hydrogel precursors. Hydrogel crosslinking kinetics optimisation is shown in Chapter 3. The composition of the buffers used to dissolve the polymer and crosslinker was tuned to ensure complete crosslinking within 2 to 10 min. Indeed, a quicker reaction would be at risk of clogging the chip while a longer crosslinking time would require extensive tubing for long-term microemulsion stabilisation.

Two main strategies can be used to aid microdroplet stability. The first method consists of maintaining the microdroplets at a sufficient distance from each other to minimise coalescence. For example, microdroplets can be circulated within microchannels until fully crosslinked [222]. The second strategy consists of modifying the interfacial tension of the microdroplets. Indeed, when two immiscible liquids are mixed together, they tend to keep their interface as small as possible to reduce interfacial energy, which promotes droplet coalescence [221]. Surfactants are amphiphilic molecules that bridge the fluid interface and decrease the surface tension [221]. The microdroplets were stabilised for the time required for them to crosslink, by adding a small amount of surfactant to the oil phase and using a long outlet tubing. A lipophilic surfactant, Span® 80, was used to stabilise the water-in-oil microemulsion. Four tubing lengths (0.5, 1.5, 2.5 and 3.5 m) and three Span® 80 concentrations (0, 5 and 10% (v/v)) were tested. Q_W and Q_O were set to 30 and 0.5 µL/min, respectively (Q_W/Q_O = 0.017).

First, the effects of varying the two parameters on the capacity to generate microdroplets at the FFJ were assessed. As seen in Figure 21.a, all conditions resulted in the stable formation of microdroplets. However, increasing the outlet tubing length, which increases pressure within the system, resulted in slight changes to the fluid dynamics. More

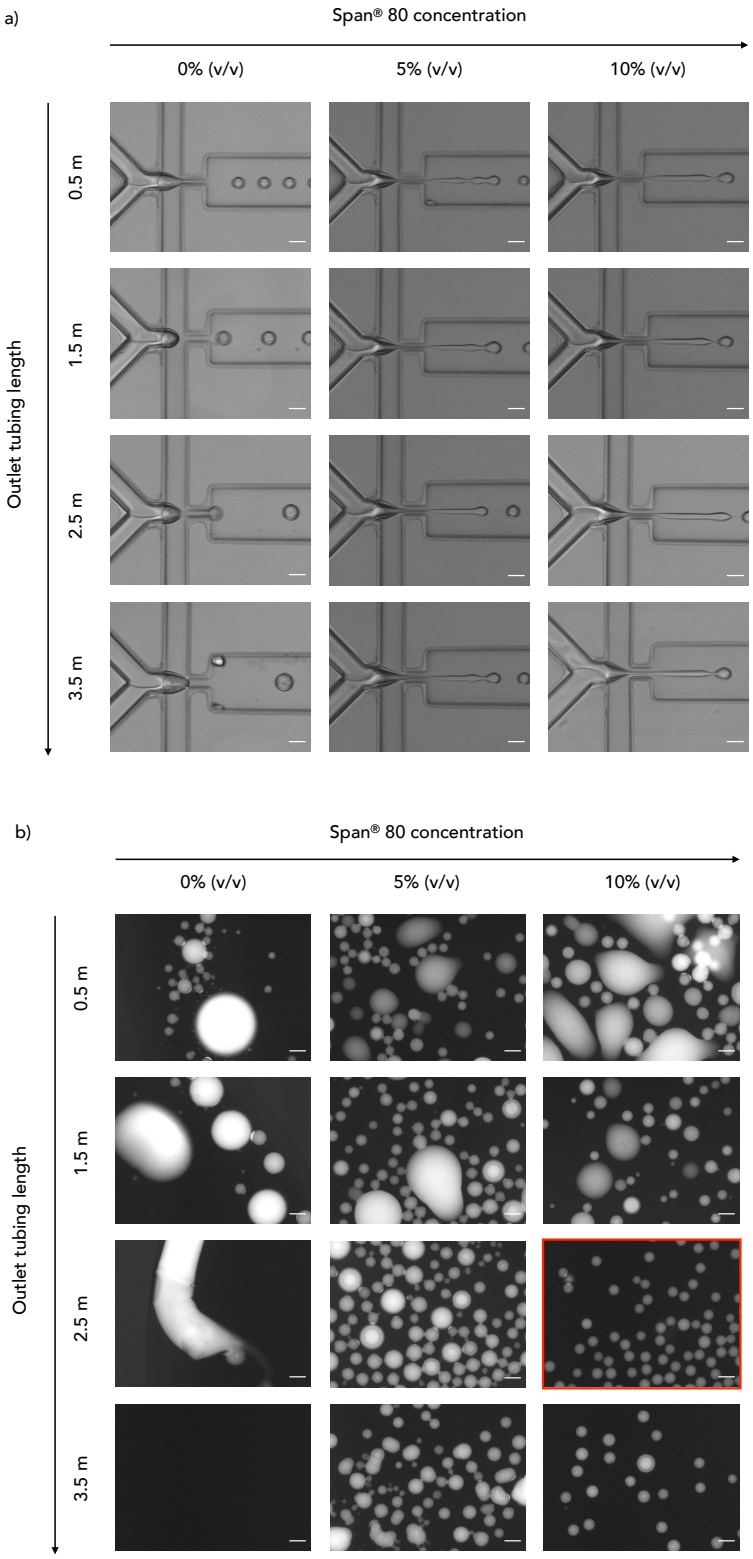


Figure 21: Optimisation of the outlet tubing length and Span® 80 concentration. a) Representative bright field images of the FFJ. Microdroplets were formed in all conditions. Increasing the outlet tubing length or decreasing Span® 80 concentration resulted in a decreased microdroplet generation frequency and an increased microdroplet size. b) Representative bright field images of the material collected at the end of the outlet tubing (in the oil phase, scale bar = 100 μm). Using outlet tubing with a length of 0.5 or 1.5 m did not allow complete crosslinking of the microdroplets. Conditions using longer tubing (2.5 or 3.5 m) but no surfactant resulted in the formation of elongated structures within the outlet tubing that formed through merging of multiple poorly-stabilised microdroplets. Using 10% (v/v) Span® 80 combined with 2.5 m tubing was chosen, as this reproducibly formed monodisperse populations of microgels.

specifically, microdroplet size was increased with the tubing length. This was attributed to the fact that the highest pressure at the FFJ from the outlet side impeded microdroplet formation, which resulted in a low microdroplet generation frequency and thus the formation of larger microdroplets. Decreasing surfactant concentration had similar effects. As seen in Figure 21, the addition of Span® 80 led to the formation of smaller microdroplets with higher frequency, as a result of a decreased interfacial tension.

Second, the effects of the tubing length and Span® 80 concentration on the capacity to form monodisperse microgels was assessed by placing the end of the outlet tubing into a plastic well 10 s to collect the output material. As seen in Figure 21.b), the 0.5 and 1.5 m long tubing produced non-crosslinked microdroplets, as indicated by the presence of non-spherical flattened structures at the bottom of the well. On the other hand, the presence of only spherical particles in all other conditions suggested successful crosslinking. Only the condition using 10% (v/v) Span® 80 combined with 2.5 m tubing reproducibly produced monodisperse microgels and was thus selected for the following experiments. All conditions but the one selected presented very polydisperse size distributions. This is likely due to the microdroplets coalescing within the outlet tubing or in the collection tube. More specifically, polydispersity appeared to increase in conditions where smaller microdroplets were formed, *i.e.* with a shorter outlet tubing or higher concentration of Span® 80. This can be explained by the fact that smaller microdroplets travel faster in laminar flow systems compared to larger microdroplets [229]. As a result, smaller microdroplets spent less time circulating within the outlet tubing, which favoured droplet coalescence in the collection tube, even for formulations using 10% (v/v) Span® 80. Conditions using longer tubing (2.5 or 3.5 m) and no surfactant resulted in the formation of elongated structures within the outlet tubing that would sometimes obstruct the flow. Such structures were formed through merging of multiple microdroplets, which was likely due to the combination of two factors favouring coalescing events before the microdroplets could crosslink. First, the absence of surfactant resulted in poor microdroplet stabilisation. And second, the larger microdroplet size translated into a slower circulation velocity as well as the fact that clogging a channel necessitate coalescence of fewer big microdroplets compared to smaller ones.

3.3.3. Microgel fabrication process reproducibility

Fluorescent microgels were prepared using the optimised set of parameters: 10% (v/v) Span® 80, 2.5 m long outlet tubing, Q_W = 30 µL/min and Q_O = 0.5 µL/min (Q_W/Q_O = 0.017) (Figure 22.a). The reproducibility of the microgel fabrication process was tested using four different chips (Figure 22.b). Microgel diameter was measured by image analysis on 100 microgels per condition (Figure 22.c). Microgel diameter showed little variation between chips, indicating that the microgel fabrication method was reproducible.

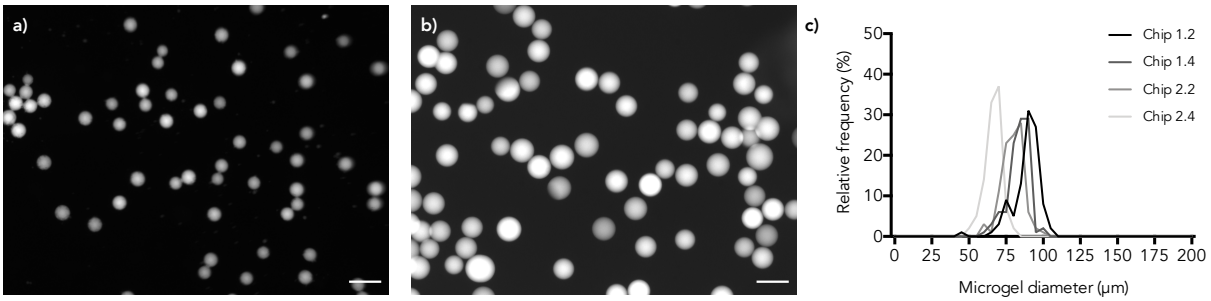


Figure 22: Reproducible microgel fabrication. Representative micrograph of microgels fabricated using the chosen set of parameters (10% (v/v) Span® 80, 2.5 m long outlet tubing, Q_W = 30 µL/min, Q_O = 0.5 µL/min, Q_W/Q_O = 0.017) in a) the oil phase and b) at equilibrium in PBS-antimicrobials (scale bar = 100 µm). c) Reproducibility was validated by fabricating microgels using four different chips. Each chip is numbered as follows: (batch number).(chip number).

3.4. Validation of microgel washing and phase transfer

Microgels in suspension were collected in the oil phase. They were then washed in pentane to remove the mineral oil and Span® 80 and transferred into an aqueous buffer, where they could swell and reach their equilibrium swollen size. Pentane was chosen for multiple reasons. First, it is miscible with both the mineral oil and the Span® 80, meaning that it can be used to dilute and dissolve both components of the oil phase. Second, it has a relatively low density (0.626 g/mL), allowing microgels to rapidly sink, for quick and easy washing without the need for centrifugation. Third, pentane is highly volatile (vapour pressure of 57.90 kPa at 20°C), meaning that once the microgels have been washed, the remaining

traces of pentane can be readily eliminated by leaving the solvent to evaporate under a chemical hood or in a vacuum desiccator. Finally, pentane, which is a Class 3 solvent according to the United States Pharmacopeia (USP), is less toxic compared to other solvents with similar properties, such as hexane [230]. Diluting and removing the surfactant is crucial as it stabilises the microgel suspension in the oil phase. Four washes with a dilution factor of 10 should theoretically result in a final Span® 80 concentration of 0.001% (v/v), which can be considered negligible. As seen in Figure 23.a, an increasing tendency of the microgels to aggregate was observed after each pentane wash. This can be explained by the fact that, as the Span® 80 concentration decreases with the washes, microgels are no longer stabilised in their surrounding hydrophobic environment, which leads them to aggregate through hydrophilic interactions. Microgels were then transferred into an aqueous phase (PBS-antimicrobials) where they could swell and dissociate. They were washed twice in the same buffer to remove any free Alexa Fluor™ 488 C5 Maleimide which had not crosslinked with the thiolated crosslinker (Figure 23.b). The fluorescence intensity at 490/525 nm was measured in the supernatant of the two PBS washes as well as in the final 10% (v/v) microgel suspension (Figure 23.d). As seen in Figure 23.c, the supernatant fluorescence intensity obtained from the second PBS wash was reduced compared to the supernatant obtained from the first one to a level similar to the control. This suggests that the second wash was necessary and that most of the free dye was removed after the second PBS wash.

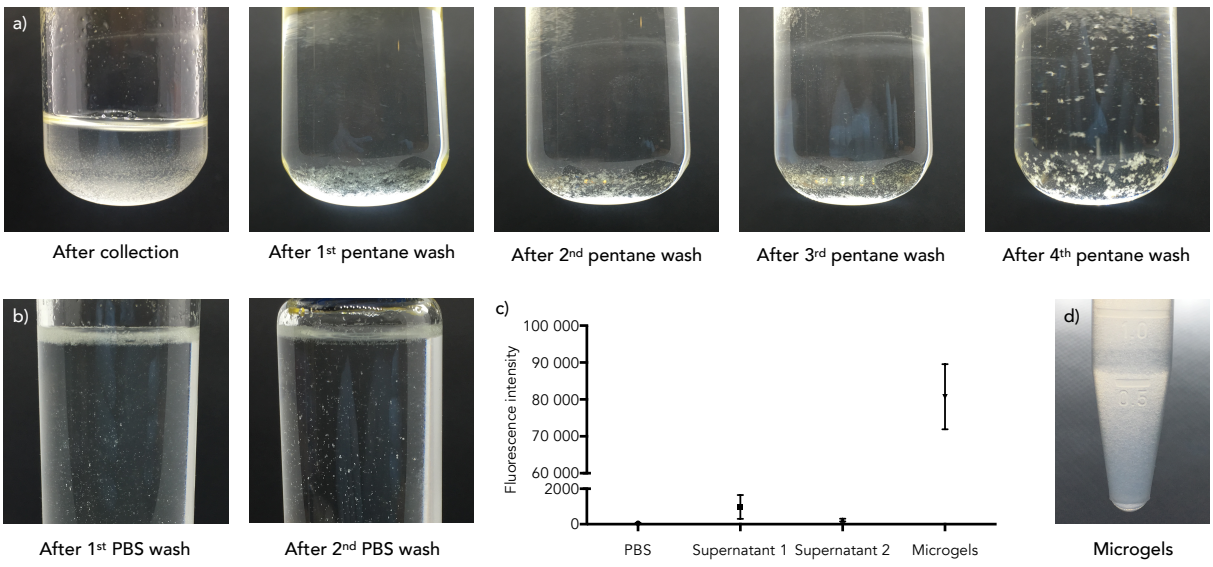


Figure 23: Validation of microgel washing and phase transfer. a) Representative pictures of the microgel suspension after each pentane wash and b) PBS wash. c) Fluorescence intensity measurements performed on the supernatant collected after each PBS wash, on the final 10% (v/v) microgel suspension and on a PBS control. d) Representative picture of the final 10% (v/v) microgel suspension.

3.5. Injectability

The capacity to inject the 10% (v/v) suspension without damaging the microgels was evaluated using two methods. Images of microgels before and after injection through a 29G x 12.7 mm needle (Figure 24). Injection was smooth and feasible by hand. As seen in Figure 24.a, no microscopic damage was observed after injection. Rheological measurements showed a decreased viscosity as the shear rate increased, which is indicative of a shear-thinning material, ideal for injection (Figure 24.b).

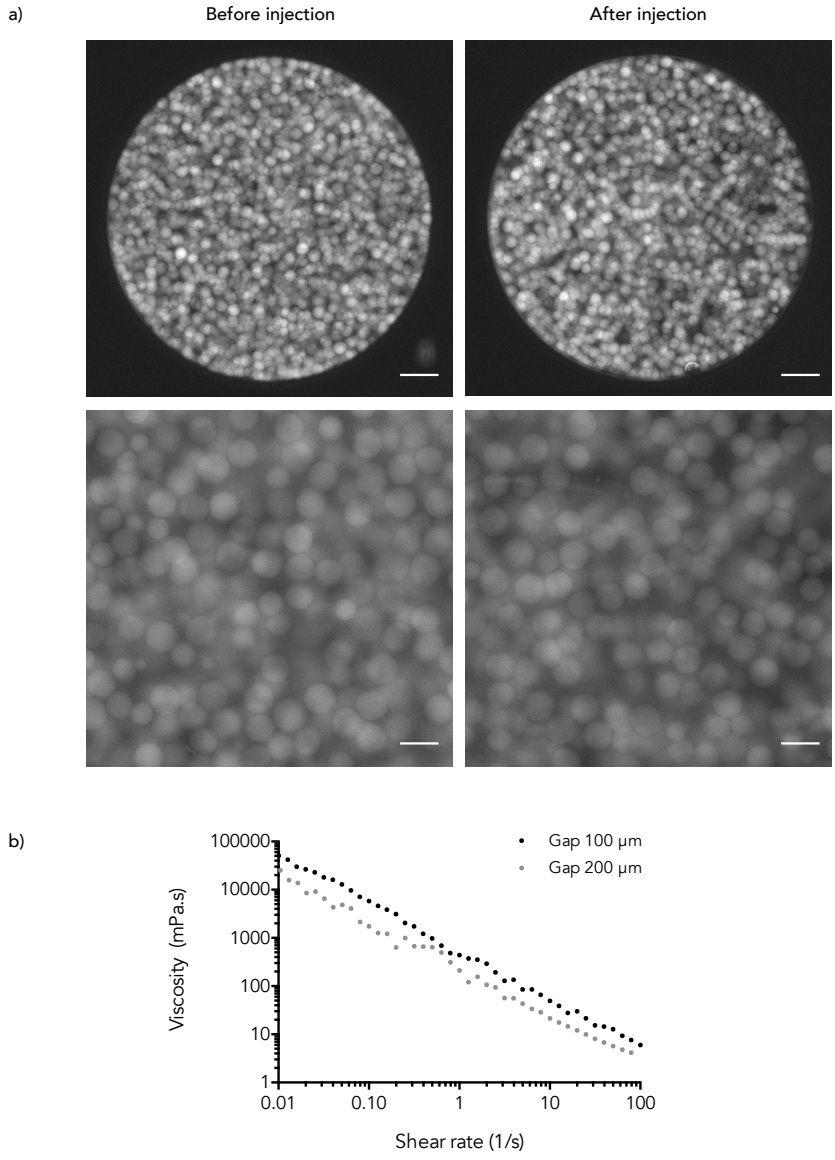


Figure 24: Injectability of the 10% (v/v) microgel suspension. a) Images taken before (left) and after (after) injecting the microgels through a 29G x 12.7 mm needle (scale bar = 250 µm for top images, scale bar = 100 µm for bottom images). No damage was observed after injection. b) Viscosity measurements. Viscosity decreased as shear rate increased, which is indicative of a shear-thinning material, ideal for injection.

4. Conclusions

In this chapter, a microfluidics-based method for the fabrication of injectable PEG-based microgels was described. A microfluidic chip was designed to allow the efficient formation of monodisperse microdroplets in the targeted size range. Microgel size and yield were optimised by varying the relative flow rates, outlet tubing length and Span® 80 concentration. These last two parameters were also tuned to adequately stabilise the microdroplets until fully crosslinked, and thus enable the continuous in-line fabrication of microgels for at least 2 h at a time without interruption. Finally, a microgel washing protocol was developed to remove the oil residue, surfactant, and free fluorescent dye, as well as to provide adequate microgel storage and usage conditions. This protocol allowed the production of injectable microgels with an equilibrium swollen diameter of approximately 75 µm. The final 10% (v/v) microgel suspension presented shear-thinning properties and could easily be injected through a 29G needle, which suggests that the final microgel suspension should be deliverable using the percutaneous catheter-based intramyocardial injection systems described in Chapter 1.

Using the present setup, the yield could be increased up to 1 µL of hydrogel precursor solution processed into microdroplets per min, which corresponds to 1.2 mL of 10% (v/v) microgel suspension produced in 2 h. Higher yields could be achieved by running the system continuously and/or working with multiple droplet generation junctions in parallel [231]. Automated high-throughput production systems, such as the Elveflow® products (Elvesys) could also be used to facilitate the scaling-up process and, more importantly, reach the high levels of quality and standardisation required for the production of clinical-grade medicinal products. Moreover, methods used for the microgel phase transfer and washing steps could be replaced by industrial-scale processes that use large tanks and high-throughput liquid filtration-based methods. Finally, automated microgel size analysis could be performed using specialised equipment such as a Mastersizer 3000 (Malvern Panalytical).

In this study, microgels were produced in a suspension in mineral oil and Span® 80, and washed in pentane before being resuspended in a physiological buffer. Mineral oil and surfactants (including Span® 80) are widely used in the pharmaceutical, cosmetic and food industry. However, administration of high amounts of those components were shown to induce side effects. Tissular accumulation and formation of foreign-body granulomas following systemic administration of mineral oil have been reported [232-234]. Although Span® surfactants are considered practically non-toxic [235], cases of contact dermatitis have been reported [236]. Although minimally toxic when administered by oral, inhalation and topical routes [237], there is currently no data on the effects of intramuscular administration of traces of pentane. A more robust validation of the washing process is required to ascertain trace levels of these components. In addition, evaluation of the final product toxicity *in vitro* and *in vivo* will be required prior to the conduction of any clinical trial. The results of the preliminary cytotoxicity experiments are presented in the Chapter 3. In addition, quantification of the three trace components could be performed using chromatography-based techniques [238, 239].

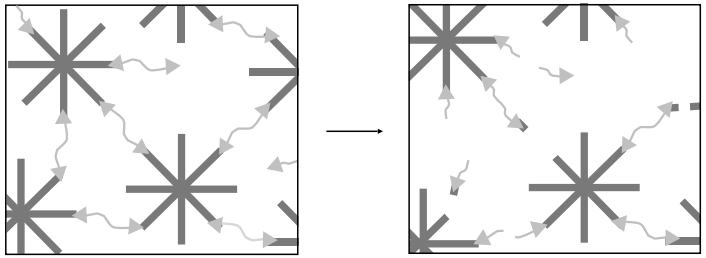
Chapter 3 MMP-sensitive microgels for environmentally-responsive degradation

1. Introduction

Using degradable hydrogels for drug delivery has two main objectives: controllably releasing the therapeutic cargo over time and eliminating the implanted materials from the tissue following delivery. The hydrogels used in this project are formed by a Michael addition between a thiolated crosslinker and an acrylated polymer, which results in the presence of hydrolysable ester bonds in the polymer backbone. While hydrolysis is an effective strategy for sustained microgel degradation, the rate of degradation is relatively slow *in vitro* and *in vivo* [172] and cannot be tuned once the microgels are fabricated. Additional control over degradability can be conferred using photodegradable or enzyme-sensitive crosslinkers [167-170]. In particular, using enzyme-degradable segments provides control over the release rate of the therapeutic cargo without the need for an external trigger. Synthetic peptides based on the structure of natural substrates can be used as enzyme-sensitive segments. Interestingly, MMP-2 and MMP-9 have been shown to be upregulated in the heart for up to a month after an MI [41, 179, 180]. Utilising a peptide crosslinker that can be degraded by these enzymes could provide an environmentally-sensitive response to aid the kinetics of cargo delivery [181].

The fabrication of MMP-2/9-sensitive microgels is described in this chapter. More specifically, an enzyme-sensitive peptide crosslinker was synthesised and characterised (Figure 25). The peptide sensitivity to MMP-2 and MMP-9 was investigated. The composition of two buffers was optimised to ensure the stability of both the hydrogels precursors and the EVs. Emphasis was placed on tailoring the crosslinking kinetics to the microfluidics setup developed in Chapter 2 and providing a suitable platform for EV encapsulation and delivery to the heart, which will be explored in Chapter 4. The synthesised thiol-terminated peptide crosslinker was used to fabricate MMP-2/9-sensitive microgels. The effects of utilising the new peptide crosslinker in place of the commercially-available PEG dithiol crosslinker used so far on microgel size and stability were investigated. The cytotoxicity of both microgel formulations was assessed *in vitro* using relevant primary cardiac cells. Finally, the sensitivity of the fabricated microgels to MMP-9 was evaluated to determine whether the formulation was suitable for sustained EV delivery for heart repair.

a)



b)

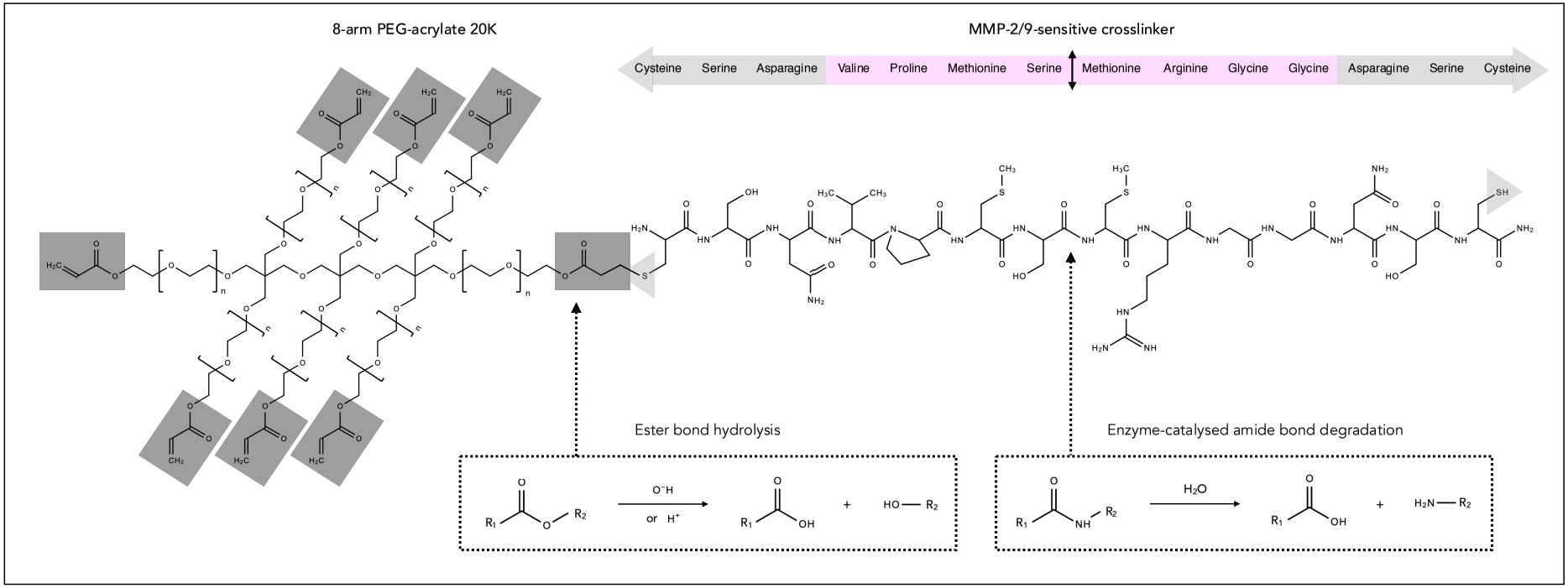


Figure 25: MMP-2/9-mediated degradation. a) Overview of the hydrogel degradation mechanism. b) Hydrogel degradation is achieved through 2 types of reaction. The ester bonds can be hydrolysed in acidic or basic conditions (left) and the peptide crosslinker can be recognised and cleaved by MMP-2 and MMP-9 (right). The recognition motif is indicated in lighter pink and the black arrow represents the cleavage site. The ends of the sequence (light grey) contribute to the peptide stability and reactivity.

2. Materials and methods

2.1. Materials

Acetonitrile (ACN) (A/0620/PB17), Alexa Fluor™ 488 C5 Maleimide (A10254, MW 720.66), antibiotic-antimycotic (A/A) 100X (15-240-062), Brij™-35 (20150), BSA (A2153), $CaCl_2$ (C1016), calcein-AM (C1430), DAPI (D1306), DPBS without calcium and magnesium 1X (14-190-144), DMEM high glucose GlutaMAX™ supplemented with pyruvate (10569010), DTNB (22582), ethidium homodimer-1 (E1169), glycerol (G5516), penicillin-streptomycin (P/S) 10,000 U/mL (15-140-148), tricine (T0377), trypsin-EDTA 0.05% (25300054), trypsin-EDTA 0.5% (15400054) and $ZnCl_2$ (229997) were purchased from Fisher Scientific. EDTA (EDS), HCl solution 1.0 N (H9892), HEPES solution 1 M (H0887), L-cysteine hydrochloride (C1276), mineral oil (M5310), human recombinant MMP-2 (SRP3118), human recombinant MMP-9 (PF140), MOPS (M1254), NaCl solution 5 M (S5150), NaOH solution 1.0 N (S2770), Na_2HPO_4 (S7907), PEG dithiol crosslinker (717142, average Mn 1000), 20% (v/v) piperidine in DMF (80645), saponin (47036), sodium acetate buffer solution 3M (S7899), Span® 80 (S6760), trifluoroacetic acid (TFA) (T6508) and triisopropyl silane (TIS) (233781) were purchased from Sigma-Aldrich. Rink Amide-AM resin (100-200 µm mesh, 0.33 mmol/g), Fmoc-protected amino acids, dimethylformimide (DMF), *N,N,N',N'*-Tetramethyl-O-(1H-benzotriazol-1-yl)uronium hexafluorophosphate *o*-(Benzotriazol-1-yl)-*N,N,N',N'*-tetramethyluronium hexafluorophosphate (HBTU) and dithiothreitol (DTT) were purchased from ATGC Bioproducts. Dichloromethane (DCM) (24233) and diethyl ether (32203) were purchased from Honeywell. Ninhydrin test (kaiser test) kit (25241) was purchased from Anaspec. Diisopropylethylamine (DIEA) (005027) was purchased from Fluorochem. 8-arm PEG-acrylate (tripentaerythritol) (MW 20740) was purchased from JenKem Technology USA.

2.2. Methods

2.2.1. Peptide crosslinker: synthesis, purification and characterisation

An MMP-2/9-sensitive peptide crosslinker (CSNVPMSMRGGNSC) was synthesised by solid phase peptide synthesis (SPPS) using a Rink Amide-AM resin. First, the resin was deprotected using 20% (v/v) piperidine in DMF and deprotection was confirmed with a positive Kaiser test (presence of free amines). Fmoc-protected amino acids were sequentially coupled using a 4x molar excess Fmoc-amino acid, 3.95x molar excess HBTU and 6x molar excess DIEA in DMF. Each amino acid was reacted for at least 3 hours on a peptide vessel shaker. Reaction completion was confirmed by a negative Kaiser test (absence of free amines).

Peptides were cleaved from the resin using TFA, TIS, water (95/2.5/2.5 v/v) with 2.5% (w/v) DTT, precipitated three times in chilled diethyl ether and purified by reversed-phase high-performance liquid chromatography (HPLC) (Shimadzu prominence system equipped with UV detector at 220 and 280 nm and a Phenomenex C18 Gemini NX column, 5 µm pore size, 110 Å particle size, 150 x 21.2 mm) under acidic conditions using a acetonitrile/water gradient at a flow rate of 12 mL/min. Fractions 11 to 15 min were pooled and freeze-fried.

Peptide molecular weight was confirmed by liquid chromatography-mass spectrometry (LC-MS) (Agilent 6130 Quadrupole coupled to an Agilent 1260 Infinity LC equipped with a 150 x 4.6 mm Phenomenex C18 Gemini NX column, 5 µm pore size and 100 Å particle size, Agilent Technologies) and matrix-assisted laser desorption/ionization time-of-flight mass spectrometry (MALDI-TOF MS) (Micromass® MALDI micro MX™, Waters).

For the study of MMP-2/9-triggered degradation, an enzyme buffer containing 50 mM tricine, 10 mM $CaCl_2$, 50 mM NaCl, 20 µM $ZnCl_2$ and 0.05 wt% Brij™-35, 20% (v/v) glycerol and 0.1% wt% BSA was prepared. MMP-2 and MMP-9 were dissolved in enzyme buffer at a concentration of 1 µM and 0.5 µM respectively and stored at -80°C until further use. Aliquots of 0.5 mg degradable crosslinker were placed into glass tubes and dissolved in 100 µL of either enzyme buffer, 40 nM MMP-2 or 20 nM MMP-9. Tubes were then placed at 37°C overnight. This was followed by a disulfide bond reduction step using 50 mM DTT in 20 mM MOPS pH 8 at 37°C for 1 hour. Finally, the content of each tube was analysed by LC-MS (Agilent 6130 Quadrupole coupled to an Agilent 1260 Infinity LC equipped with a

150 x 4.6 mm Phenomenex C18 Gemini NX column, 5 µm pore size and 100 Å particle size, Agilent Technologies).

2.2.2. Optimisation of the hydrogel precursor buffer composition

The composition of two new buffers was tailored to ensure EV and precursor stability. The concentrations of the salts were adjusted in both buffers to ensure adequate osmolarity before and after mixing of the two precursors solutions. The composition of the HEPES buffer was optimised using various concentrations of HEPES, NaCl and Na_2HPO_4. A sodium acetate-based buffer was prepared using various concentrations of CH_3COONa, CH_3COOH and NaCl. The pH was measured in each buffer and in a solution prepared by mixing the two buffers with a ratio 1:1.

The ability of the two buffers to stabilise the two hydrogel precursors was assessed by measuring the thiol concentration in the crosslinker solution and analysing the crosslinking kinetics of the hydrogel formulations (crosslinking time and rheology) every hour for 4 hours after hydrogel precursor preparation.

Thiol concentration in the crosslinker solution was measured using the Ellman's Reagent assay. Briefly, a pH 8 reaction buffer was prepared with 0.1 M Na_2HPO_4 and 1.0 mM EDTA, and the pH was adjusted using 1 M NaOH. An Ellman's reagent solution was prepared with 4 mg/mL DTNB in the pH 8 reaction buffer. An L-cysteine standard curve was prepared from a 15 mM L-cysteine hydrochloride stock solution. This was followed by the preparation of 1 mM non-degradable and degradable crosslinker solutions using the sodium acetate buffer, of which the composition was optimised in section 3.1.1. At each time point (0, 1, 2, 3, 4 h after precursor dissolution), 25 µL of either crosslinker solution were transferred into a tube, diluted into 250 µL pH 8 reaction buffer and 5 µL Ellman's reagent solution, and left to react at RT for 15 min. Three 60 µL replicates were then pipetted into a 384-well plate and absorbance was measured at 412 nm with an EnVision® plate reader (PerkinElmer). Free thiol concentration was then calculated using the standard curve. In this assay, the DTNB

substrate is reduced by the free thiols present in the crosslinker solution, resulting in a yellow colour change.

Crosslinking time was measured manually in an Eppendorf tube. First, the PEG polymer and crosslinker solutions were prepared using their respective buffer. At each timepoint (0, 1, 2, 3, 4 h after precursor dissolution), the two hydrogel precursor solutions were mixed with a ratio 1:1 and crosslinking time was determined by continuously pipetting the solution up and down. The crosslinking time was defined as the time elapsed between the time the hydrogel precursors are first mixed and the moment the solution can not longer be pipetted.

Finally, crosslinker solution stability was assessed by rheometry. The elastic (G') and viscous (G'') contributions to shear modulus of the non-degradable and degradable hydrogels were measured using a AR2000ex rheometer (TA instruments) and a 8 mm sst plate. The gap was set to 500 µm and temperature to 25°C. At each time point (0, 1, 2, 3, 4 h after precursor dissolution), the hydrogel precursor solutions were mixed with a ratio 1:1 and 40 µL of the solution was placed onto the plate. G' and G'' were measured for 10 min using a normal force of approximately 0.35 N, a 1% strain and a 1 Hz frequency.

2.2.3. Hydrogel characterisation: swelling ratio, crosslinking density and mesh size

The set of buffers n°4 (selected in section 3.1.3.) was used to prepare hydrogels. Briefly, a HEPES buffer was prepared with 150 mM HEPES and 75 mM NaCl in MilliQ water and the pH was adjusted to 7.4 using NaOH and HCl solutions. A sodium acetate buffer was prepared with 10 mM sodium acetate and 140 mM NaCl and the pH was adjusted to 5.0 using NaOH and HCl solutions. Hydrogel precursor solutions were prepared by dissolving the PEG polymer in the HEPES buffer, and the non-degradable PEG dithiol crosslinker or degradable peptide crosslinker in the sodium acetate buffer. Hydrogel patches with a 10 wt% and a 1:1 thiol:acrylate crosslinking molar ratio were prepared using micromoulds (8 mm diameter, 800 µm height, approximately 40 µL, n = 3 per hydrogel formulation). After a

20 min incubation at RT for 20 min, the patches were left to swell in PBS 1% (v/v) A/A 1% (v/v) P/S overnight. Rheological measurements were performed on a AR2000ex rheometer. A strain sweep (0.1% - 5% strain using a 1 Hz frequency) and a frequency sweep (0.1-10 Hz frequency using a 1% strain) were performed on each patch, from which the average elastic modulus (G') and viscous modulus (G'') of each hydrogel formulation was calculated. Time sweeps were then performed at 1% strain and 1 Hz frequency. The swollen wet mass (m_w) and dry mass after freeze-drying (m_d) of each patch were measured. Finally, the swelling ratio (Q), crosslink density (ρ_x) and mesh size (ξ_x) were calculated using the following equations (1-4) and constants (Table 9):

Swelling ratio: $$Q = 1 + \frac{\rho_p}{\rho_s}\left(\frac{m_w}{m_d} - 1\right) \quad (1)$$

Crosslink density: $$\rho_x = \frac{G' Q^{1/3}}{RT} \quad (2)$$

Mesh size: $$\xi_x = Q^{1/3} C_n^{1/2} l n^{1/2} \quad (3) \quad \text{with} \quad n = \frac{3\rho_p}{44\rho_x} \quad (4)$$

Table 9: Table of constants used to calculate the swelling ratio, crosslinking density and mesh size.

Parameter	Symbol	Value	Unit
Swelling ratio	Q	-	-
Crosslinking density	ρ_x	-	mM
Mesh size	ξ_x	-	nm
Polymer density	ρ_p	1.07	g/mL
Solvent density	ρ_s	1.00	g/mL
Wet mass	m_w	-	g
Dry mass	m_d	-	g
Shear modulus	G'	-	Pa
Gas constant	R	8.314	J/(mol.K)
Temperature	T	298	K
Polymer characteristic ratio	C_n	4	-
Average bond length for PEG	l	1.47	Å
Number of bonds between crosslinks	n	-	-

2.2.4. Microgel preparation, size analysis and storage

Non-degradable and degradable microgels were prepared using methods optimised in Chapter 2. Briefly, an oil phase was prepared by adding 10% (v/v) Span® 80 with mineral oil. Set of buffers n°4 (described in 2.2.3) was used to prepare the hydrogel precursor solutions. The hydrogel composition was set to 10 wt% polymer with a thiol:acrylate crosslinking molar ratio of 1:1. The PEG-acrylate solution was prepared by dissolving the 8-arm PEG-acrylate 20K in HEPES buffer. The crosslinker solution was prepared by dissolving either the non-degradable PEG dithiol crosslinker or the degradable peptide crosslinker synthesised in section 2.2.1 in sodium acetate buffer, and adding 10 nM Alexa Fluor™ 488 C5 maleimide to provide the microgels with a fluorescent label.

Microgels were prepared using the microfluidic setup developed in Chapter 2 with a type-2 chip and a 2.5 m-long outlet tubing. The system was initialised using the sequence of steps described in Chapter 2, section 2.2.5. The oil phase and aqueous phase flow rates were set to 30 µL/min and 0.5 µL/min respectively. Microgels were collected for 2 hours and washed using the protocol described in 2.2.6. and stored at 4°C, RT or 37°C for up to 90 days. Microgel diameter was analysed by image analysis (Fiji) of images taken on an inverted microscope (Olympus) and used to evaluate microgel stability.

2.2.5. Microgel cytotoxicity

Cardiac fibroblasts were isolated from neonatal rats by Dr. Ivan Diakonov (Imperial College London) using a neonatal heart dissociation kit (130-098-373, Miltenyi Biotec). Briefly, neonatal rat hearts were isolated and enzymatically digested using the kit components and a gentleMACS™ Dissociator to help cell dissociation. The cell suspension was then filtered to remove any remaining larger particles and cultivated in DMEM high glucose GlutaMAX™ supplemented with pyruvate, 1% (v/v) P/S and 10% (v/v) FBS at 37°C under 5% CO_2 until passage 4.

For cytotoxicity experiments, cells were seeded at 50,000 cells/cm^2 with 300 µL media per well of an ibiTreat 8-well plate. A total of six conditions were tested: live cells (control), dead cells (control) and cells treated with 5 µL - 25 µL of 10% (v/v) non-degradable or degradable microgel suspension. Four wells were seeded for each condition: three wells for flow cytometry analysis and one well for microscopy. On the day after seeding, cells were rinsed with warm PBS to remove floating dead cells. Microgels were then added to corresponding wells and cells were incubated with the microgels for 72 hours at 37°C under 5% CO_2.

For wells dedicated to microscopy, brightfield images were taken at each stage of the experiment using an inverted microscope (Olympus, 10X objective lens). At the end of the incubation period, cells were rinsed three times with warm PBS to remove all microgels. Control dead cells wells were treated with saponin 0.1% (w/v) for 15 min at 37°C and rinsed with warm PBS. Finally, cell viability was assessed using live/dead staining. Briefly, a solution containing 2 µM calcein-AM and 4 µM ethidium homodimer-1 in PBS was prepared and added to each wells. Cells were incubated for 30 min at RT in the dark, washed with warm PBS and imaged using inverted microscope (Olympus, 10X objective lens). For the three wells dedicated to flow cytometry analysis, cells were detached using 0.05% trypsin-EDTA for 5 min at RT. DAPI was added to each tube and the cell population was analysed by flow cytometry (BD Fortessa). The cell population was gated on single cells and viable cells were defined as DAPI-negative single cells.

2.2.6. Trypsin and MMP-9-mediated microgel degradation

Microgel degradability was evaluated using trypsin and MMP-9. Alexa Fluor™ 488 C5 Maleimide-labelled microgels were prepared using methods described in section 2.2.4. All experiments were performed in 384-well plates to minimise the volumes required.

For the microgel degradation experiment using a single high concentration of trypsin, 20 µL of 10% (v/v) non-degradable or degradable microgel suspension was placed in a 384-well containing 25 µL HEPES buffer and 5 µL 0.5% trypsin-EDTA. Bright field images were taken every 2 min for 10 min using an inverted microscope (Olympus, 4X objective lens).

For the microgel degradation experiment using a range of trypsin concentrations (0, 0.2, 1 or 5 nM), an enzyme buffer (EB) was prepared with 50 mM tricine, 10 mM $CaCl_2$, 50 mM NaCl, 20 µM $ZnCl_2$ and 0.05 wt% Brij™-35, and the pH was adjusted to 7.5. Before starting the experiment, 1% (v/v) A/A and 1% (v/v) P/S were added to the enzyme buffer (EB-antimicrobials) and the final solution was 0.2 µm sterile-filtered. All 384-wells were coated with a 2 wt% BSA solution for 2 hours at 4°C, washed three times with PB 1% (v/v) P/S 1% (v/v) A/A and dried with N_2 before use. An Alexa Fluor™ 488 standard curve was prepared in a separate 384-well plate. A volume of 48.8 µL EB-antimicrobials was added to each well. Then, 6.25 µL of either EB-antimicrobials, 10% (v/v) non-degradable microgel suspension or 10% (v/v) degradable microgel suspension was added to corresponding wells (n = 3 per condition). Bright field images of each well were then taken using an inverted microscope (Olympus, 4X objective lens). Trypsin stock solutions were prepared using 0.5% trypsin-EDTA, EB-antimicrobials and 22.5 µL of the appropriate solution was added to each well. Between each timepoints, the plates were incubated at 37°C under 5% CO_2. At each timepoint (day 1, 2, 3, 4), images of each well were taken using an inverted microscope (Olympus, 4X objective lens). This was followed by the transfer of 22.5 µL supernatant of each well into a free well of the standard curve black 384-well plate and fluorescence measurement at 490/525 nm on an EnVision® plate reader (PerkinElmer). On day 1 to 3, the same volume of fresh trypsin solution was then added to corresponding wells and plates were incubated at 37°C until the next timepoint. On day 4, 22.5 µL of 0.5% trypsin-EDTA was added to each well and plates were incubated at 37°C for 2 h to allow complete microgel degradation. The absence of microgels was checked using an inverted microscope (Olympus, 4X objective lens) and a volume of 22.5 µL supernatant of each well was then transferred into a free well of the standard curve black 384-well plate. Fluorescence was measured at 490/525 nm on an EnVision® plate reader (PerkinElmer) and values were used to normalise the relative released dye concentration of each timepoint.

The same protocol was used for the microgel degradation experiment using 40 nM MMP-9. However the enzyme was tested at a single concentration on degradable microgels only (n = 3 per condition).

2.2.7. Statistical analysis

Data are presented as median ± interquartile range unless stated otherwise. Swelling ratio, crosslinking density and mesh size were analysed by two-tailed Mann-Whitney test. Microgel size was analysed by a Kruskal-Wallis test with Dunn's correction and all groups were compared to "day 2". In the cytotoxicity assay, DAPI-negative cell quantification was analysed by Kruskal-Wallis with Dunn's correction and all groups were compared to "live cells".

3. Results and discussion

3.1. MMP-2/9 degradable crosslinker synthesis and characterisation

3.1.1. Degradable peptide crosslinker synthesis and characterisation

A cysteine-terminated MMP-sensitive peptide crosslinker (CSNVPMS↓MRGGNSC) was synthesised by SPPS and purified by HPLC [176]. The LC-MS and MALDI-TOF MS spectra of the peptide after purification are shown in Figure 26. The MS analysis of fractions 0-8 min revealed the presence of m/z peaks at 721 (100%) and 1442 (37%) corresponding to the expected [M/2 + H] and [M + H] of the synthesised peptide (MW 1442). In addition, the absence of any other major peak on the spectra indicated that the synthesised peptide was of high purity.

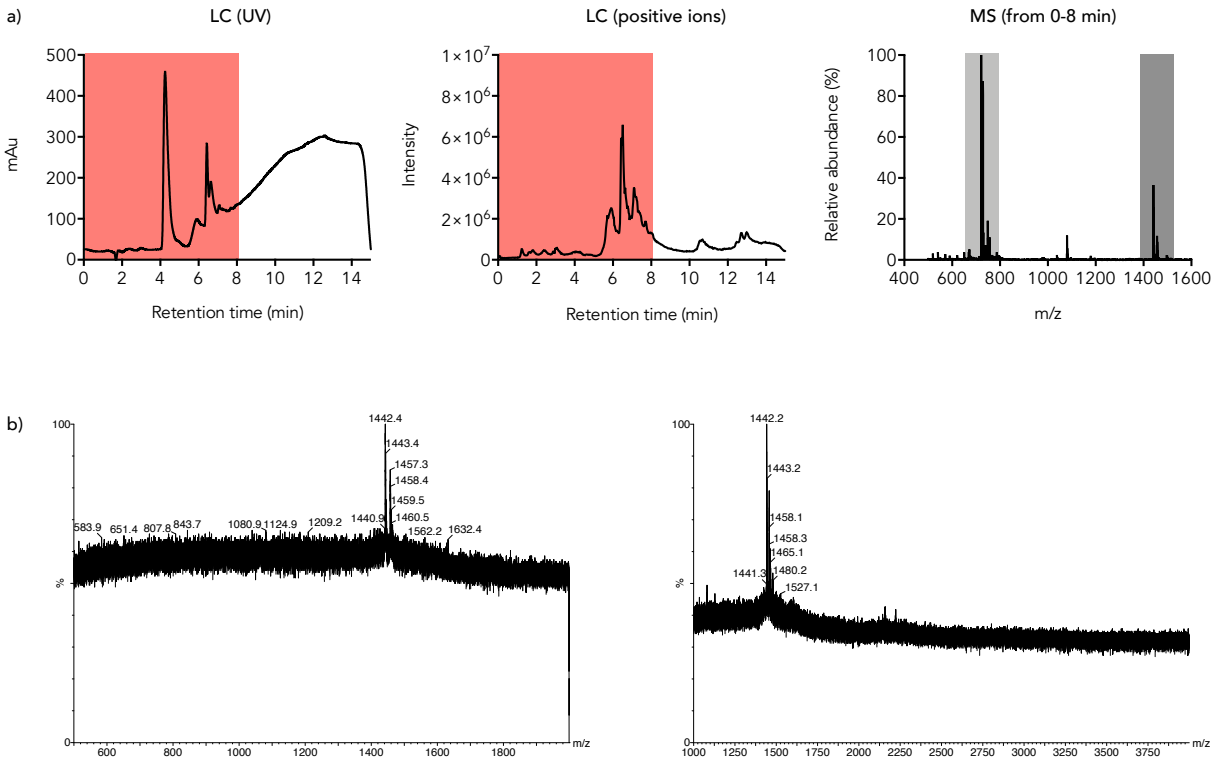


Figure 26: Peptide degradable crosslinker characterisation using a) LC-MS and b) MALDI-TOF MS. The MS analysis of fractions 0-8 min (red) revealed the presence of m/z peaks at 721 (100%, light grey) and 1442 (37%, dark grey) corresponding to the expected [M/2 + H] and [M + H] of the synthesised peptide (MW 1442). In addition, the absence of any other major peak on the spectra indicated that the synthesised peptide was of high purity.

3.1.2. Peptide crosslinker degradation by MMP-2/9

Although *in vitro* degradation studies using synthetic MMPs cannot accurately replicate the physiopathological conditions found in native tissues, such studies can provide general trends regarding peptide sensitivity to specific enzymes. The following study looked at the ability to degrade the synthesised peptide crosslinker using physiologically relevant concentrations of synthetic MMP-2 and -9 [240] through LC-MS analysis of the cleavage products.

Similar MS spectra were obtained from the fractions 0-8 min of the peptide dissolved in MilliQ water (Figure 26.a) or the enzyme buffer (Figure 27, top). This indicated the absence of spontaneous peptide degradation within the timeframe of the experiment (12 h). Of note, the presence of two new peaks in the positive ion spectrum (10-14 min) of the sample dissolved in the enzyme buffer was attributed to the nonionic surfactant (Brij™-35) used to prepare this buffer, and MS analysis was thus limited to fractions 0-8 min.

Partial degradation was achieved using either MMPs, as suggested by the reduction in relative abundance of [M/2 + H] compared the original peptide spectra as well as the disappearance of the [M + H] peak (Figure 27). More specifically, the [M/2 + H] peak was reduced from 100% relative abundance to 18% and 8%, when the peptide was treated with 40 nM MMP-2 and 20 nM MMP-9 respectively. In addition, the appearance of multiple new peaks in the m/z range of 600-650, including peaks that corresponded to the expected fragments CSNVPMS and MRGGNSC masses (MW 737 and 724, respectively), indicated successful cleavage of the peptide into smaller peptides. Although the specificity of the cleavage reaction was not investigated by incubating the peptide with other types of MMPs, these results suggested that the peptide was indeed sensitive to MMP-2 and -9, and could be effectively used to formulate environmentally-sensitive drug delivery systems for heart repair.

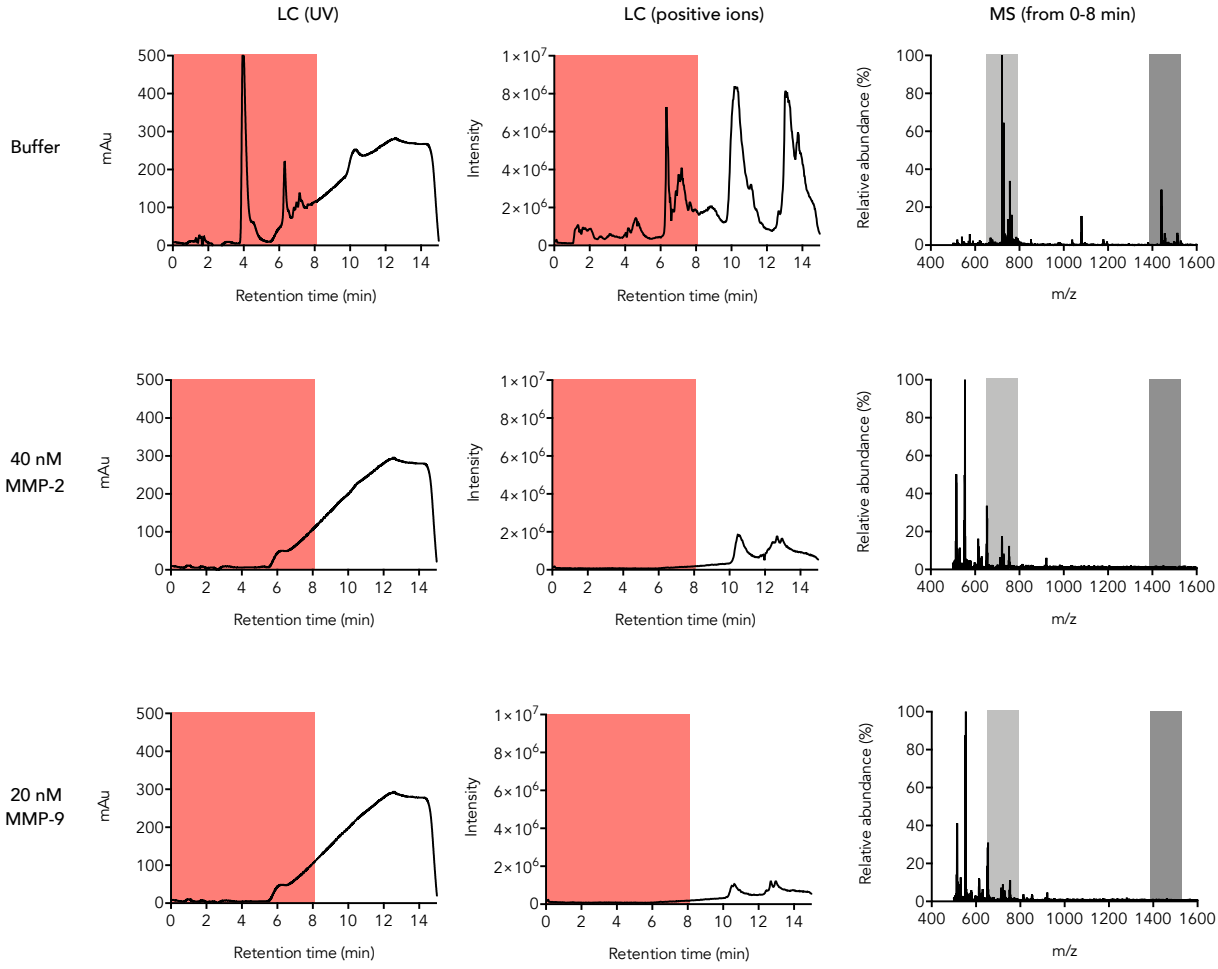


Figure 27: LC-MS spectra of the cleavage products formed by treating the peptide crosslinker with MMP-2 and -9. The MS analysis of fractions 0-8 min (red) revealed that partial degradation was achieved using either MMPs, as suggested by the reduction in relative abundance of [M/2 + H] (light grey), from 100% relative abundance to 18% and 8%, when the peptide was treated with 40 nM MMP-2 and 20 nM MMP-9 respectively, as well as the disappearance of the [M + H] peak (dark grey). Multiple new peaks in the m/z range of 600-650, including peaks that corresponded to the expected fragments CSNVPMS and MRGGNSC masses (MW 737 and 724, respectively), indicated successful cleavage of the peptide into smaller peptides.

3.1.3. Buffer optimisation and validation

The initial buffer used for dissolving both hydrogel precursors was composed of 50 mM HEPES, 140 mM NaCl, 1.5 mM Na_2HPO_4. This buffer had originally been formulated to ensure EV stability by maintaining the pH and osmolarity at close to physiological values, *i.e.* pH 7-7.8 and 275-295 mOsm respectively. However, as shown in Table 10, using this buffer resulted in poor hydrogel precursor stability and decreased reactivity. This was indicated by the increase in the crosslinking time observed when the hydrogel precursors

were left for increasing periods of time in the buffer solution. Precursor stability is essential for microgel fabrication since both hydrogel precursor solutions are prepared and loaded into the syringes of the microfluidics system at the very beginning of the microgel fabrication process and used over a few hours.

Table 10: Decreased hydrogel precursors reactivity over time using the initial buffer (50 mM HEPES, 140 mM NaCl, 1.5 mM Na_2HPO_4, pH 7.5).

Time after hydrogel precursors preparation	Crosslinking time (degradable crosslinker)
0 h 0 min	2 min 10 s
1 h 00 min	2 min 15 s
2 h 13 min	3 min 47 s
2 h 57 min	> 10 min

The composition of two new buffers was tailored to ensure EV and precursor stability (Table 11). The concentration of the different salts were adjusted in both buffers to ensure adequate osmolarity before and after mixing of the two precursors solutions. An HEPES-based buffer with a physiological pH was chosen for the PEG polymer solution containing the EVs, while an acidic sodium acetate-based buffer, which would limit disulphide bond formation, was selected for the crosslinker solution. The pH of the solution resulting from the mixing equal volumes of the two hydrogel precursors solution was measured to ensure that EVs were kept in a physiological environment at all times. Finally, the buffers were used to dissolve the hydrogel precursors and the crosslinking time was measured to determine whether the formulation could gel within 2 to 10 min in order to be compatible with the microfluidics system developed in Chapter 2.

First, the concentration of each buffer was varied to obtain a final pH in the physiological range (set n°1 and 2). Then, the pH of the HEPES buffer was adjusted to tune the pH and thus the crosslinking time of the final solution (set n°3 to 5). As seen in Table 11, the composition of set n°4 allowed for the crosslinking of the PEG-acrylate, and the non-degradable or degradable crosslinker in 5 min 10 s and 2 min 04 s, respectively.

Table 11: Buffer optimisation.

	HEPES buffer				Sodium acetate buffer				1:1	Crosslinking time	
N°	[HEPES] (mM)	[NaCl] (mM)	[Na_2HPO_4] (mM)	pH	[CH_3COONa] (mM)	[CH_3COOH] (mM)	[NaCl] (mM)	pH	pH	Non-degradable crosslinker	Degradable crosslinker
1	100	50	1.5	7.2	100	100	50	5.0	6.2	> 10 min	> 10 min
2	100	50	1.5	7.0	10	10	140	5.0	6.9	> 10 min	6 min 41 s
3	150	75	0	7.1	10	10	140	5.0	7.0	> 10 min	3 min 42 s
4	150	75	0	7.4	10	10	140	5.0	7.4	5 min 10 s	2 min 04 s
5	150	75	0	7.8	10	10	140	5.0	7.7	2 min 30 s	1 min 15 s

The capacity of the new buffers (set n°4) to keep the hydrogel precursors stable at RT for multiple hours was then investigated. Both precursors were dissolved in their respective buffer and stored at RT. At each timepoint (0, 1, 2, 3, 4 h after precursor dissolution), the thiol concentration in the crosslinker solution (Figure 28.a), the crosslinking time (Figure 28.b) and the elastic modulus G' in function of time (Figure 28.c) were measured and compared to their initial value at t_0. There was no appreciable difference between t_0 and t_4, which suggests that both precursors were equally reactive at the beginning and the end of the experiment, meaning that they were stable in the new buffers for at least 4 h.

3.1.4. Hydrogel characterisation

The properties of hydrogels prepared using either the synthesised degradable peptide crosslinker or the commercially-available non-degradable PEG dithiol crosslinker were then compared. With an elastic modulus G' of the order of 10 kPa, both non-degradable and degradable hydrogel formulations demonstrated biomechanical properties similar to muscle tissue, which is ideal for *in vivo* intramuscular delivery [241] (Figure 28.c). Swelling ratio, crosslinking density and mesh size were calculated based on dry weight, wet weight and G' measurements. As shown in Figure 29, although there was a trend towards the degradable hydrogels to swell more and have bigger pores than non-degradable hydrogels, swelling ratio, crosslinking density and mesh size were not significantly different between the two formulations. Moreover, the estimated mesh size was found to be in a

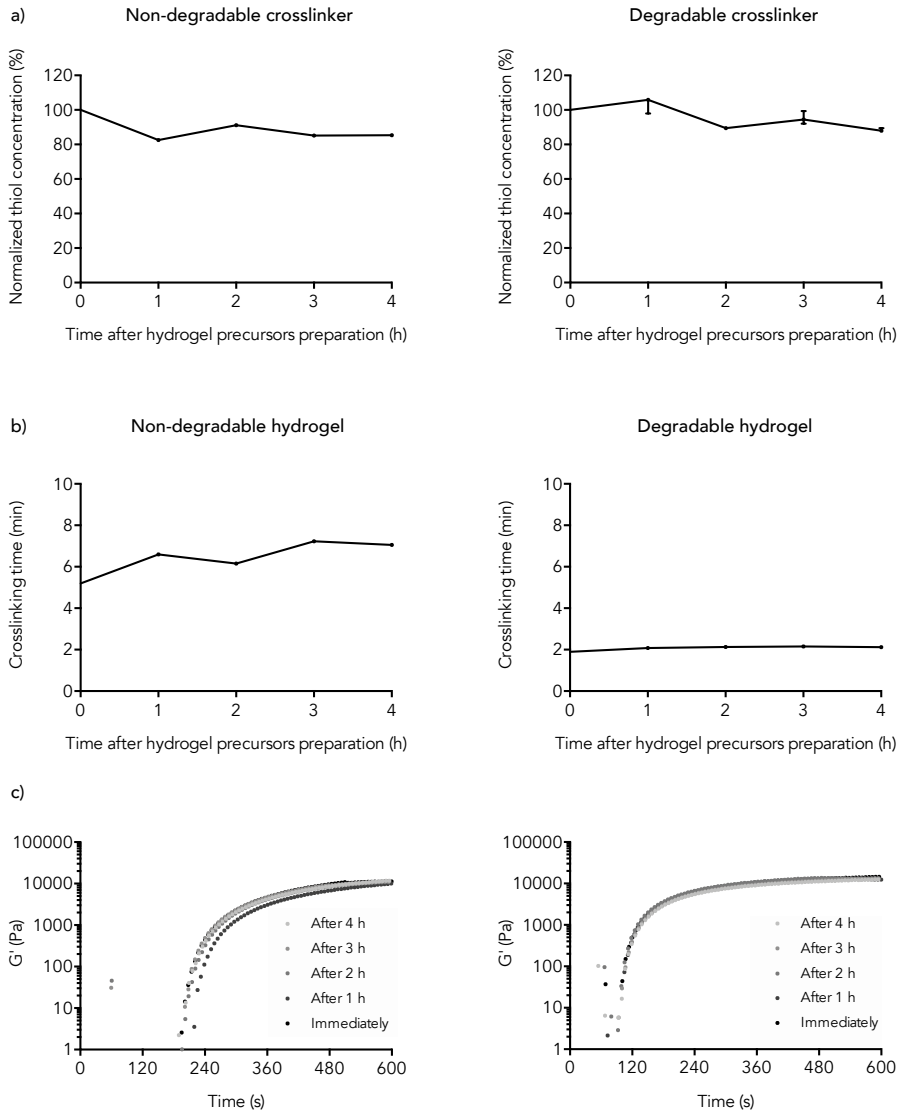


Figure 28: Validation of the new set of buffers using the non-degradable (left) and degradable (right) crosslinkers. a) Thiol concentration measured every hour on crosslinker solutions stored at RT. b) Crosslinking time measured every hour using crosslinker solutions stored at RT. c) Time sweep performed on crosslinking hydrogels using crosslinker solutions stored at RT. Steady thiol concentration, crosslinking time and crosslinking kinetics indicate that both crosslinkers were stable in the new buffers.

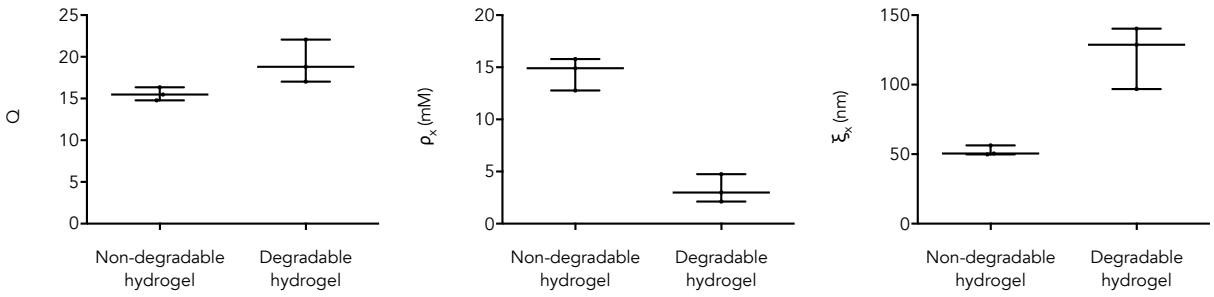


Figure 29: Estimations of swelling ratio Q (left), crosslinking density (middle) and mesh size (right) of the non-degradable and degradable hydrogel formulations (n = 3). All three parameters were found to not be significantly different between the two groups (two-tailed Mann-Whitney test).

range compatible with an efficient entrapment of nano-sized particles such as EVs, with 128 nm and 50 nm for degradable and non degradable hydrogels, respectively.

3.2. Microgel characterisation

3.2.1. Microgel size and stability

The two crosslinkers were then used to prepare non-degradable and degradable microgel 10% (v/v) suspensions. Microgel fabrication was successful using either crosslinker and resulted in the generation of monodisperse microgels with a diameter in the targeted range, with a median size of 76 µm for non-degradable microgels and 86 µm for degradable microgels (Figure 30, day 2). The stability of these microgels in PBS 1% (v/v) A/A 1% P/S (v/v) at various storage temperatures was then assessed by measuring their size over time. As shown in Figure 30.b (left), although size was found to be significantly increased in all conditions at day 30 and 90 compared to day 2, the magnitude of this change was very small for microgels stored at 4°C. Indeed, in the case of samples stored at 4°C for 30 days, median size only changed by +4% and +5% for non-degradable and degradable microgels, respectively. In the case of non-degradable microgels, this change could be due to the temperature enhancing the rate of hydrolysis of the ester bonds, which come from the acrylated groups of the PEG polymer. Although peptide-crosslinked microgels also contain ester groups that can be hydrolysed in a temperature-dependant manner, the greater extent of this phenomenon suggest that another parameter was interfering with the microgel stability. In spite of the microgels being suspended in a buffer containing 1% (v/v) antimicrobials, these formulations were neither prepared in aseptic conditions nor sterilised at the end of the fabrication process. As a consequence, the possibility for the suspensions to contain small amounts of bacteria, and thus bacteria-derived proteases that could degrade the peptide, cannot be ruled out and implementing techniques to reduce the probability of bacterial contamination may be able to solve the issue.

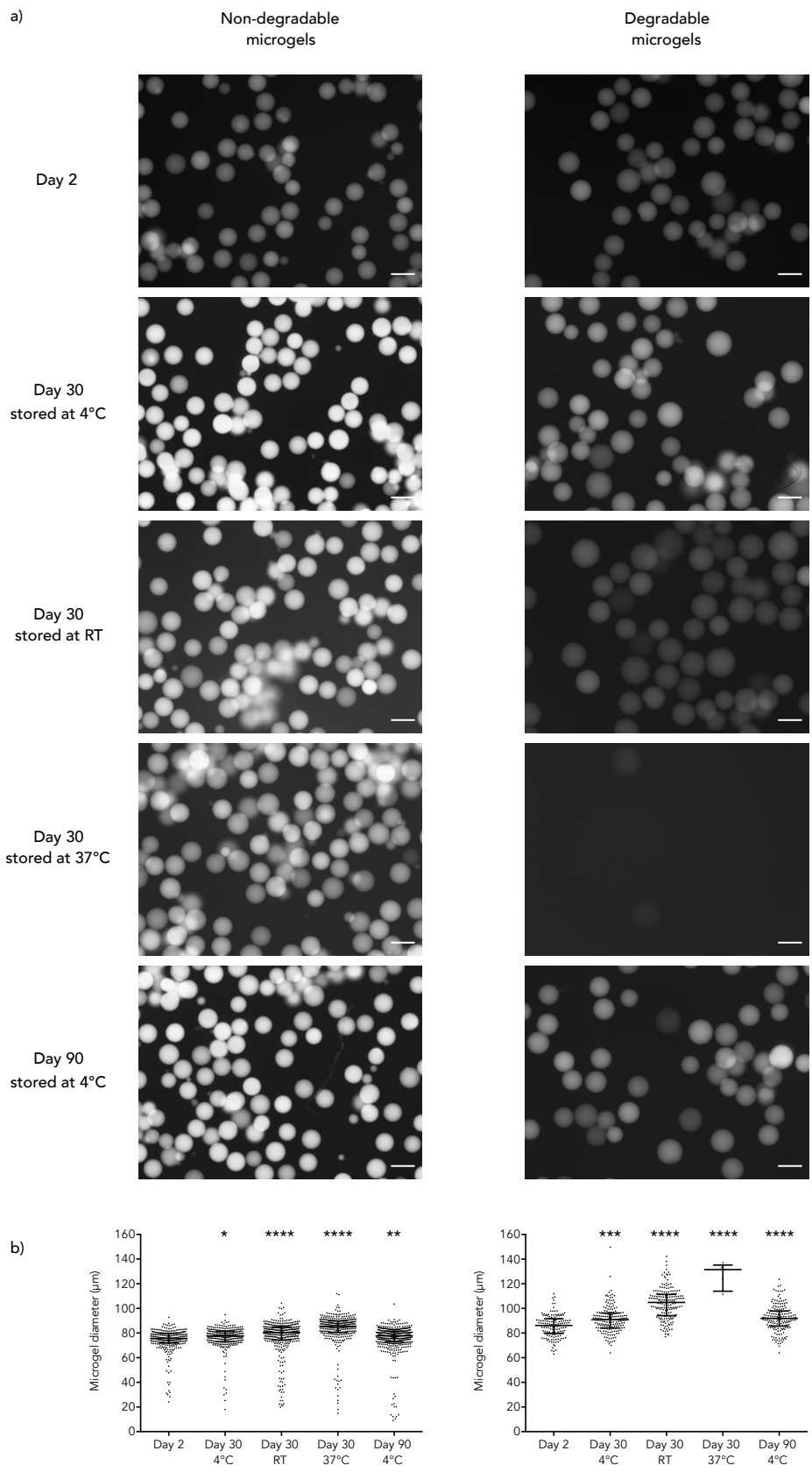
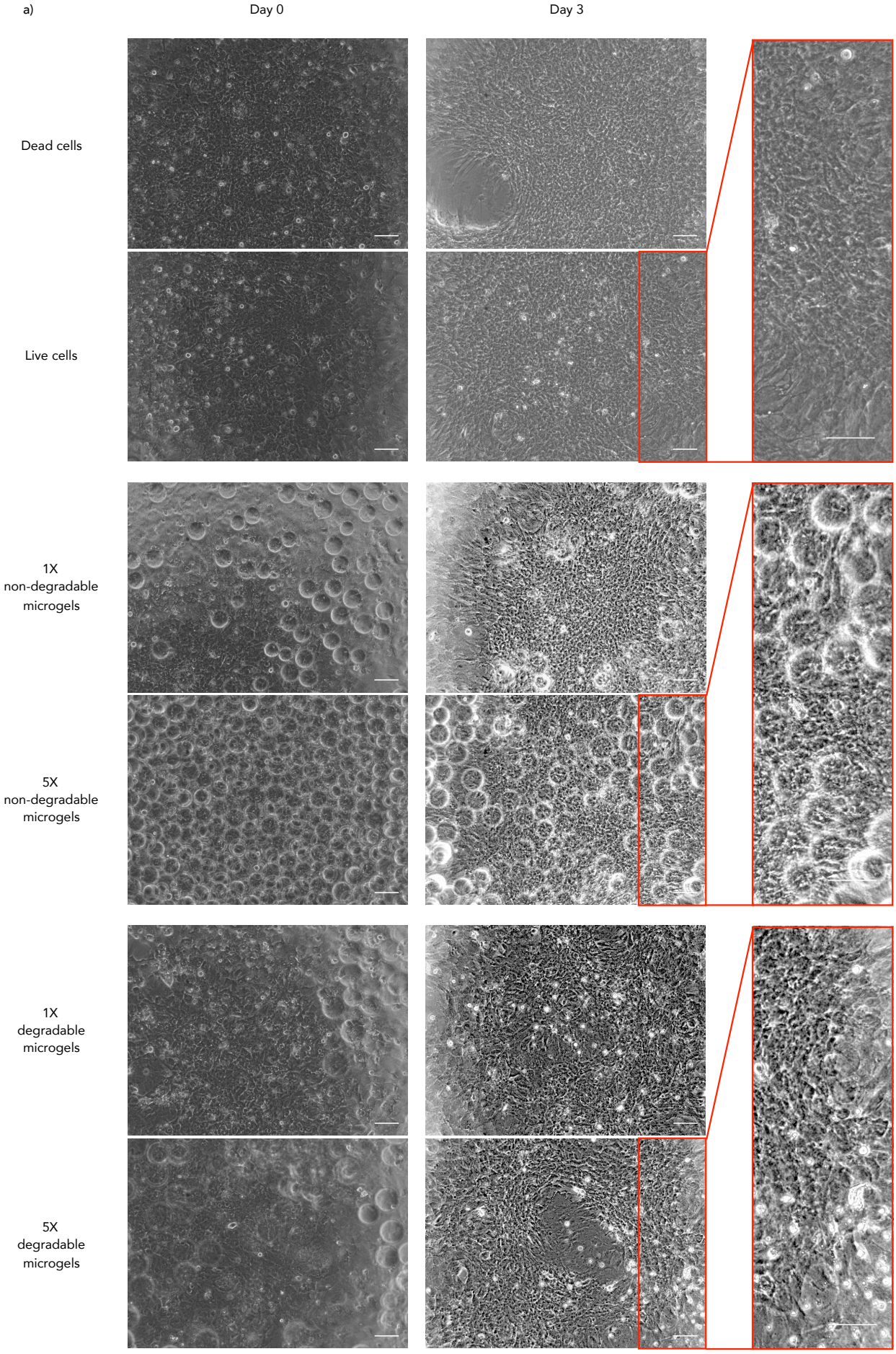


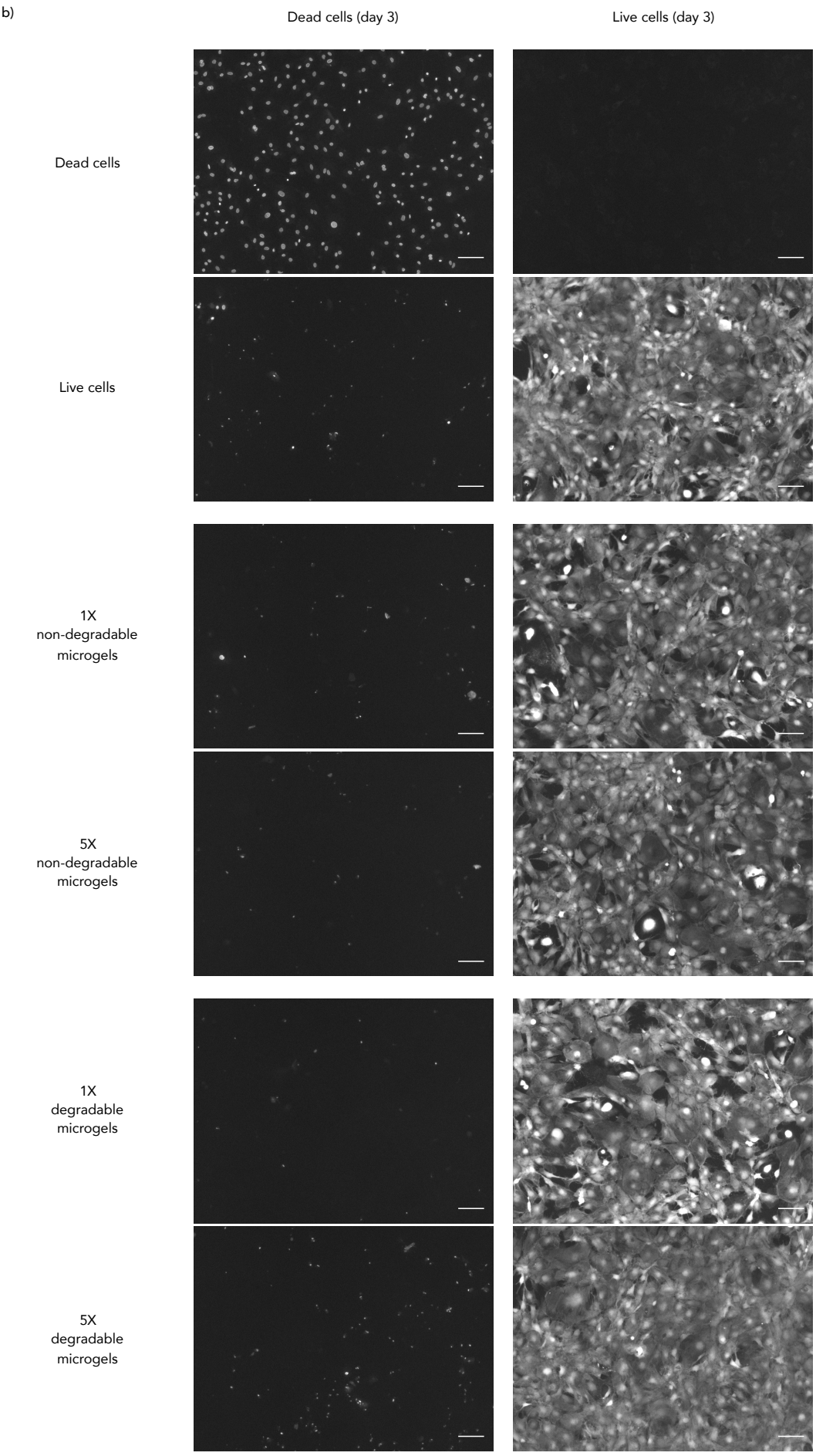
Figure 30: Microgel stability during storage. a) Representative pictures (scale bar = 100 µm) and b) size analysis of non-degradable and degradable microgels stored for 30 to 90 days at various temperatures (median with interquartile range). Swelling is indicative of microgel degradation, predominantly through bulk degradation. Although size was found to be significantly increased in all conditions at day 30 and 90, the magnitude of this change was very small for microgels stored at 4°C (Kruskal-Wallis test with Dunn's correction, all groups compared to day 2, * $p = 0.0175$, ** $p = 0.0034$ and **** $p < 0.0001$ for non-degradable microgels, *** $p = 0.0003$ and **** $p < 0.0001$ for degradable microgels).

3.2.2. Microgel cytotoxicity

Microgel cytotoxicity was assessed by exposing neonatal rat cardiac fibroblasts in culture to non-degradable or degradable microgels for 72 hours and measuring cell viability by using a live/dead staining and a flow cytometry analysis with DAPI. Two microgels concentrations were tested, 1X and 5X. No major morphological difference was observed between conditions after 72 hours of exposure (Figure 31.a). Interestingly, in both conditions using degradable microgels, all microgels had degraded after 72 hours, due to the presence of proteases secreted by the cells in the culture media. As seen in Figure 31.b, live/dead staining revealed that, except for the condition in which cells were exposed to 5X degradable microgels, all conditions showed similar levels of cell viability to the live cells control. A quantification of cell viability was also performed by flow cytometry analysis using DAPI staining, which labels cells with permeabilised plasma membranes. Although no significant difference in viability was found between untreated live cells and microgel-treated cells, there was a trend for lower viability in cells treated with 5X degradable microgels (Figure 31.c). This could be due to the presence of products of microgel degradation in higher amount compared to the 1X condition. Further investigations are required to determine the safe microgel dosage range.


a)
Day 0
Day 3
Dead cells
Live cells
1X non-degradable microgels
5X non-degradable microgels
1X degradable microgels
5X degradable microgels

b)


Dead cells (day 3)
Live cells (day 3)
Dead cells
Live cells
1X
non-degradable
microgels
5X
non-degradable
microgels
1X
degradable
microgels
5X
degradable
microgels

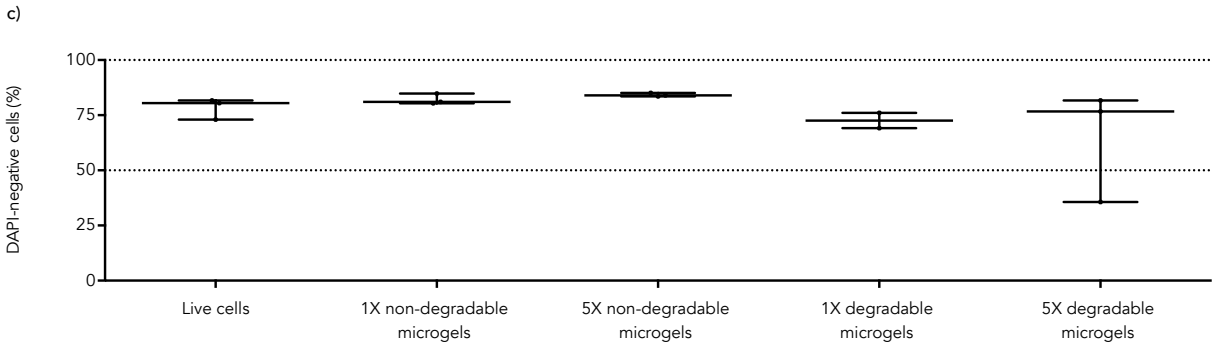


Figure 31: Microgel cytotoxicity. a) Representative pictures of neonatal rat cardiac fibroblasts exposed to non-degradable and degradable microgels at two different concentrations. No major morphological difference was observed between conditions after 72 hours of exposure (scale bar = 100 µm). b) Representative pictures of a live/dead staining performed on the exposed cells. Except for the condition in which cells were exposed to 5X degradable microgels, all conditions showed similar levels of cell mortality to the live cells control (scale bar = 100 µm). c) Cell mortality quantification analysed by flow cytometry using DAPI. No significant difference in cell viability was found between control untreated live cells and the microgel-treated cells (Kruskal-Wallis test with Dunn's correction, all groups compared to live cells).

3.3. Microgel degradation

3.3.1. Trypsin-mediated degradation

Microgel degradability was evaluated using both trypsin, which is a non-specific protease, and MMP-9. Although trypsin is not present in the human body, this enzyme provides provides an effective and affordable option for studying protease-mediated degradation. Degradation was assessed by quantifying the amount of crosslinked AlexaFluor™ 488 fluorophore released by the microgels upon enzyme exposure.

A first degradation assay was performed at RT using a high concentration of trypsin (0.5% or 21 µM) on fluorescent non-degradable and degradable microgels. Images of the microgels taken before adding the trypsin and every 2 min after adding the enzyme are provided in Figure 32. A high concentration of trypsin had no effect on the non-degradable microgels, whereas progressive microgel degradation was observed in the wells containing the peptide-crosslinked degradable microgels. More particularly, degradable microgels appeared to swell and become less fluorescent over time. This suggests that the hydrogel network was degrading predominantly through bulk degradation, meaning that the trypsin

could diffuse through the pores and cleave the peptide bonds within the microgels and not only at their surface.

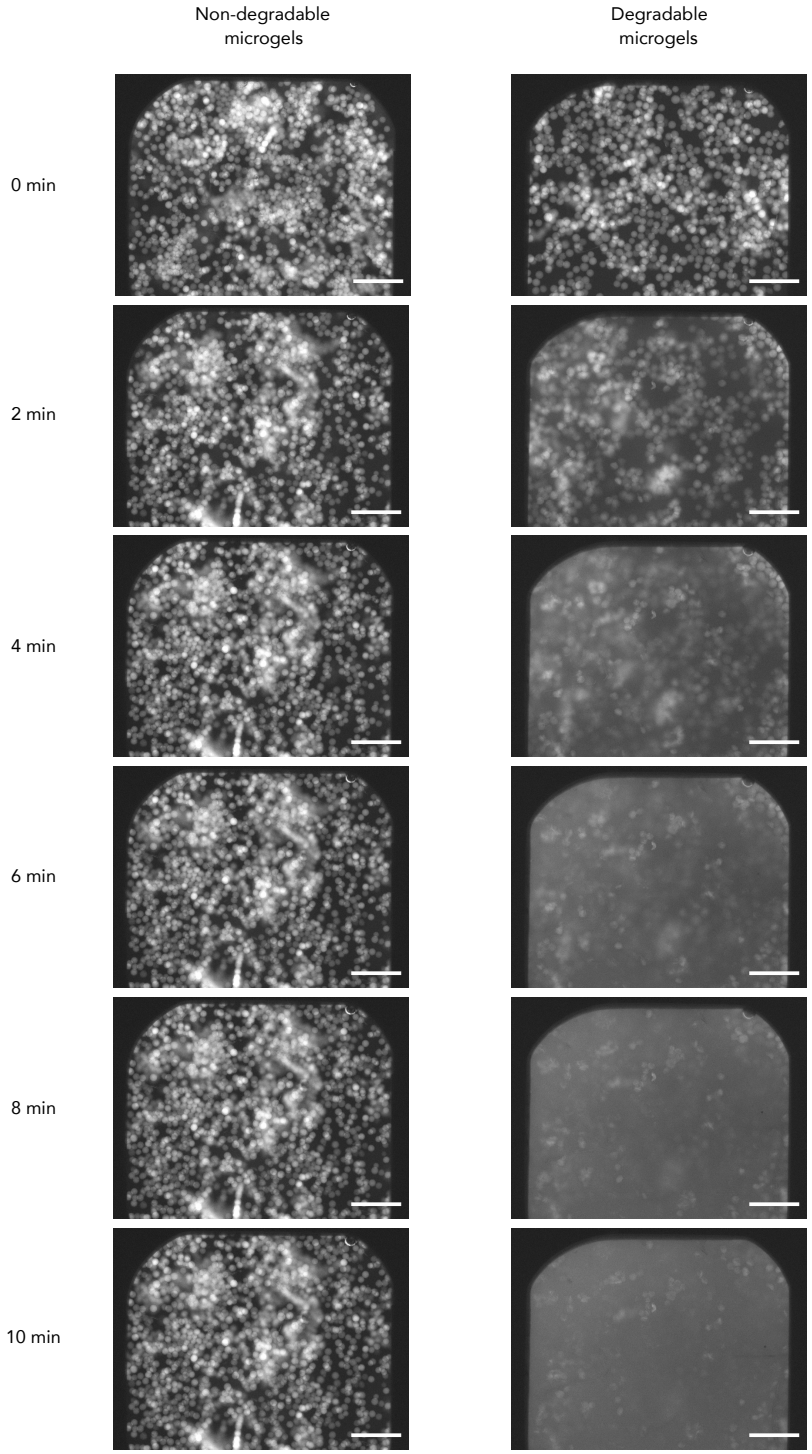
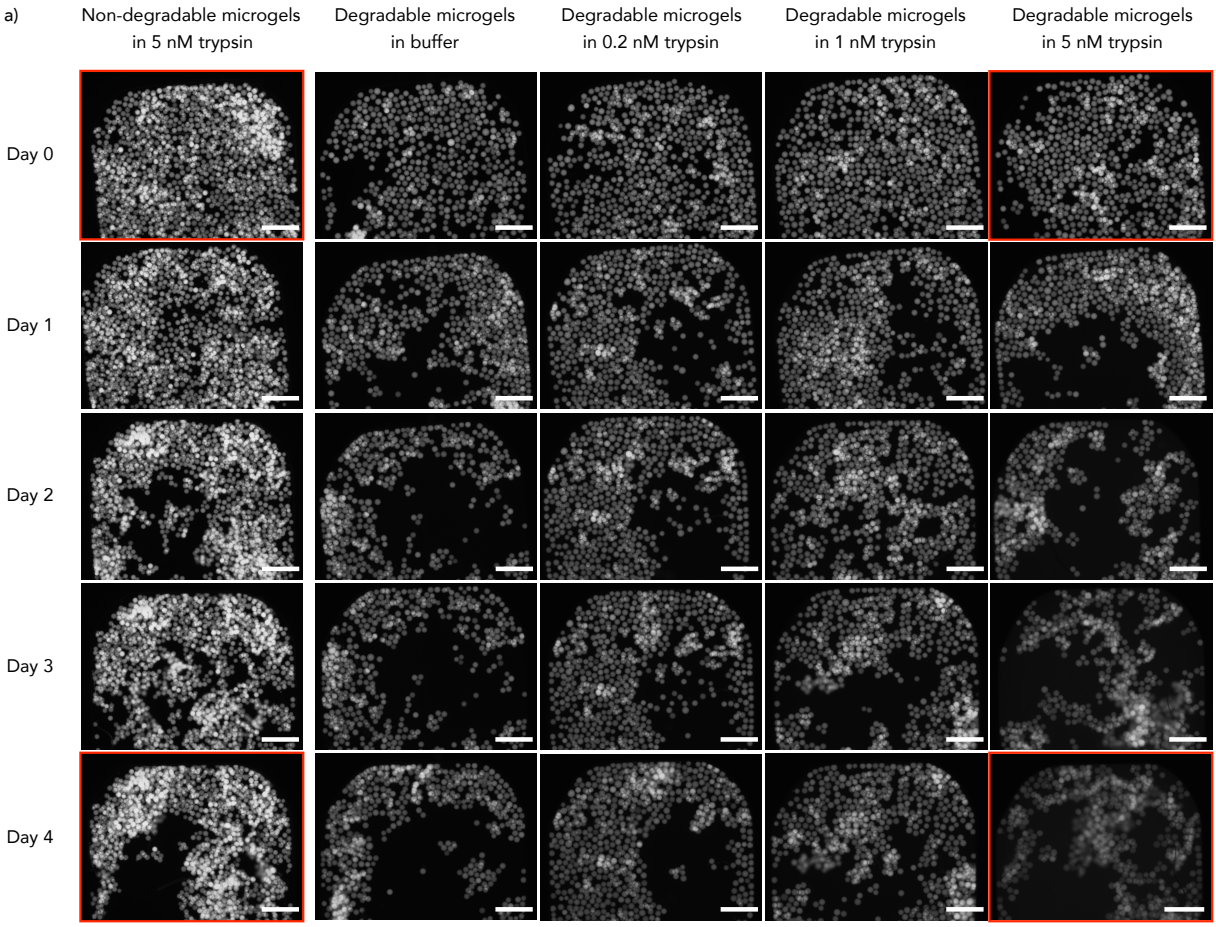
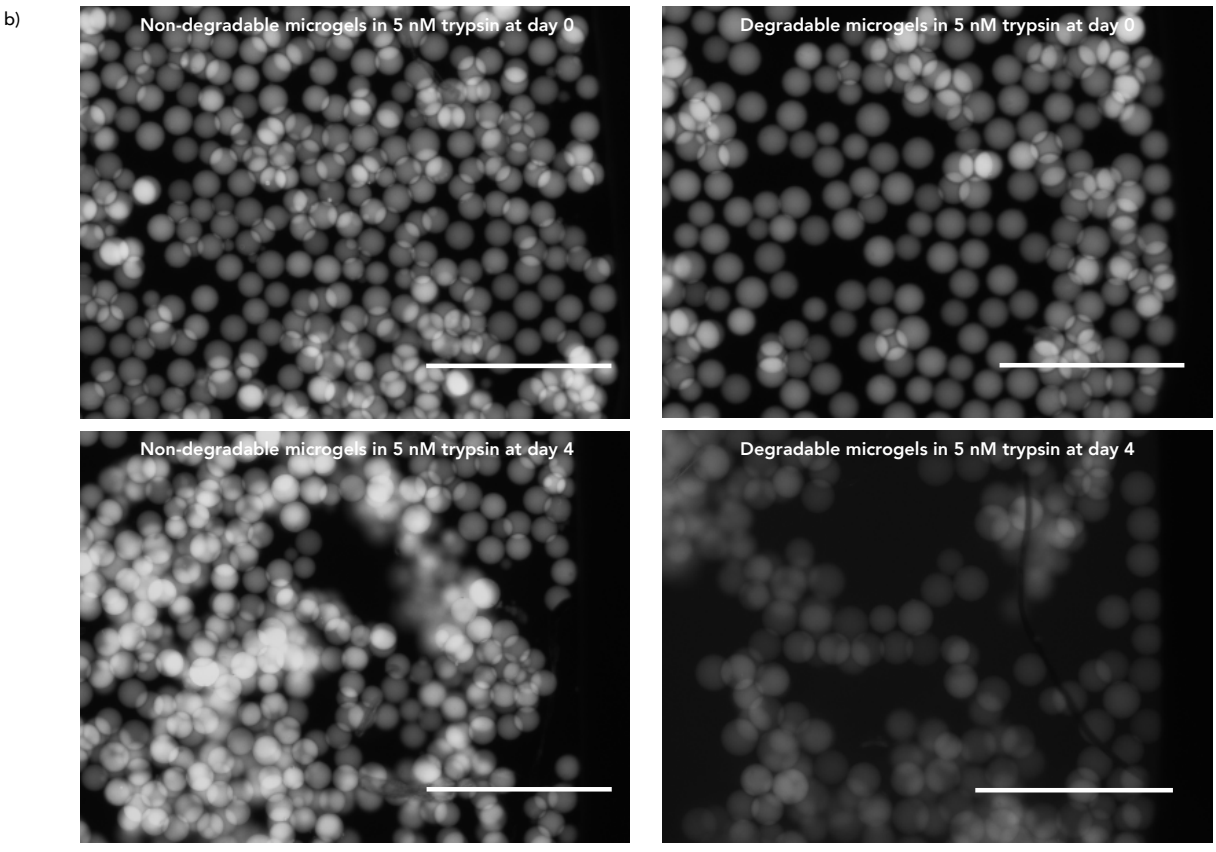


Figure 32: Microgel degradation using a high concentration of trypsin (21 μM). Trypsin had no observed effect on the non-degradable microgels, whereas progressive microgel degradation was observed in the wells containing the peptide-crosslinked degradable microgels (scale bar = 500 μm).


a)
Non-degradable microgels in 5 nM trypsin
Degradable microgels in buffer
Degradable microgels in 0.2 nM trypsin
Degradable microgels in 1 nM trypsin
Degradable microgels in 5 nM trypsin
Day 0
Day 1
Day 2
Day 3
Day 4


b)
Non-degradable microgels in 5 nM trypsin at day 0
Degradable microgels in 5 nM trypsin at day 0
Non-degradable microgels in 5 nM trypsin at day 4
Degradable microgels in 5 nM trypsin at day 4

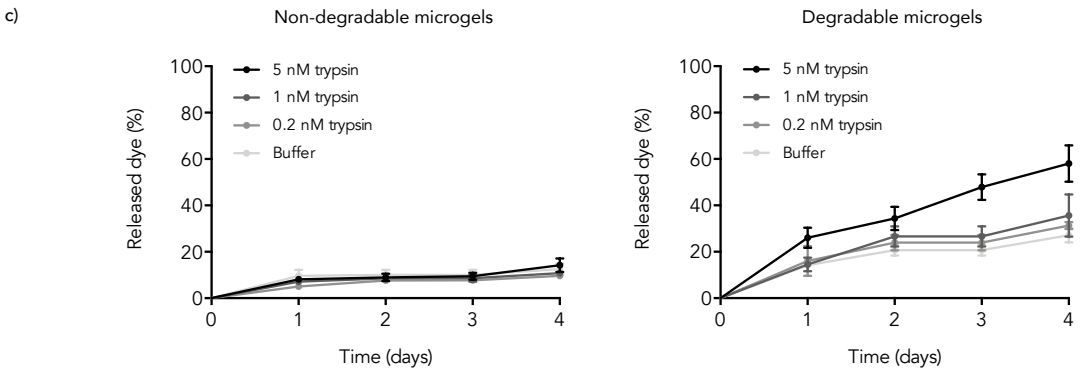


Figure 33: Microgel degradation using a range of nanomolar concentrations of trypsin. a) Representative pictures of fluorescent non-degradable and degradable microgels treated with 0, 0.2, 1 or 5 nM trypsin for 4 days at 37°C. Non-degradable microgels did not change in size or fluorescence in the presence of trypsin. However, degradable microgels appeared to slowly swell and lose fluorescence over time in the presence of trypsin, which suggests that the microgels were degrading predominantly through a bulk degradation mechanism (scale bar = 500 µm). b) Close up pictures of the degradable and non-degradable microgels treated with trypsin at day 0 and 4. c) Quantification of the fluorescent dye released in the supernatant (n = 3, mean ± SD). Background levels of fluorescence of the crosslinked dye (10%) were released between day 0 and day 1 in all wells containing non-degradable microgels. In wells containing degradable microgels, 58% of the crosslinked fluorophore was released in 4 days using 5 nM trypsin, compared to 48% in the wells treated with 1 nM trypsin wells, 34% in the wells treated with 0.2 nM trypsin wells and 26% in control wells exposed to the enzyme buffer only.

In a second experiment, fluorescent non-degradable and degradable microgels were treated with a range of trypsin concentrations (0.2, 1 and 5 nM) for 4 days at 37°C (Figure 33). Images of the microgels taken every day are provided in Figure 33.a. Non-degradable microgels did not change in size or fluorescence in the presence of trypsin. However, similarly to the results obtained in the previous experiment, degradable microgels appeared to slowly swell and lose fluorescence over time in the presence of trypsin, which suggests that the microgels were degrading predominantly through a bulk degradation mechanism. In addition, degradation seemed to be more pronounced for degradable microgels treated with higher concentrations of trypsin.

The released dye was also measured in each well as each time point to estimate the extent of the degradation. As shown in Figure 33.b, approximately 10% of the crosslinked dye was released between day 0 and day 1 in all wells containing non-degradable microgels. This could be explained by the fact that free dye was had not been entirely removed from the microgel suspension, which resulted in background levels of fluorescence. On the other hand, in wells containing degradable microgels, fluorescence continuously increased over the 4 day-experiment in all wells, which is indicative of a progressive degradation. In the

wells exposed to buffer only, the increase in fluorescence was likely to be due to the non-specific degradation of the peptide crosslinker by proteases present in the environment, as mentioned in section 3.2.1. However, dye release was found to be faster when using higher concentrations of trypsin, which suggests that the degradation rate can be modulated by varying the enzyme concentration within the range investigated here. More specifically, In wells containing degradable microgels, 58% of the crosslinked fluorophore was released in 4 days using 5 nM trypsin, compare to 48% in the wells treated with 1 nM trypsin wells, 34% in the wells treated with 0.2 nM trypsin wells and 26% in control wells exposed to the enzyme buffer only. .

3.3.2. MMP-9-mediated degradation

Finally, degradable microgel sensitivity to MMP-9 was evaluated exposing them to a physiologically relevant concentration of MMP-9 [240] over a period of 4 days (Figure 34). Progressive degradation was observed to a higher extent in the control group (55% at day 4), which could be explained by a potential bacterial contamination. However, higher release rates were observed in the wells exposed to MMP-9, with about 90% at day 4. These results indicate that the peptide can successfully be cleaved by MMP-9 within the microgels and thus be used to make them sensitive to this enzyme.

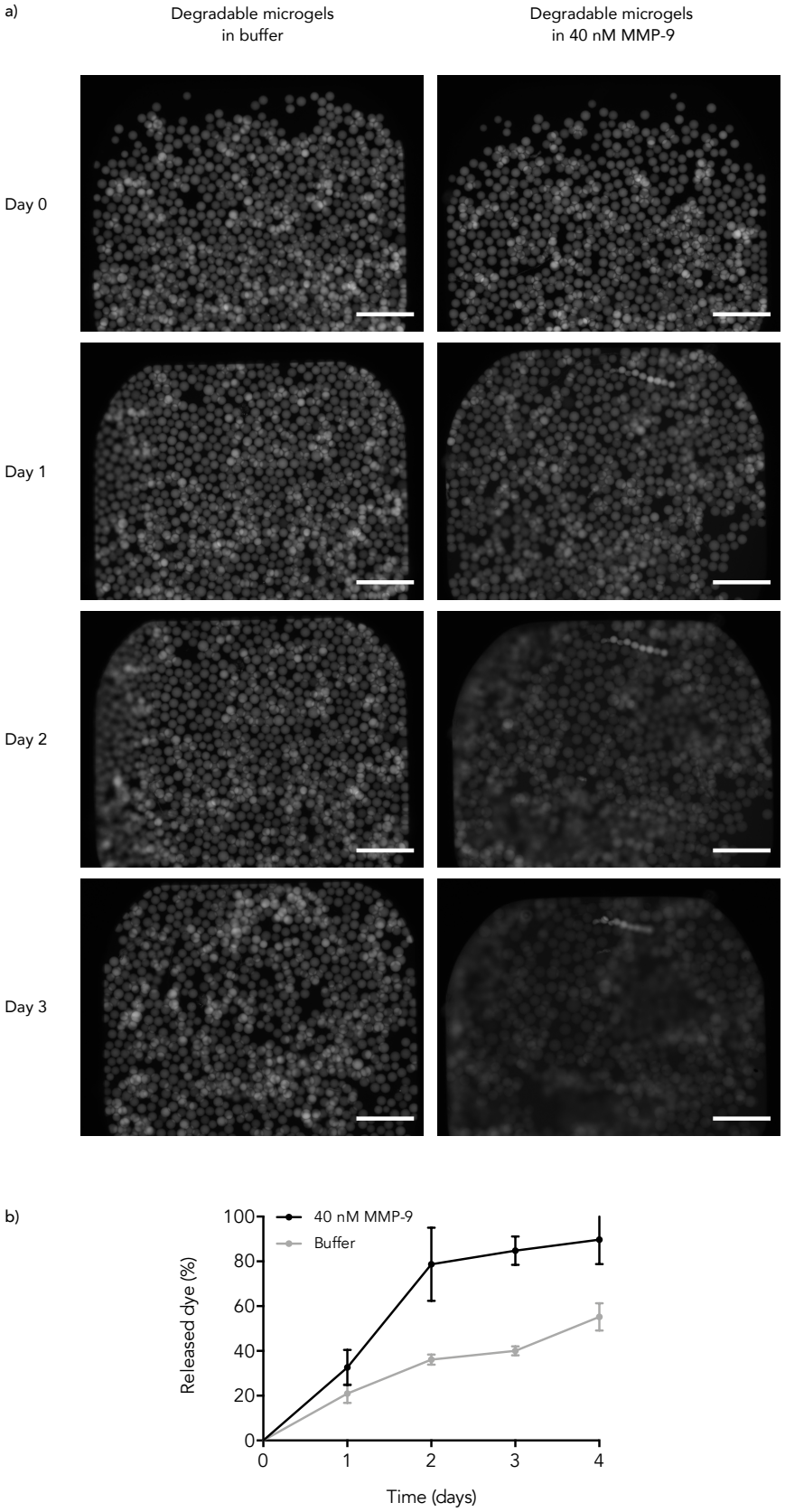


Figure 34: Microgel degradation using MMP-9. a) Representative pictures of fluorescent degradable microgels treated with 0 or 40 nM MMP-9 for 4 days at 37°C (scale bar = 500 µm). b) Quantification of the fluorescent dye released in the supernatant (n = 3, mean ± SD). Progressive degradation was observed in the control group (55% at day 4), which could be explained by a potential bacterial contamination. However, higher release rates were observed in the wells exposed to MMP-9, with about 90% at day 4.

4. Conclusion

In this chapter, an MMP-2/9-sensitive peptide crosslinker was synthesised and characterised. This peptide could be cleaved in the presence of physiologically relevant concentrations of MMP-2 or MMP-9, and thus could be used to make environmentally-sensitive hydrogels for heart repair. The composition of two buffers was optimised to ensure both EV and crosslinker stability during the microgel fabrication process, and to tune the crosslinking kinetics to a timeframe that was compatible with the microfluidics platform developed in Chapter 1. Hydrogels prepared using either a non-degradable PEG dithiol crosslinker or the synthesised peptide crosslinker presented similar biomechanical properties to the native muscle tissue. Both formulations were found to have a porosity that was appropriate for the encapsulation of nanosized particles such as EVs, as suggested by their estimated mesh size. Importantly, monodisperse microgels could successfully be fabricated using the newly synthesised degradable peptide crosslinker. Although microgel size was found to significantly increase over time using various storage conditions, the magnitude of these changes was very small when stored at 4°C for 30 days. Suboptimal stability could be explained by the presence of hydrolysable ester bonds on the polymer backbone of both microgel types as well as the sensitivity of the degradable peptide to proteases that are found ubiquitously in the environment. Both non-degradable and degradable microgels were found to be non-cytotoxic at lower concentrations as assessed by DAPI and live/dead stainings. The microgel sensitivity to trypsin, a non-specific enzyme, and MMP-9 was investigated, and revealed that the peptide-crosslinked microgels could be almost entirely degraded in 4 days using a concentration of MMP-9.

The synthesised degradable peptide crosslinker allowed to control the microgel degradation over a period of 4 days using MMP-9. Although the concentration of enzymes used for the degradation experiments are relevant to the application [240], such *in vitro* assays cannot accurately recapitulate the environment found in native tissues. Indeed, native MMPs have been shown to be more active than their synthetic equivalents due to differences in post-translational modifications [242]. It is thus essential to extend this work

with additional *in vivo* experiments aiming at adapting the degradation profile of the microgels to the infarcted heart environment, as well as ensuring that the release profile of the encapsulated EVs would cover an adequate period of time to induce optimal beneficial effects. More specifically, tuning the microgel degradation kinetics could be achieved using various strategies. First, microgels could be fabricated using a blend of non-degradable and degradable crosslinker to make their degradation slower [192]. The affinity of the two MMPs could also be altered by amending the sequence of peptide crosslinker [176]. Finally, the polymer (*e.g.* number of arms, MW) and hydrogel formulation (*e.g.* wt%, ratio polymer-crosslinker) could be systematically changed [168]. Imaging tools could also be used to adapt the final product to each individual patient by measuring their MMP activity levels and determining the appropriate formulation for their needs [41].

Prior to conducting extensive *in vivo* efficacy experiments, additional studies investigating the safety of the final product should be performed. As mentioned in Chapter 1, a more robust validation of the microgel washing process is required to ascertain trace levels of these components. The effects of microgel exposure on cell phenotype should be investigated through extensive cytotoxicity experiments performed over longer periods of time. Finally, *in vitro* and *in vivo* studies looking at potential immunogenic reactions against the implanted microgels should be performed, including investigations on the potential risks of immune rejection and capsule formation, which are common side effects of implants.

Finally, the final product stability should be improved to a level that would allow its use as an off-the-shelf product. Indeed, being a ready-to-use product would have many logistical benefits for both the patients and health professionals. As mentioned in 3.2.1., the current lack of stability of the degradable microgels is very likely to be due to contamination issues. The implementation of aseptic methods and/or sterilisation steps in the microgel fabrication process, which would be required before further use in clinical trials, should be sufficient to provide satisfactory levels of stability. Other preservation methods, such as freeze-drying or the use of preservative agents, could also be employed to help stability, providing they are compatible with the drugs loaded into the microgels (*e.g.* EVs).

Chapter 4 Environment-sensitive microgels for EV delivery: a proof of concept

1. Introduction

Using MMP-sensitive microgels to deliver EVs offers two potential benefits: improving retention at the site of administration and providing a sustained and environmentally-responsive release of EVs to the surrounding damaged tissue. EVs can be loaded into microgels through entrapment within the pores of the hydrogel network or tethering to the polymer backbone. In most cases, tethering requires the modification of the cargo and/or the polymer to incorporate functional handles that allow conjugation, methods that risk reducing the cargo bioactivity. In addition, as seen in Chapter 3, mesh size was estimated to be in the diameter range of EVs, which supports the idea that tethering may not be necessary to efficiently load the EVs into the microgels. Thus, in a first attempt to demonstrate the feasibility of producing EV-loaded microgels, EVs were simply entrapped in the hydrogel network by adding them to the PEG acrylate polymer solution used for the microgel fabrication.

Using this loading strategy, it is hypothesised that releasing the entrapped EVs from MMP-2/9-sensitive microgels could be accomplished through degradation of the hydrogel network and diffusion of the EVs into the surrounding tissue (Figure 35). More specifically, degradation would be achieved predominantly *via* cleavage of the MMP-2/9-sensitive peptide crosslinker in the presence of either of these enzymes or any broad-spectrum protease. To a lesser extent, nonspecific hydrolysis of the ester bonds formed during the crosslinking reaction between the thiolated crosslinker and the acrylated polymer may also contribute to the degradation of the microgels.

The capacity to load and release EVs from MMP-2/9-sensitive microgels is investigated in this chapter. EVs were purified from the conditioned media of cells in culture and fully characterised. An EV labelling protocol was optimised to enable the preparation of fluorescent DiD-labelled EVs. These EVs were used to fabricate EV-loaded hydrogel patches and EV-loaded microgels. EV loading was assessed by rheometry, fluorescence microscopy and ultrastructural imaging. EV-loaded patches and microgels were then degraded and the

presence of intact EVs in the degradation products was investigated. An EV uptake assay using primary cardiac cells was developed and used to assess EV integrity before and after the loading and release processes. Finally, DiD-labelled EVs and DiD-EV-loaded degradable microgels were administered subcutaneously in mice in order to evaluate the capacity for *in vivo* visualisation and tracking.

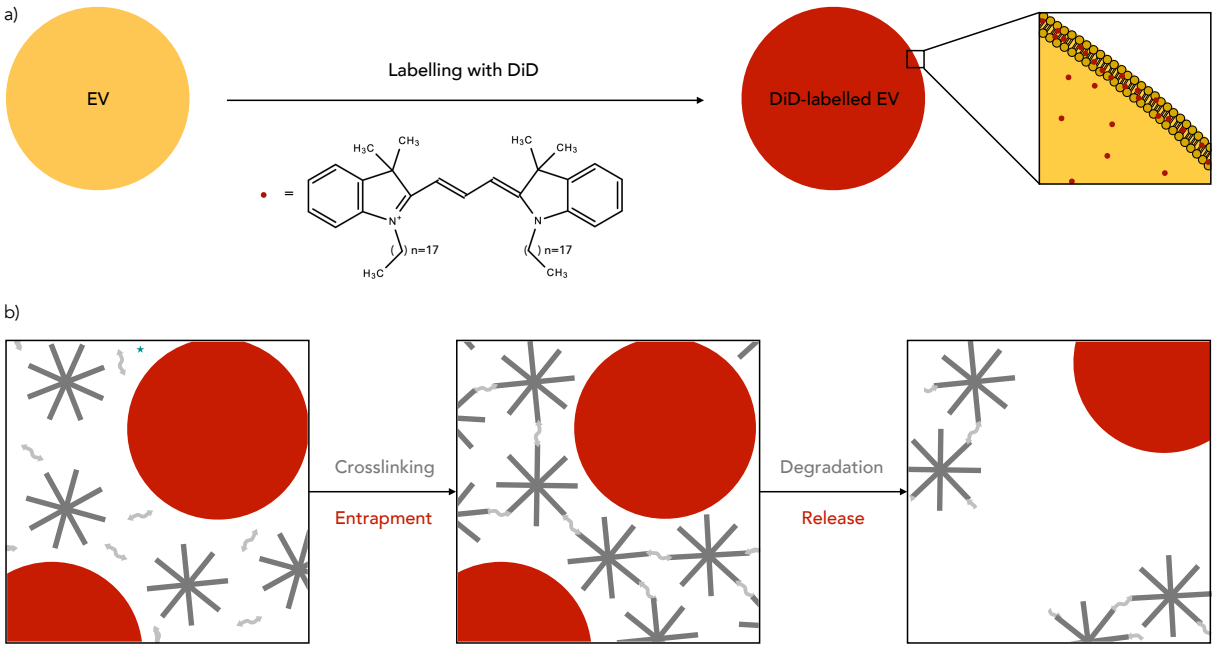


Figure 35: Overview of the EV labelling using DiD (red dot) (a), loading and release (b) strategy. The EVs (red) are entrapped in the hydrogel pores upon crosslinking of the PEG-acrylate (dark grey) with the MMP-2/9-sensitive crosslinker (light grey). EVs can be released by diffusion through the pores following degradation of the polymer backbone.

2. Materials and methods

2.1. Materials

Alexa Fluor™ 488 C5 Maleimide (A10254, MW 720.66), Alexa Fluor™ 488 Phalloidin (A12379), Alexa Fluor™ 647 (A20006), antibiotic-antimycotic (A/A) 100X (15-240-062), BSA (A2153), CD63 monoclonal antibody (10628D), CD9 monoclonal antibody (10626D), CD81 monoclonal antibody (10630D), DAPI (D1306), DiD' oil; DiIC18(5) oil (1,1'-Dioctadecyl-3,3,3',3'-Tetramethylindodicarbocyanine Perchlorate) (D307), DPBS without calcium and magnesium 1X (14-190-144), DMEM high glucose GlutaMAX™ supplemented with pyruvate (10569010), DTNB (22582), FreeStyle™ 293-F Cells (R79007), FreeStyle™ 293 Expression Medium (12338018), Micro BCA™ Protein Assay Kit (23235), penicillin-streptomycin (P/S) 10,000 U/mL (15-140-148), trypsin-EDTA 0.05% (25300054) and trypsin-EDTA 0.5% (15400054) were purchased from Fisher Scientific. Acetone (24201), PEG dithiol crosslinker (717142, average Mn 1000), Sepharose® CL-2B, skimmed milk powder (70166), Triton™ X-100 (X100) and Tween® 20 (P1379) were purchased from Sigma-Aldrich. 8-arm PEG-acrylate (tripentaerythritol) (MW 20740) was purchased from JenKem Technology USA. TBS 10X was purchased from Bio-Rad. Osmium tetroxide 4% (19150), paraformaldehyde aqueous solution 16% (PFA) (15710) and uranyl acetate (22400) was purchased from Electron Microscopy Sciences. IRDye® 800CW goat anti-Mouse IgG secondary antibody (926-32210) was purchased from LI-COR Biosciences.

2.2. Methods

2.2.1. EV purification and characterisation

Floating human embryonic kidney cells (FreeStyle™ 293-F Cells) were cultured at 37°C under 5% CO_2 in FreeStyle™ 293 Expression Medium 1% (v/v) P/S 1% (v/v) A/A. The conditioned media were collected twice a week, 0.45 µm-filtered and stored at 4°C until further processing. A concentration step using a Vivacell® 250 device with a Vivacell 250

100K MWCO filter (Sartorius) was then performed at 4°C. More specifically, each filter was used to concentrate 1.5 L of conditioned media into approximately 10-20 mL under 4 bar-pressure. This was followed by a second concentration step using an Amicon Ultra-15 Centrifugal Filter Unit (UFC910008, Merck Millipore) to further reduce the volume down to 1 mL. For this step, the centrifugation speed was set to 5000 rpm. The sample was then purified by size exclusion chromatography (SEC). Briefly, PBS-antimicrobials was prepared with 1% (v/v) A/A and 1% (v/v) P/S. A 1 cm diameter column was packed with Sepharose® CL-2B to a depth of 30 cm and rinsed with 60 mL PBS-antimicrobials. A volume of 500 µL sample was added to the top of the column and left to enter the column. PBS-antimicrobials was then added to the top and 30 1 mL fractions were collected into separate tubes.

The particle concentration and hydrodynamic diameter was measured on each fraction using NTA. Briefly, samples were diluted in PBS-antimicrobials to reach the linear range of NTA measurements, which is between 10^8 x 10^9 particles/mL. Three 30 s videos were recorded using a NanoSight NS300 (Malvern Panalytical). Acquisition was performed at a camera level of 14. Analysis was performed using a detection threshold of 10. The total protein content was measured using a Micro BCA™ Protein Assay Kit. However, due to issues with the preparation of the standard curve, protein concentration was not calculated and the data was plotted as a normalised signal intensity. Finally, the presence of EV markers (CD9, CD63 and CD81) in the fractions was detected by dot blotting. Briefly, a 1X TBS solution was prepared by diluting 10X TBS with MilliQ water. A TBS-T solution was prepared by adding 0.1% (v/v) Tween® 20 to the TBS solution. A 0.45 µm nitrocellulose membrane (162-0117, Bio-Rad) was equilibrated in TBS for 10 min and installed into a 96-well Bio-Dot® microfiltration device (1703938, Bio-Rad). The wells were rehydrated with 100 µL TBS and allowed to drain. 80 µL of sample was added to the corresponding wells and allowed to pass through. Each well was washed three times with TBS. The membrane was then removed from the device, blocked using 5 wt% skimmed milk in TBS-T for 1 h at RT and incubated overnight on a shaker at 4°C with the primary antibody solution (CD9, CD63 or CD81 monoclonal antibody, dilution 1:1000 in TBS-T with 5% BSA). The membrane was then washed three times with TBS-T and incubated for 1 h at RT with the secondary

antibody (goat anti-mouse IgG, dilution 1:10000 in TBS-T). After three washes in TBS-T, the membrane was imaged with an Odyssey® near-infrared fluorescence imaging system (LI-COR Biosciences). Finally, fractions containing EVs (7 to 11) were pooled and the resulting suspension was analysed by NTA.

2.2.2. DiD-labelled EV production and characterisation

The pooled EV suspension prepared in section 2.2.1 was labelled using DiD. The labelling method was optimised as described in section 3.1.2. Briefly, EVs were incubated with 0.5 or 5 µM DiD for 2 h at 4°C under agitation (300 or 1000 rpm) using a ThermoMixer® C (Eppendorf) ("DiD-EVs"). Control samples were prepared using PBS-antimicrobials in place of the EV suspension ("DiD"). Both samples were then concentrated using an Amicon Ultra-15 Centrifugal Filter Unit ("cc DiD-EVs" and "cc DiD") and buffer was exchanged for the HEPES buffer prepared in Chapter 3. NTA analysis was then performed on DiD-EVs, DiD, cc DiD-EVs and cc DiD.

Labelling efficiency and particle hydrodynamic diameter were assessed by fluorescence correlation spectroscopy (FCS) on a commercial LSM 880 (Carl Zeiss) equipped with an incubation chamber set to 37°C. All FCS measurements and analysis were performed by Dr. Adrian Najer (Imperial College London). A HeNe laser was used as excitation source at a wavelength of 633 nm and an appropriate filter sets were used to detect the fluorescence signal. The laser beam was passed through a 40X C-Apochromat water immersion objective with a numeric aperture of 1.2 to focus the beam into the sample droplet. A 5 µL droplet of sample was put on an ibidi glass bottom 8-well plate and all the measurements were performed 200 µm above the glass surface. A 25 nM AlexaFluor™ 647 solution in PBS was used to calibrate the confocal volume (D = 3.30 x 10-6 cm^2/s at 25°C, and when corrected for the higher temperature used: D = 4.42 x 10-6 cm^2/s at 37°C) [243]. For each sample, 25 x 5 s intensity traces were recorded, autocorrelated and analysed. Autocorrelation curves were created in ZEN software (Carl Zeiss) and the curves were exported for further analysis using PyCorrfit program 1.1.6 [244]. Data was fitted using one component fits ($G_{1comp}(\tau)$) to

obtain the diffusion times (τ_D) for the corresponding sample. A triplet fraction (T) with a triplet time (τ_{trip}) between 1 to 10 µs was included for all the curves.

$$G_{1comp}(\tau) = \left(1 + \frac{T}{1-T} e^{\frac{-\tau}{\tau_{trip}}}\right) * \frac{1}{N * \left(1 + \frac{\tau}{\tau_D}\right) * \sqrt{1 + \frac{\tau}{SP^2 \tau_D}}} \quad (5)$$

N is the effective number of diffusing species in the confocal volume (used to calculate concentrations) and SP is the structural parameter describing the ratio of height to width of the confocal volume (fixed to 5). The following equation relates the x-y dimension of the confocal volume (ω_{xy}^2), which was calibrated by a standard measurement of Alexa Fluor™ 647 in PBS, to the diffusion coefficient (D), which was calculated for each sample using the obtained diffusion time (τ_D):

$$D = \frac{\omega_{xy}^2}{4\tau_D} \quad (6)$$

Einstein-Stokes equation was used to calculate the hydrodynamic radius (R_h) *via* the obtained diffusion coefficients (D). η is the viscosity of the surrounding medium, $k_B$is the Boltzmann constant, and T is the absolute temperature.

$$D = \frac{k_B T}{6\pi\eta R_h} \quad (7)$$

2.2.3. EV uptake

Cardiac fibroblasts were isolated from neonatal rats by Dr. Ivan Diakonov (Imperial College London) using a neonatal heart dissociation kit (130-098-373, Miltenyi Biotec) as described in Chapter 3. Cells were cultured in DMEM high glucose GlutaMAX™ supplemented with pyruvate, 1% (v/v) P/S and 10% (v/v) FBS at 37°C under 5% CO_2 until passage 4. Cells were seeded at 50,000 cells/cm^2 with 300 µL media per well of an ibiTreat 8-well plate.

On the day after seeding, cells were rinsed with warm PBS to remove floating dead cells and fresh media was added to each well. Samples were added to respective wells and plates were incubated at 37°C under 5% CO_2. Untreated cells were used as a negative control. Cells were exposed to six different treatments: DiD, DiD-EVs, cc DiD, cc DiD-EVs and the degradation products from either a cc DiD-EV-loaded patch or cc DiD-EV-loaded microgels. Uptake was assessed after 30 min and after 3 h of exposure to the four first treatments, and after 3 h only for the last two. A total of 10^{10} EVs were added to each EV-treated well (DiD-EVs and cc DiD-EVs) and the same volume of the corresponding control solution was added to the DiD and cc DiD-treated wells. For wells treated with the degradation products, a volume theoretically equivalent to 10^{10} released EVs was added to each well. Four wells were seeded for each condition: three wells for flow cytometry analysis and one well for microscopy.

At the end of the incubation period, wells dedicated to confocal fluorescence microscopy imaging were rinsed with warm PBS and stained. All following steps were performed at RT in the dark. Cells were then fixed using 4% PFA in PBS for 15 min and washed with PBS. This was followed by a permeabilisation step using 0.5% Triton X-100 in PBS for 10 min and a wash in PBS. Cells were then incubated with Alexa Fluor™ 488 Phalloidin for 15 min to label F-actin microfilaments, washed twice in PBS and incubated with DAPI for 10 min to label the nuclei. Finally, cells were washed twice with PBS and stored in this same buffer at 4°C. Cells were imaged on an SP5 inverted confocal microscope (Leica, 20X objective lens) at 405/415-479 nm (DAPI), 488/500-600 nm (Alexa Fluor™ 488 Phalloidin) and 633/650-700 nm (DiD). All images were taken by Dr. James Armstrong (Imperial College London). For wells dedicated to flow cytometry analysis, cells were detached using 0.05% trypsin-EDTA for 5 min at RT and transferred into round-bottom polystyrene tubes. The same volume of media containing 10% (v/v) FBS was added to each sample and all tubes were centrifuged at 300 G for 5 min. The supernatant was then removed, and cells were resuspended in 500 µL PBS. DAPI was added to each tube just before analysing the cell population on a Fortessa flow cytometry (BD) using 405-450/50 (DAPI) and 640-670/14 (DiD) filters. The cell

population was gated on DAPI-negative (viable) single cells and the DiD-negative cell population was gated using the untreated cell sample.

2.2.4. EV-loading into patches and microgels

Hydrogel precursor solutions were prepared as follows. The hydrogel composition was set to 10 wt% polymer with a thiol:acrylate crosslinking molar ratio of 1:1. HEPES and sodium acetate buffers were prepared as described in Chapter 3. The crosslinker solution was prepared by dissolving either the non-degradable PEG dithiol crosslinker or the degradable peptide crosslinker in the sodium acetate buffer, and adding 10 nM Alexa Fluor™ 488 C5 maleimide to provide the hydrogels with a fluorescent label. The PEG-acrylate solution was prepared by dissolving the 8-arm PEG-acrylate in the cc DiD-EV suspended in HEPES buffer.

EV-loaded patches and microgels prepared in the following section were fabricated using the cc DiD-EVs suspended in HEPES buffer (10^{12} EV/mL), in place of the plain HEPES buffer. Mixing of the two hydrogels precursors solutions using a 1:1 ratio resulted in a final theoretical cc DiD-EV loading concentration of 5 x 10^{11} EV/mL hydrogel for patches or 5 x 10^{10} EV/mL of 10% (v/v) microgel suspension.

The crosslinking kinetics was compared between the unloaded and cc DiD-EV-loaded formulations using rheometry. The elastic (G') and viscous (G'') contributions to shear modulus of the non-degradable and degradable, unloaded and EV-loaded hydrogels were measured using an AR2000ex rheometer (TA instruments) and an 8 mm sst plate. The gap was set to 500 µm and temperature to 25°C. The hydrogel precursor solutions were mixed at a 1:1 ratio and 40 µL of the solution was placed onto the plate. G' and G'' were measured for 10 min using a normal force of approximately 0.35 N, a 1% strain and a 1 Hz frequency.

Unloaded and cc DiD-EV-loaded microgels were prepared using the setup and methods described in Chapter 2 and more specifically using a type-2 chip, 2.5 m-long outlet tubing, and a 10% (v/v) Span® 80 concentration. The oil phase and aqueous phase flow rates were set to 30 µL/min and 0.5 µL/min, respectively. Microgels were collected for 2 h and washed using the protocol described in Chapter 2.

The fabricated unloaded or cc DiD-EV-loaded patches and microgels were imaged on an SP5 inverted confocal microscope (Leica, 20X objective lens) at 488/500-600 nm (Alexa Fluor™ 488) and 633/650-700 nm (DiD). All images were taken by Dr. James Armstrong (Imperial College London). For Focused Ion Beam milling combined with Scanning Electron Microscopy (FIB-SEM) imaging, samples were prepared by high-pressure freezing and freeze substitution (HPF-FS) using an EM PACT 2 HPF (Leica) and an AFS2 freeze substitution machine (Leica). Sample preparation was performed with the help of Jelle Penders (Imperial College London) and sample embedding and imaging was performed by Dr. Qu Chen (Imperial College London). The HPF was cooled with liquid N_2. A volume of 1 µL of 10% (v/v) cc DiD-EV-loaded microgel suspension was pipetted in gold carriers (1.2 mm x 200 µm) and samples were frozen with HPF. Correct freezing was verified for each sample by monitoring the pressure/temperature. Samples were transferred into liquid N_2 to the FS, which was precooled to -90°C with acetone added as a surrounding media. The carriers containing the samples were then transferred into precooled acetone-filled tubes supplemented with 0.5% (v/v) osmium tetroxide and 0.1% (v/v) uranyl acetate. The tubes were transferred to the FS machine and brought to 0°C overnight with 5°C/h. Samples were taken out of the FS machine and washed in acetone, embedded into Quetol 651 (TAAB Laboratories Equipment) and cured in BEEM® Embedding Capsules Size 00 (Electron Microscopy Science) at 60-65°C for 40 h. Ultra-thin sections (65 nm) were made by ultramicrotomy (RMC PowerTome) with a 45° diamond knife (Diatome) and collected on conductive silicone wafers for FIB-SEM imaging. A 4 nm carbon coating (Leica) was then deposited on the sections to make them conductive and more stable under electron beam. FIB-SEM images were taken using a Zeiss Auriga at 1.49 kV with ESB detector.

2.2.5. EV release and uptake

Cc DiD-EV-loaded patches and microgels were prepared using the methods described in section 2.2.4. Eight 48-wells were coated with 2 wt% BSA at 4°C for 2 h, washed three times with PBS-antimicrobials and dried with N_2. Four 30 µL cc DiD-EV-loaded degradable patches were prepared as described in section 2.2.4 and placed in four coated wells containing 270 µL PBS-antimicrobials. A volume of 300 µL 10% (v/v) cc DiD-EV-loaded degradable microgel suspension was placed in the four other wells. Images were taken using an inverted microscope (Olympus, 4X objective lens). Then, 0.05% trypsin-EDTA was added to each well and the plate was incubated at RT for 15 min in the dark. Wells were observed under a microscope to check for complete hydrogel degradation. Cell media containing 10% (v/v) FBS was added to each well at a ratio 1:1 to inhibit the trypsin. Images of each wells were taken using an inverted microscope (Olympus, 4X objective lens). The degradation products were then analysed by FCS using methods described in section 2.2.2. Finally, degradation products were tested using the EV uptake assay described in section 2.2.3.

2.2.6. *In vivo* experiments

All animal procedures were carried out in accordance with the UK Home Office Animals (Scientific Procedures) Act 1986 and Directive 2010/63/EU of the European Parliament on the protection of animals used for scientific purposes. *In vivo* experiments were performed in collaboration with Dr. Daniel Stuckey (University College London). BALB-c mice were ordered from Charles River Laboratories and left to acclimatise for at least 1 week before the injections were performed. Anaesthesia was induced with 5% isoflurane (Zoatis) and surgical anaesthesia was confirmed by the loss of standing and pedal reflexes. The hairs were removed from their lower back using clippers (Harvard Apparatus). Isoflurane was reduced and maintained at 2% during the whole procedure. Animals were imaged at 640/680 nm before treatment administration using an IVIS® Spectrum fluorescence imaging system for small animals (PerkinElmer) and background fluorescence levels were used to normalise post-injection measurements. Treatments were injected using a 0.5 mL 29G

MicroFine™+ Insulin syringe (BD) and each animal received two 200 µL subcutaneous injections on either side of their lower back. Images were acquired immediately, 10 min, 30 min, 1 h, 4 h, 2 d, 4 d and 8 d after injection.

For the first experiment, treatments consisted of three dosages of cc DiD-EVs (10^9, 10^{10} and 10^{11}) prepared using a dilution series and were compared to a PBS-antimicrobials control (n = 1 per condition). For the second experiment, an injection of 10^{10} cc DiD-EVs suspended in 200 µL PBS-antimicrobials was compared to an injection of 200 µL 10% (v/v) degradable microgels loaded with 5×10^{11} EV/mL hydrogel (equivalent to 10^{10} EVs total in theory, n = 2-3 per condition).

2.2.7. Statistical analysis

Data are presented as median ± interquartile range unless stated otherwise. NTA results were analysed using a Kruskal-Wallis test with Dunn's correction. FCS experiments comparing multiple groups were analysed using a Kruskal-Wallis test with Dunn's correction. FCS experiments comparing two conditions were analysed using two-tailed Mann-Whitney test.

3. Results and discussion

3.1. DiD-EV preparation and characterisation

3.1.1. EV characterisation

EVs were isolated and purified from the conditioned media of floating HEK cells, concentrated by UF and purified by SEC.

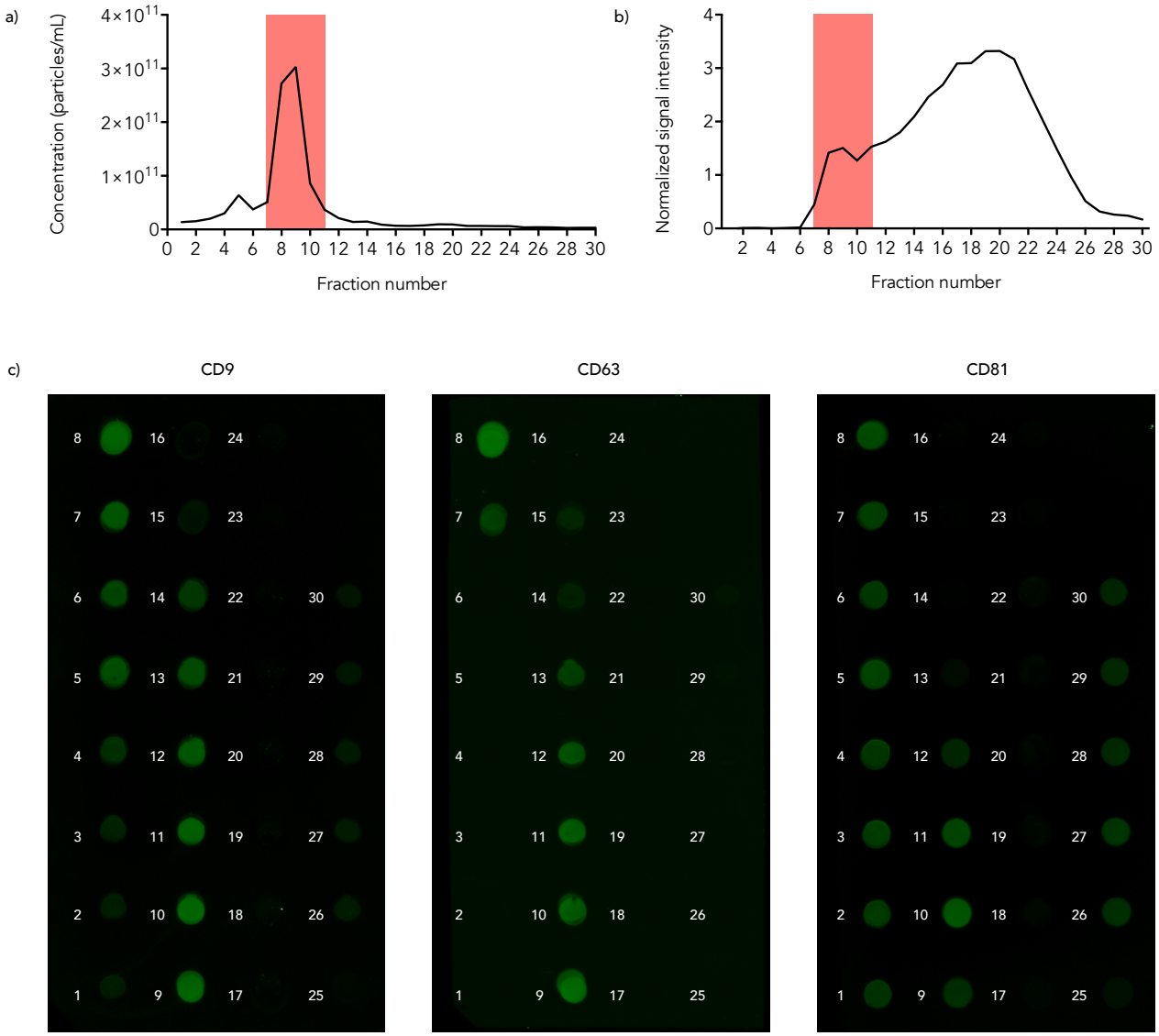


Figure 36: Characterisation of the fractions obtained following SEC of the HEK cell-derived conditioned media using a) NTA analysis, b) MicroBCA assay and c) dot blotting against EV-specific markers CD9, CD63 and CD81. Fractions 7-11 were selected for their high EV concentration.

The 30 fractions collected from this last step were analysed by NTA, a MicroBCA assay and dot blotting to identify the fractions containing the largest amounts of EVs with minimal contamination from soluble proteins (Figure 36). As indicated by the results of the NTA analysis, fractions 7 and 11 contained the largest amounts of nanosized particles (Figure 36.a). Although these fractions also contained a small amount of protein, most of the protein content of the concentrated conditioned media was eluted in later fractions (Figure 36.b). As shown in Figure 36.c, fractions 7-11 were also found to contain the highest amount of the three main EV-specific surface markers, CD9, CD63 and CD81.

3.1.2. DiD-EV labelling

Fractions 7-11 were pooled and labelled with DiD, a commercially available lipophilic carbocyanine dye used as fluorescent cell tracer. Methods used to label the EV suspension were optimised in the following section, with the aim of maximising labelling and minimising the risk of DiD micelle formation. FCS was used to measure labelling, which was expressed as counts per particle (CPP), and particle hydrodynamic diameter (Dh).

In a first experiment, the DiD concentration was set to 5 µM and the effects of the working volume (V, 500 or 1000 µL) and mixing rate used during the incubation period (ω, 300 or 1000 rpm) were evaluated. As shown in Figure 37.a, there was no significant difference in the Dh between the four samples. However, the CPP was significantly reduced when using a larger working volume (1000 µL) in combination with a higher mixing rate (1000 rpm) compared to using a smaller working volume (500 µL) with a lower mixing speed (300 rpm) ($p = 0.0461$). The combination V = 500 µL and ω = 300 rpm was thus selected for the next experiments.

In a second experiment, the DiD concentration was decreased by a factor of 10 to assess whether the heterogeneity in labelling could be reduced. As shown in Figure 37.b, reducing the dye concentration from 5 µM to 0.5 µM resulted in no change in Dh and a significant

reduction in CPP ($p < 0.0001$) without majorly affecting the interquartile range of the CPP. The highest concentration (5 µM) was therefore kept for the following experiments.

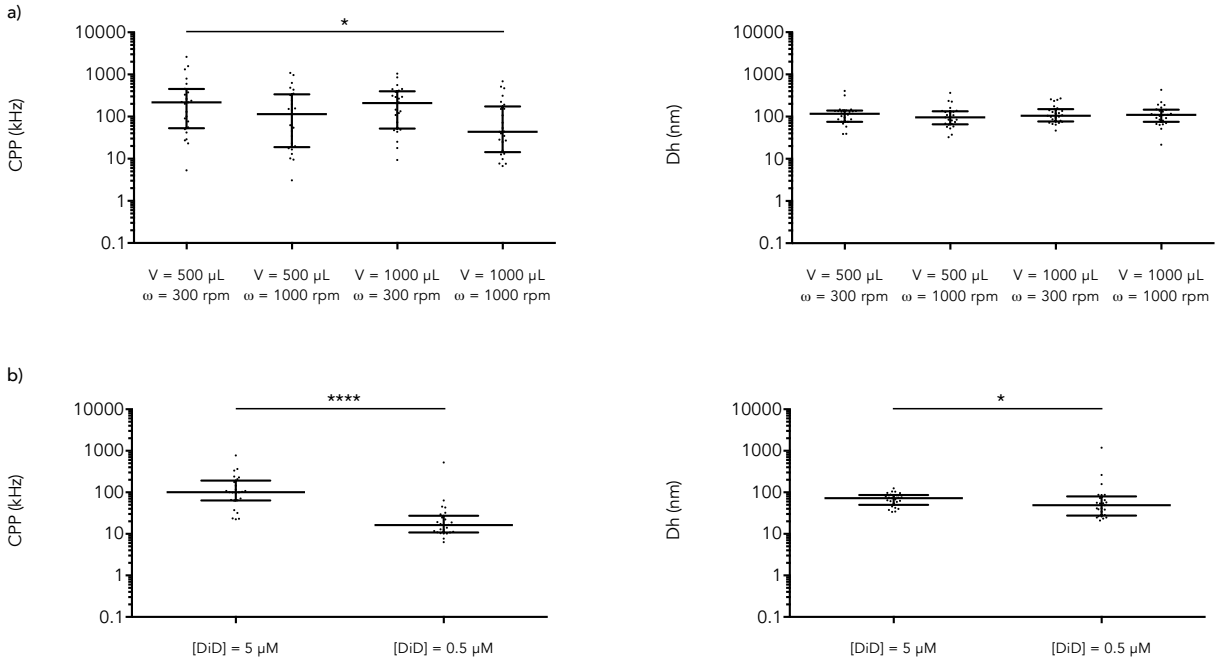


Figure 37: Evaluation of the effects of different parameters on the EV labelling (CPP, left) and hydrodynamic diameter (Dh, right) using FCS analysis. a) Optimisation of the working volume (V) and mixing rate (ω) (Kruskal-Wallis test with Dunn's correction, * $p = 0.0461$). b) Optimisation of the DiD concentration (two-tailed Mann-Whitney test, **** $p < 0.0001$, * $p : 0.0340$).

The newly optimised protocol was used to prepare a batch of DiD-labelled EVs, which was then concentrated into a smaller volume (cc DiD-EVs) using UF to enable the fabrication of microgels loaded with high amounts of EVs. A control DiD sample was also prepared using PBS-antimicrobials in place of the EV suspension and was concentrated (cc DiD) using the same protocol. NTA was used to measure the Dh and concentration of all nanoparticles present in the samples (Figure 38.a), while FCS was used to measure the Dh and CPP of fluorescent particles only (Figure 38.b). Importantly, no particles were found in the DiD and cc DiD control samples, which suggested that under these conditions, DiD had not formed nano-sized particles. As shown in Figure 38, no significant difference in Dh was observed between all three samples when measured with NTA, while FCS measurements revealed a significant difference between the DiD-EVs and cc DiD-EVs samples ($p = 0.0040$). Such differences in measurement outcomes could be attributed to the fact that NTA and FCS do

not use the same principle to measure particles [245]. According to NTA measurements, particles, particle concentration was increased in the cc DiD-EVs compared the EVs and DiD-EVs, which demonstrated that the UF was efficient at concentrating the sample. Finally, labelling was found to be significantly reduced (p = 0.0090), yet less heterogeneous, for the cc DiD-EVs compared to the DiD-EVs. This difference was however considered to be unimportant since cc DiD-EVs were still showing a considerable level of fluorescence and EV concentration was an essential step to enable the fabrication of microgels loaded with high amounts of EVs.

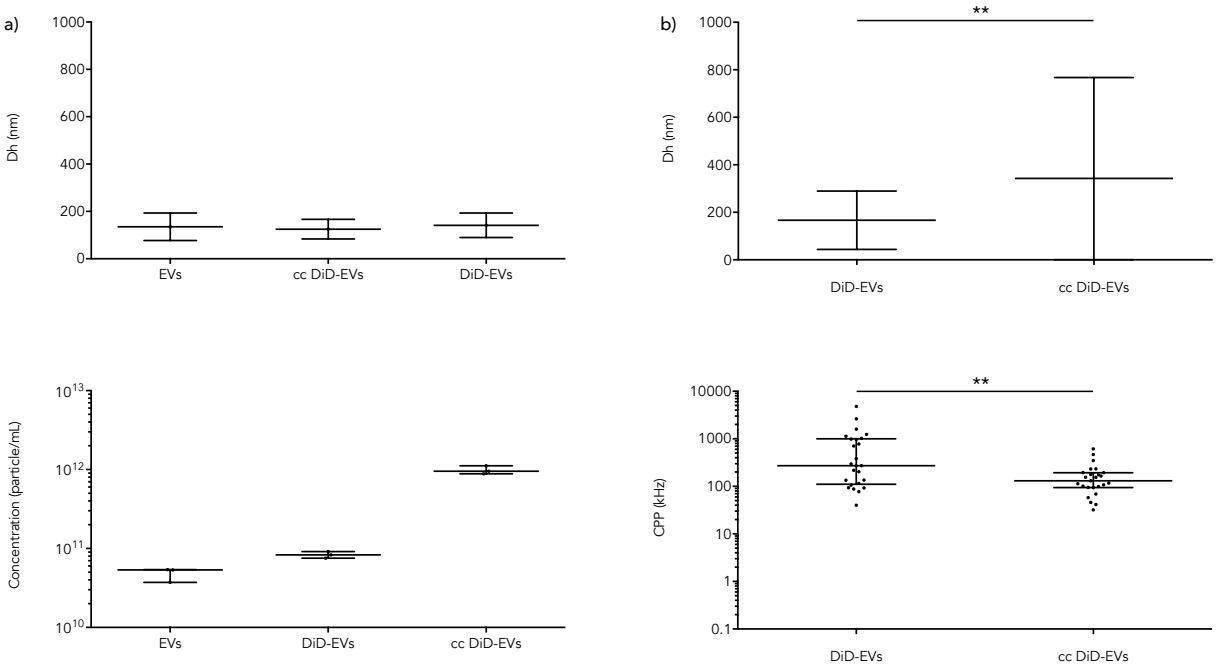


Figure 38 : Evaluation of the effects of EV labelling and UF-based concentration on particle hydrodynamic diameter (Dh, data presented as mean ± SD), particle concentration and labelling levels (CPP) using a) NTA (Kruskal-Wallis test with Dunn's correction) and b) FCS analysis (two-tailed Mann-Whitney test, for Dh ** p = 0.0040, for CPP ** p = 0.0090).

3.1.3. DiD-labelled EV uptake

As discussed in Chapter 1, EVs play a major role in intercellular communication, which relies on their ability to bind and being internalised by recipient cells *via* mechanisms that are dependant on the integrity of their lipid membrane and surface receptors. In this section, an *in vitro* EV uptake assay was developed to evaluate the impact of the different steps

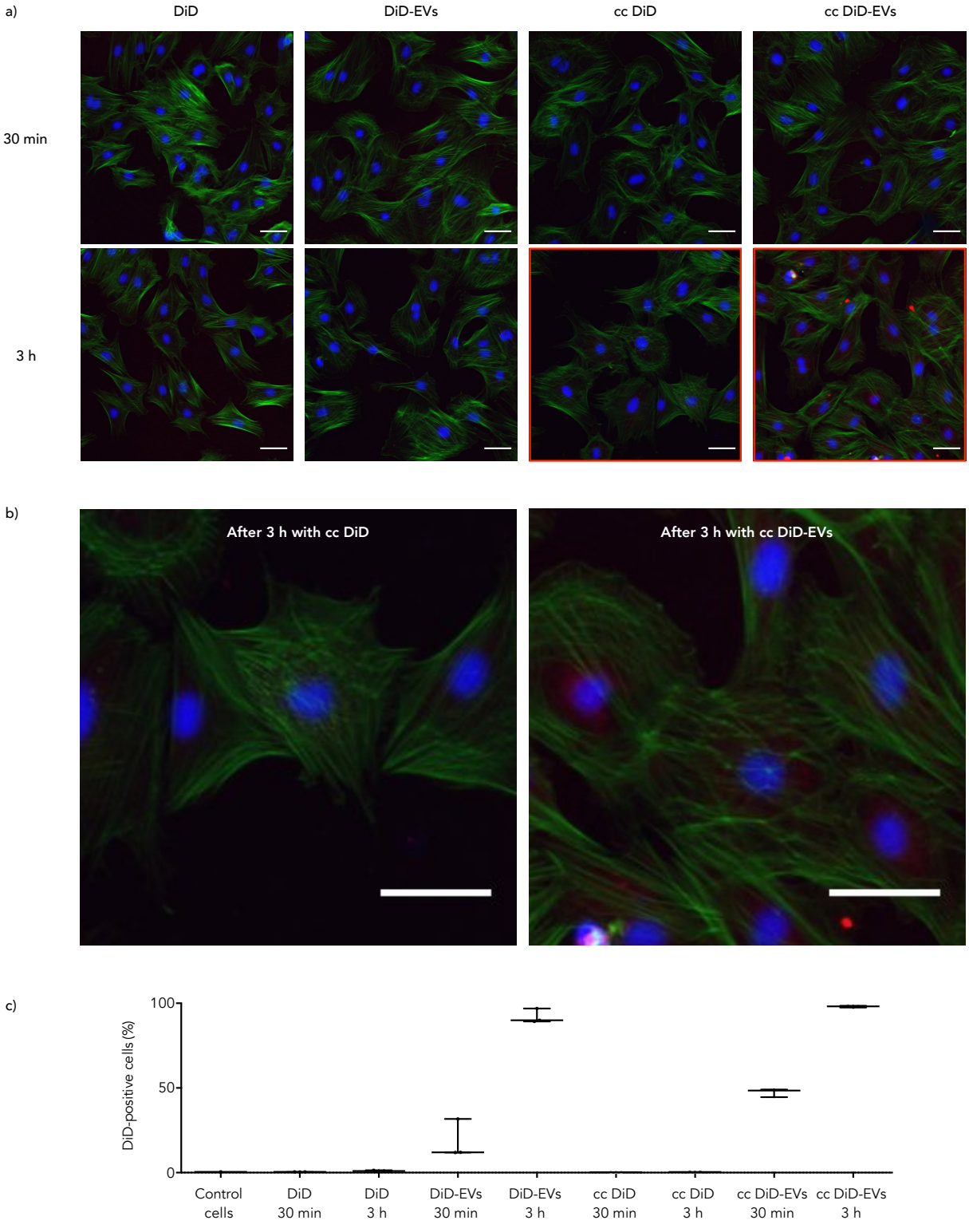


Figure 39: DiD-EV uptake by neonatal rat cardiac fibroblasts in culture. a) Confocal images (scale bar = 50 µm). The F-actin cytoskeleton was labelled with phalloidin (green) and the nuclei were stained with DAPI (blue). The presence of a red halo around the nuclei of cells treated with cc DiD-EVs for 3 hours indicated that the EVs were efficiently uptaken. b) Close up pictures of the cells treated with cc DiD and cc DiD-EV for 3 hours. c) Quantification of the DiD-positive cells using flow cytometry.

involved in EV loading and release from microgels on their capacity to be internalised by cells in culture. Neonatal rat cardiac fibroblasts were exposed to the DiD-labelled EVs (DiD-EVs and cc DiD-EVs) and DiD controls (DiD and cc DiD) prepared in section 3.1.2.

Uptake was evaluated after a 30 min or 3 h incubation using flow cytometry and confocal fluorescence imaging. As shown in Figure 39.b, flow cytometry analysis revealed that only a small number of cells became DiD-positive following exposure to DiD or cc DiD (<2%), while high uptake rates were observed when treating the cells with DiD-EVs and cc DiD-EVs. More specifically, 19% and 92% DiD-positive cells were found in conditions treated with DiD-EVs for 30 min and 3 h, respectively. Similarly, when treated with the same amount of cc DiD-EVs, approximately 47% and 98% cells were DiD-positive after 30 min and 3 h exposure, respectively.

These results indicated that, under these experimental conditions, DiD was able to effectively label cells only when carried by EVs. Confocal fluorescence microscopy images of all eight conditions are provided in Figure 39.a. Among all conditions, only the cells treated with 10^{10} cc DiD-EVs for 3 h demonstrated a very obvious red labelling. This labelling appeared to be located around the nuclei, which indicated that the DiD-labelled EVs had been internalised.

3.2. DiD-EV loading into microgels

3.2.1. EV loading capacity

Rheological measurements were performed on hydrogels unloaded or loaded with 5×10^{11} EV/mL. As seen in Figure 40, hydrogels could efficiently be crosslinked when loaded with this concentration of EVs. For both degradable and non-degradable formulations, EV-loaded hydrogels seemed to present slightly faster crosslinking kinetics and higher elastic modulus G' compared to unloaded hydrogels. However, this would need to be confirmed

with additional measurements and longer timepoints in order to establish whether is effect is significant.

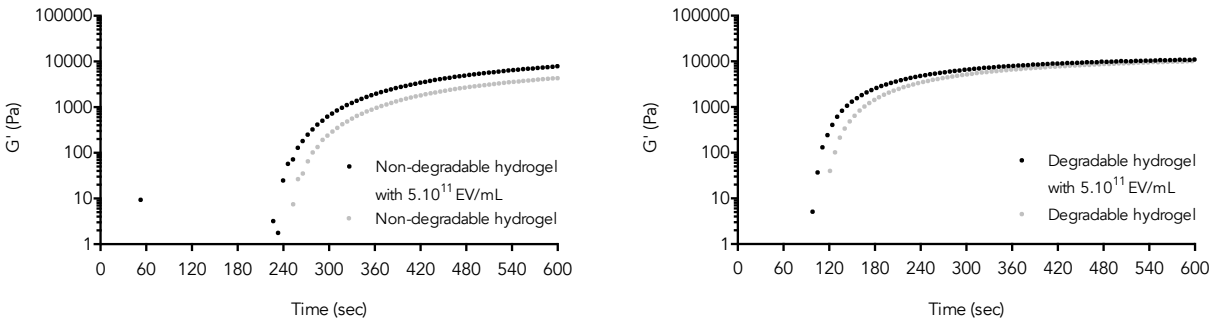


Figure 40: Time sweep performed on crosslinking unloaded hydrogels (grey) and hydrogels loaded with 5 x 10^{11} EV/mL, prepared using the non-degradable PEG dithiol crosslinker (left) or MMP-2/9-sensitive peptide crosslinker (right).

3.2.2. EV-loading into microgels

EV-loaded microgels were then fabricated using this same concentration of cc DiD-EVs. Some particles could be observed in the channel containing the PEG precursor solution containing the EVs, which seemed to result in disturbances at the droplet generation junction and the formation of slightly less monodisperse microdroplets.

The fabrication of EV-loaded microgels using the microfluidic platform, and the non-degradable or degradable peptide crosslinker was successful. Loaded microgels were imaged using a confocal fluorescence microscope (Figure 41). EV-loaded non-degradable patches and unloaded microgels were prepared and used as controls. As shown in Figure 41, EVs were efficiently loaded into the microgels, as suggested by the presence of fluorescent particles in the microgels, with a similar distribution to the EV-loaded patch. These findings suggested that the microgel fabrication did not appear to change the loading efficiency of the EVs into the gel network compared to the hydrogel patch. However, in both cases, the size of the particles suggested that the EVs had aggregated to form micro-sized aggregates. Moreover, in the non-degradable EV-loaded microgels, the EV aggregates appeared to be more concentrated in the middle of the microgels. This could be due to the slight differences in crosslinking kinetics between the two formulations.

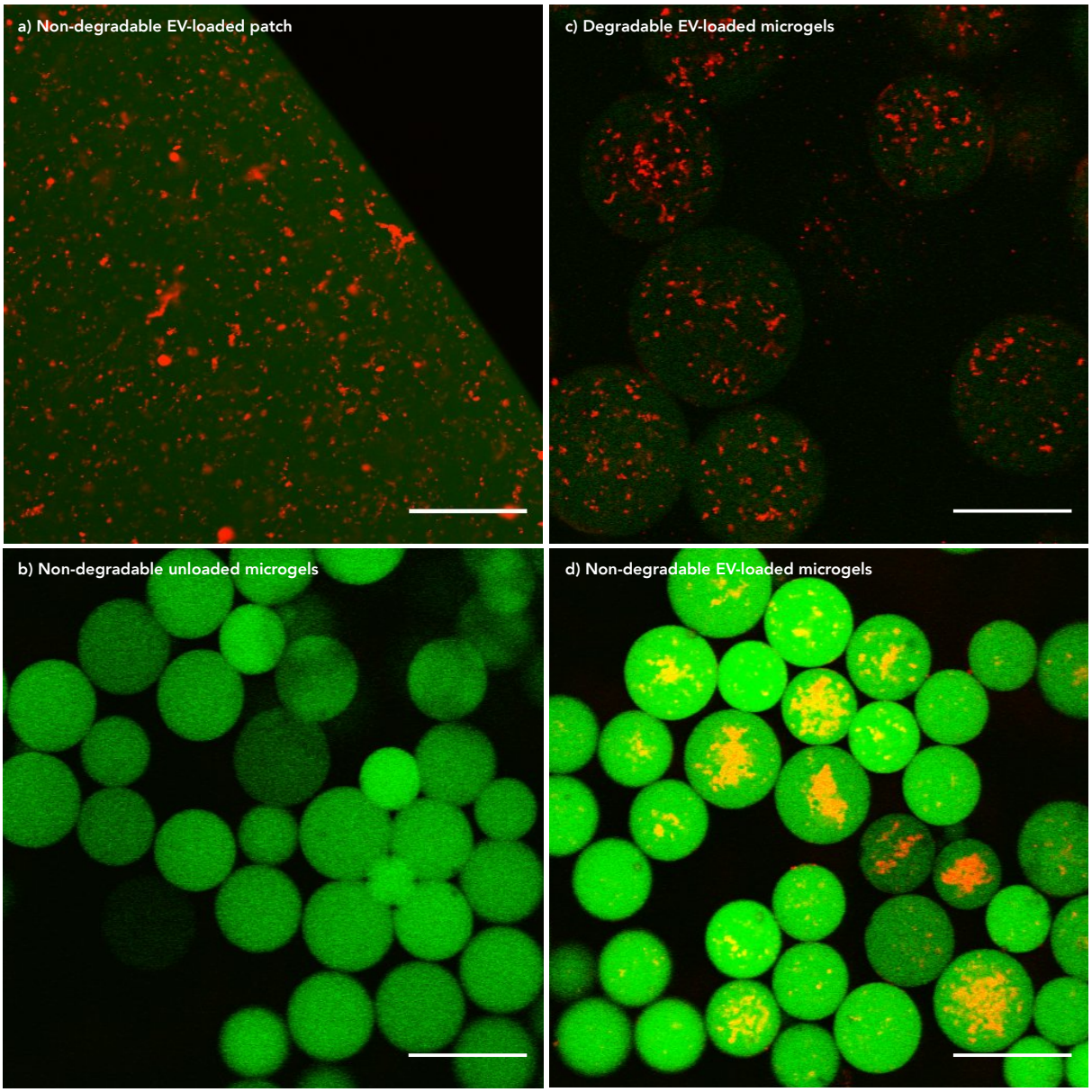


Figure 41: Confocal images of a non-degradable EV-loaded hydrogel patch (a), non-degradable unloaded microgels (b), degradable EV-loaded microgels (c) and non-degradable EV-loaded microgels (d). EVs are labelled with DiD (red) and gels are labelled with AlexaFluor™ 488 (green). All EV-loaded gels were loaded with 5 x 10^{11} EV/mL (scale bar = 100 µm).

Compared to the non-degradable microgels, the degradable EV-loaded microgels also looked more swollen and less fluorescent than the non-degradable microgels. This is likely due to the degradable microgels starting to degrade between the time they were prepared and imaged (10 days). In addition, EVs were not purified in aseptic conditions, meaning that loading EVs into the microgels constitutes another potential source for contamination by microbial proteases. Additional experiments are needed to properly characterise the EV-

loaded microgel size and stability and refine fabrication methods to implement sterilisation steps or aseptic procedures. These preliminary results, however, demonstrated that DiD-labelling can be used to track EVs during their encapsulation into hydrogels using confocal fluorescence microscopy.

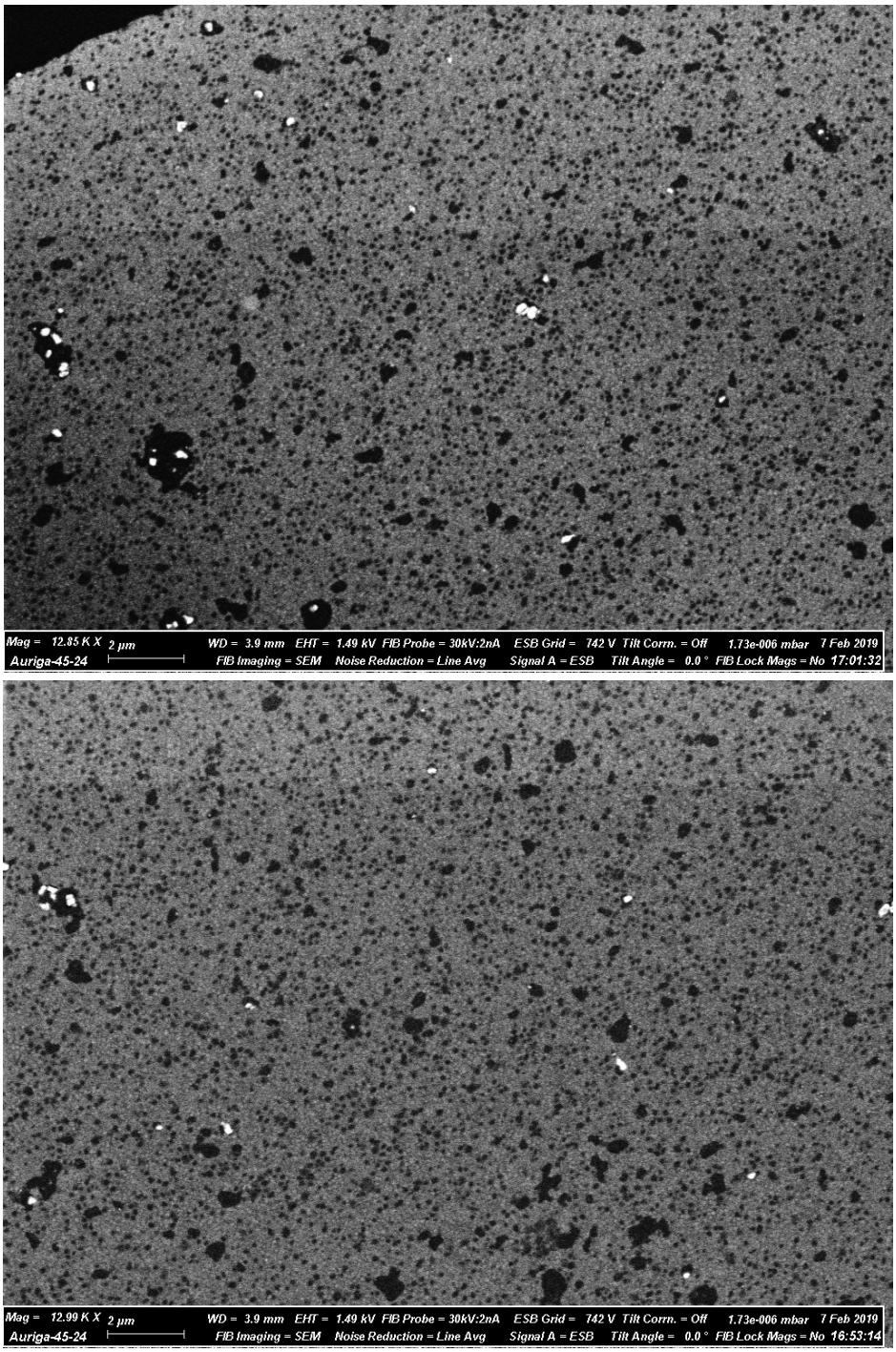


Figure 42: FIB-SEM images of non-degradable EV-loaded microgels. EVs were labelled using 0.5% osmium tetroxide (white). The contrast between the sample and background was enhanced using uranyl acetate, which made the pores appear in black (scale bar = 2 µm).

Non-degradable EV-loaded microgels were also imaged using FIB-SEM (Figure 42). Samples were prepared by HPF-FS to better preserve the microgel structure. As shown in Figure 42, microgels could be successfully imaged using this protocol. The pores of the hydrogel were visible (in black, approximate size 150 nm). Importantly, lipid nanoparticles and aggregates of nanoparticles (in white) were found in the pores throughout the whole sample. Although imaging of unloaded microgel would be necessary to unquestionably exclude the possibility of an artefact, these lipid aggregates are most likely to be EVs. These findings, which were consistent with the results of confocal fluorescence imaging, provided further evidence that EVs can successfully be loaded into microgels.

3.2.3. EV release and uptake

EV-loaded patches and microgels were degraded using trypsin 0.05% for 15 min at RT followed by addition of media containing 10% (v/v) FBS to inhibit the remaining enzyme. Figure 43 provides images of the patches and microgels before and after degradation.

Degradation products were analysed by FCS and compared to three EV controls: cc DiD-EVs (from the suspension used to prepare the patches and microgels), cc DiD-EVs treated with trypsin followed by media ("trypsin-treated cc DiD-EV"), and cc DiD-EVs treated media containing 10% (v/v) FBS only ("media-treated cc DiD-EV"). As shown in Figure 44 (left), fluorescent nanoparticles could be detected in all three EV samples. Their hydrodynamic diameter (Dh, $p = 0.0002$) and labelling (CPP, $p < 0.0001$) was found to be significantly reduced in trypsin-treated cc DiD EVs compared to cc DiD-EVs. However, no difference was found between trypsin-treated cc DiD-EVs and media-treated cc DiD-EVs, which suggested that these changes in particle size and fluorescence could not be attributed to trypsin itself and that the trypsin-based protocol could safely be used to degrade EV-loaded hydrogels.

Degradation products obtained from the four EV-loaded patches were compared to the products released from the degradation of the four microgel suspension samples. Fluorescent nanosized particles could be detected in all eight samples. EVs released from microgels were significantly bigger ($p = 0.0028$) and brighter ($p = 0.0016$) than EVs released

from the patches, while particle concentration remained constant. This could be due to the formation of small EV aggregates during the microgel fabrication process, which would be consistent with the observations made in section 3.2.2. Although results cannot be directly compared due to differences in sample size, the particle concentration was found to be similar in trypsin-treated cc DiD-EVs and patches degradation products, but higher in microgel degradation products. These results could be explained by the fact that dose matching was attempted based on the theoretical amount of EVs loaded in the microgels during their fabrication. However, inaccuracies accumulating along the EV loading process may have resulted in higher EV loading into the microgels.

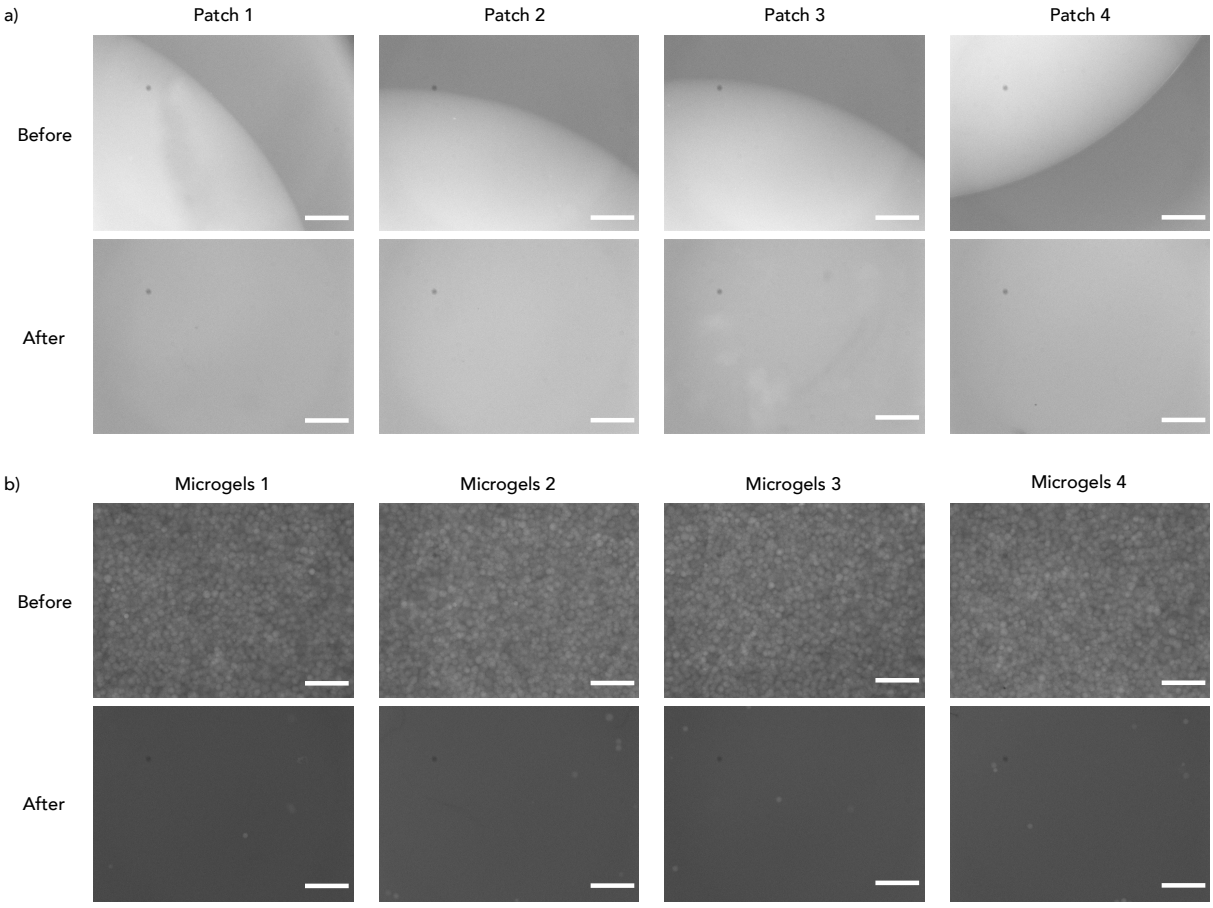


Figure 43: Images of peptide-crosslinked a) hydrogels and b) microgels loaded with 5 x 10^{11} EV/mL before and after trypsin-mediated degradation (scale bar = 500 µm). In all conditions, the hydrogels were successfully degraded after the 15 min treatment with trypsin 0.05% at RT.

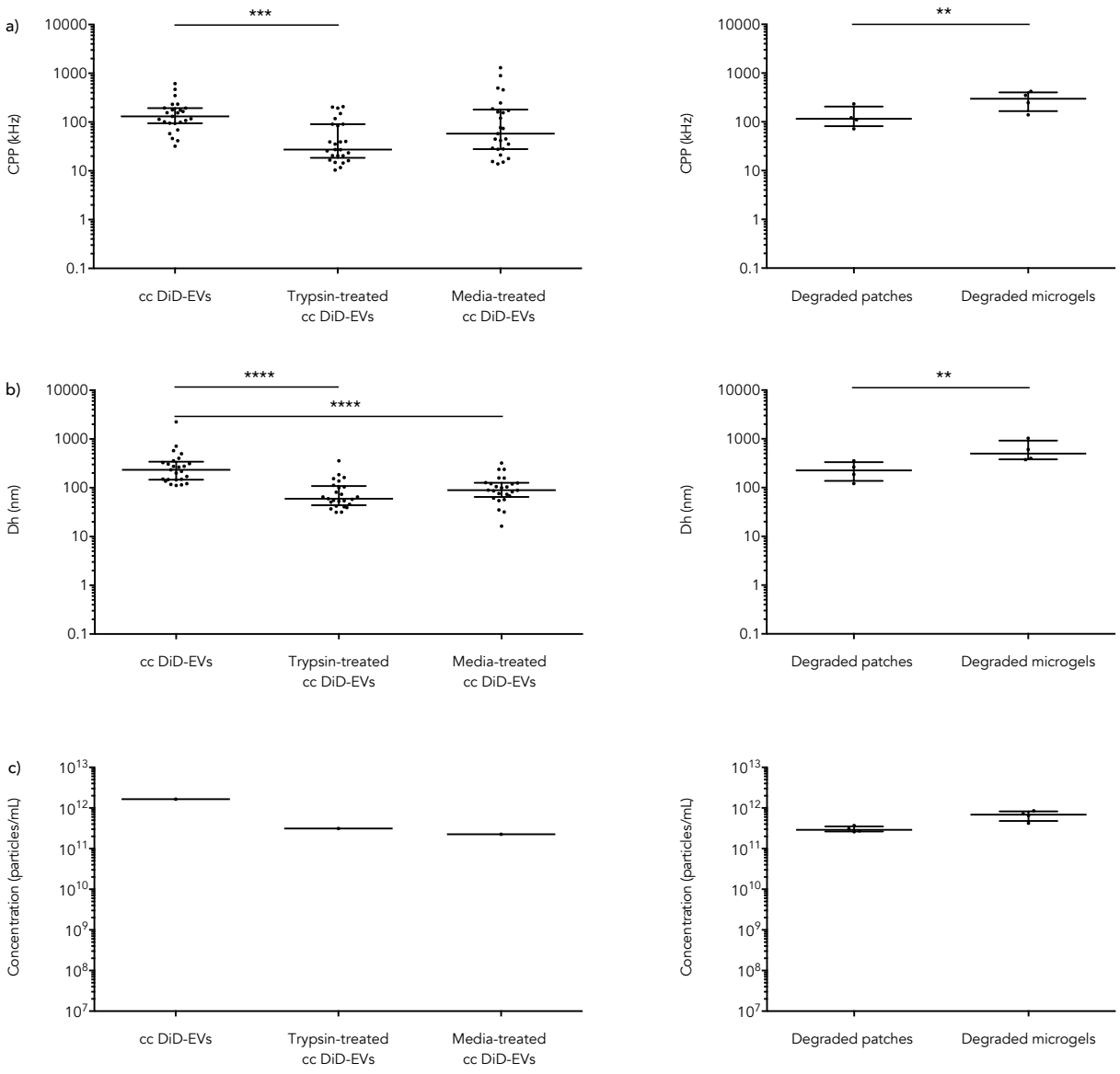


Figure 44: Analysis of the degradation products obtained from cc DiD-EV-loaded patches and microgels. The labelling (CPP, a), hydrodynamic diameter (Dh, b) and concentration (c) of the cc DiD-EVs treated with tryspin or media as well the nanoparticles released from the degraded patches and microgels were analysed by FCS. EV data (a-c, left) were analysed with a Kruskal-Wallis test with Dunn's correction (for CPP: *** $p = 0.0002$; for Dh: **** $p < 0.0001$). Degradation products data (a-c, right) were analysed with a two-tailed Mann-Whitney test (for CPP: ** $p = 0.0016$; for Dh: ** $p = 0.0028$).

The patches and microgel degradation products were then evaluated using the EV uptake assay developed in section 3.1.3. Neonatal rat cardiac fibroblasts were exposed to the released products for 3 h and analysed by flow cytometry and confocal fluorescence imaging (Figure 45). No DiD labelling could be observed in the cells treated with the degradation products using confocal fluorescence microscopy. However, DiD-positive cells were detected during the flow cytometry analysis. More

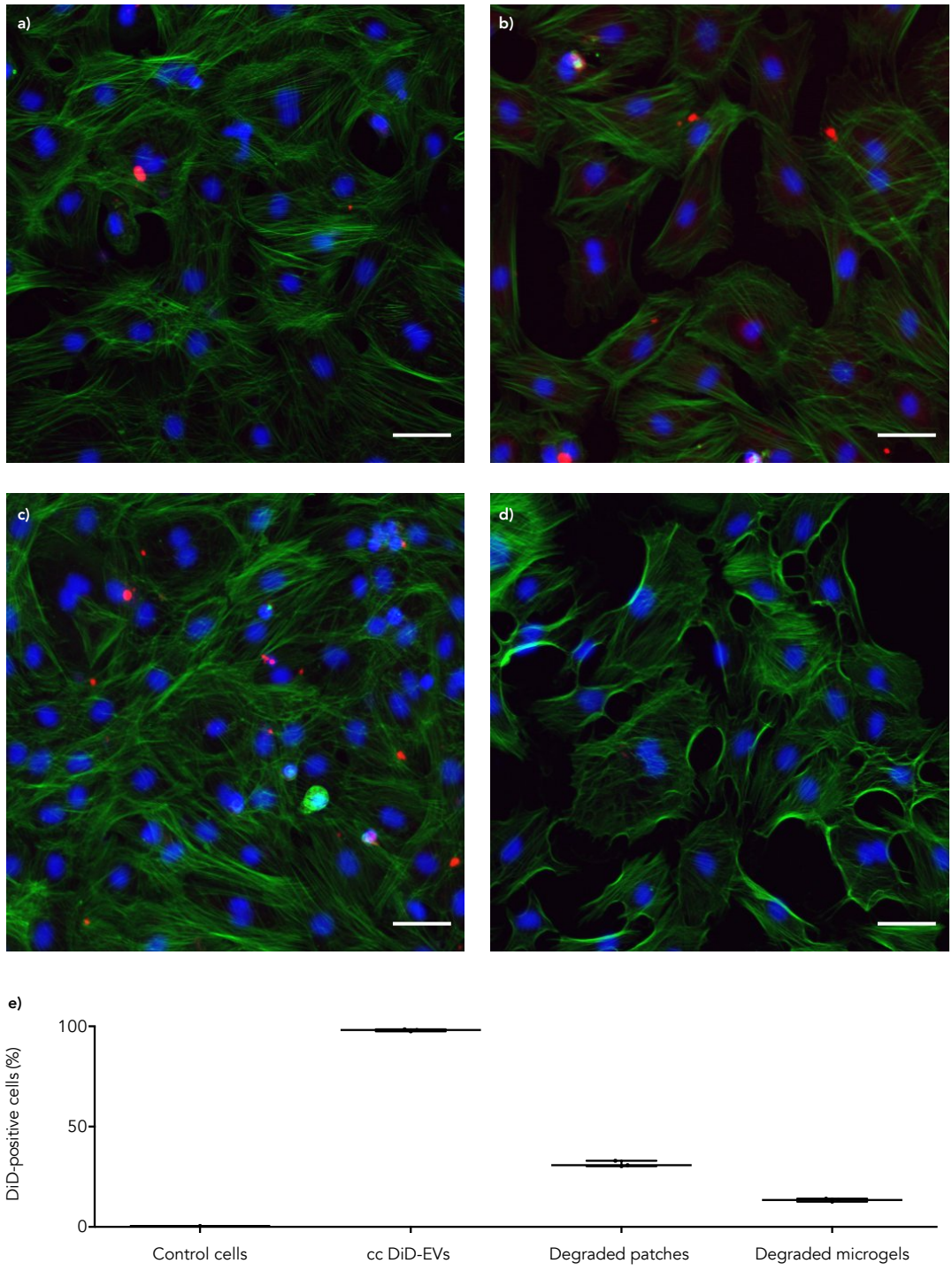


Figure 45: Evaluation of the degradation products obtained from cc DiD-EV-loaded hydrogels and microgels using the EV uptake assay. Confocal images were taken after incubation for 3 h with a) media only, b) 10^{10} cc DiD-EVs, or the degradation products obtained from cc-DiD-EV-loaded c) patch or d) microgels (scale bar = 50 µm). The F-actin cytoskeleton was labelled with phalloidin (green) and the nuclei were stained with DAPI (blue). The presence of a red halo around the nuclei of cells treated with cc DiD-EVs for 3 hours indicated that the EVs were efficiently uptaken. No signal was found in the cells treated with degraded pacthes and microgels. e) Quantification of the DiD-positive cells using flow cytometry. Approximately 98%, 31% and 13% cells were found to be DiD-positive in the cc DiD-EV, degraded patch and degraded microgel-treated cells, respectively.

specifically, approximately 31% and 13% cells were found to be DiD-positive when treated with the degraded patches and degraded EV-loaded microgels, respectively. These results indicate that EVs partially retained their capacity to be uptaken by cells throughout the microgel fabrication and degradation processes. Although uptake levels were reduced for EVs released from degradable microgels, such findings suggest that EVs can be encapsulated into degradable microgels using the methods developed in the previous chapters without preventing the cell-binding capacity of EVs.

3.2.4. DiD-labelled EV detection *in vivo*

Preliminary *in vivo* experiments were performed to investigate the possibility of detecting and tracking DiD-labelled EVs. The ability to detect fluorescence *in vivo* mainly depends on two factors: the fluorophore emission wavelength and the depth from which the signal is emitted. Therefore, a subcutaneous injection model was chosen in order to maximise the probability of detecting the DiD-labelled EVs.

In a first *in vivo* experiment, three different dosages (10^9, 10^{10} and 10^{11}) of cc DiD-EVs as well as a PBS-antimicrobials control were injected subcutaneously in the back of two mice. A fluorescence image of the four syringes containing the treatments is provided in Figure 46.a. No background fluorescence was observed in the control syringe (PBS-antimicrobials), whereas signal could be detected in all of three other syringes. Mice were imaged before injection and post-injection and measurements were normalised to those values. Mice were imaged immediately, 10 min, 30 min, 1 h and 4 h after injection on day 0, as well as on day 2, 4 and 8. As seen in Figure 46.b and 46.c, EVs were detected over 8 days post injection in all concentrations, validating the DiD detection method in an *in vivo* setting.

The average radiance efficiency was first detected in the area injected with 10^{11} EV. However, signal intensity increased in the hours following injection and all dosages became detectable from the 4 h timepoint. This progressive increase could be explained by the fact that EVs were suspended in a relatively large volume of liquid (200 µL). When injected, this formed a liquid pocket under the skin (as seen when comparing the camera images

obtained before and immediately after injection). This could lead to the attenuation of the signal emitted by the fluorescent EVs located deeper in the liquid pocket, closer to the muscle. As the liquid diffuses out of this tissue region, the EVs were progressively concentrated and/or uptaken by the surrounding tissues (*e.g.* muscle, skin). The average radiance efficiency reached a peak at day 2 before starting to slowly decrease. Importantly, signal could still be detected for all three dosages up to d 8, which is very likely to be due to the EVs being uptaken by resident cells.

3.2.5. *In vivo* evaluation of EV retention using microgels

In a second study, the administration of 10^{10} cc DiD-EVs in suspension was compared to the injection of cc DiD-EV-loaded degradable microgel suspension (10% (v/v)), which theoretically contained the same amount of EVs. However, as seen in Figure 47.a, higher fluorescent signal was detected in syringes containing the EV-loaded microgels, which indicated that dose matching was not successful. This could be due inaccuracies that accumulated along the EV loading process.

Nevertheless, three mice were treated with the EVs on one side of their back and EV-loaded microgels on the other side and imaged for 8 d (Figure 47.b and c). The signal emitted by the EVs was detectable at 30 min after injection, reached a peak on day 2 and then slowly decreased, which was consistent with the results found in the previous experiment. A strong signal was detected from the side injected with the EV-loaded microgels immediately after injection, which could partially be explained by the fact that the amount of EV loaded into the microgels had been underestimated. However, although images cannot be directly compared between experiments in the case of *in vivo* fluorescence imaging, this signal appeared to be much brighter than the signal detected from the highest dosage of EVs used in the previous experiment. These observations suggest that there may be other factors playing a role in signal intensity than inaccuracies during microgel fabrication and loading. The signal intensity increased to reach a peak at day 2, which, similarly to non-encapsulated EVs, could be due to the solvent diffusing out of the tissue and leaving only the 10% volume occupied by the microgels. Interestingly, the fluorescence remained

constant between day 2 and day 8, which may be due to the retained presence of microgels in the tissue and the progressive release of DiD-EVs being uptaken by the surrounding cells. These promising results provided preliminary evidence that DiD-labelled EVs could be detected *in vivo* when injected subcutaneously. More specifically, dosages as low as 10^9 cc DiD-EVs, prepared using the labelling protocol described in section 3.1.2, could be tracked for at least 8 d. DiD-EV-loaded microgels could also be detected and signal intensity was found to be constant in the days following the delivery. This suggested that the degradable microgels may be slowly releasing the DiD-EVs over time, thus providing a platform for sustained EV delivery. Additional experiments are needed to confirm these observations and determine the fate of the DiD-EVs once delivered. Histological analysis could be used to determine whether the microgels have degraded and whether the DiD-EVs are uptaken by the surrounding cells. These results also suggest that, since the signal intensity was so high when DiD-EVs were injected subcutaneously, it may be possible to move to a more relevant animal model such as an intramuscular injection in the thigh.

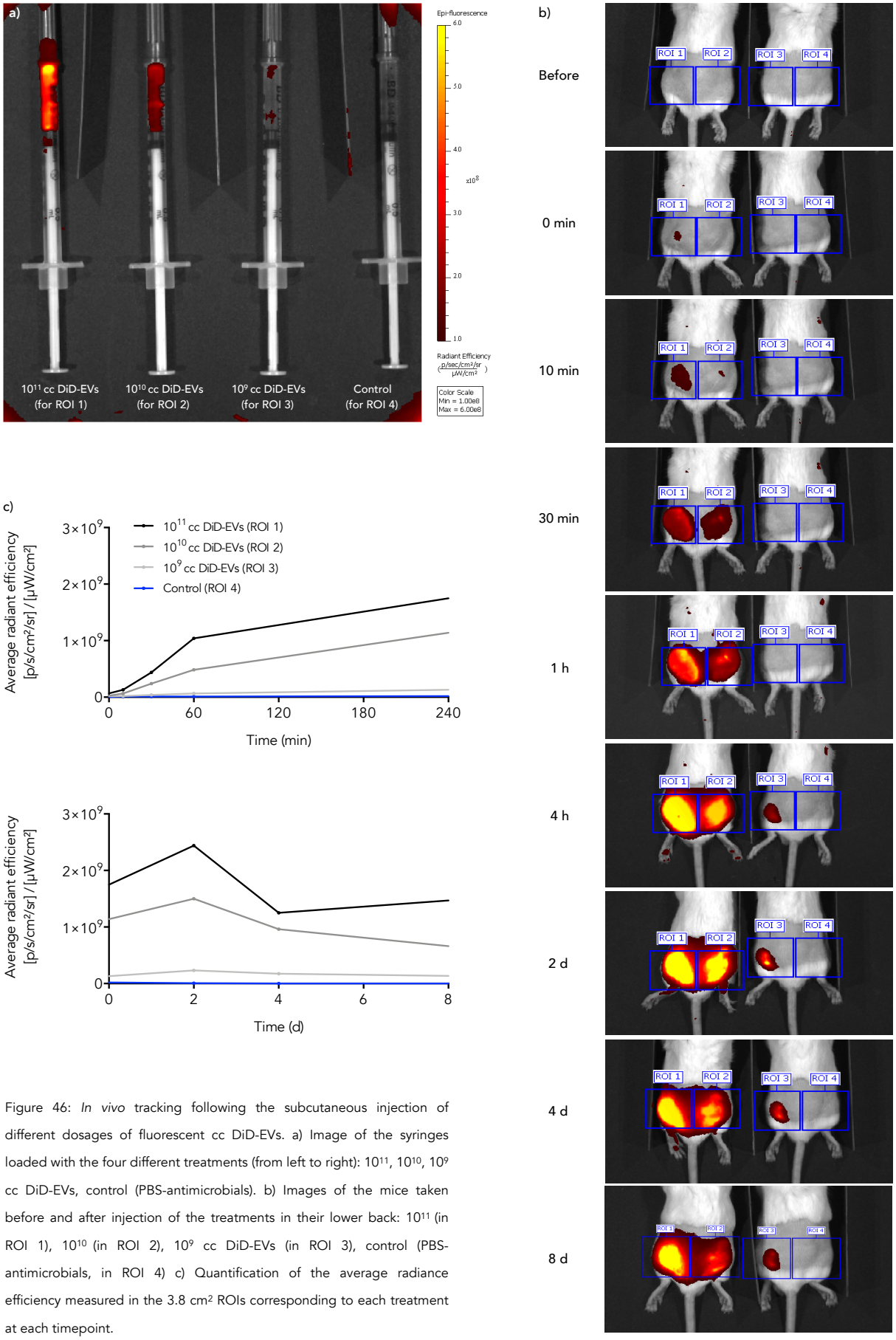


Figure 46: *In vivo* tracking following the subcutaneous injection of different dosages of fluorescent cc DiD-EVs. a) Image of the syringes loaded with the four different treatments (from left to right): 10^{11}, 10^{10}, 10^{9} cc DiD-EVs, control (PBS-antimicrobials). b) Images of the mice taken before and after injection of the treatments in their lower back: 10^{11} (in ROI 1), 10^{10} (in ROI 2), 10^{9} cc DiD-EVs (in ROI 3), control (PBS-antimicrobials, in ROI 4) c) Quantification of the average radiance efficiency measured in the 3.8 cm^2 ROIs corresponding to each treatment at each timepoint.

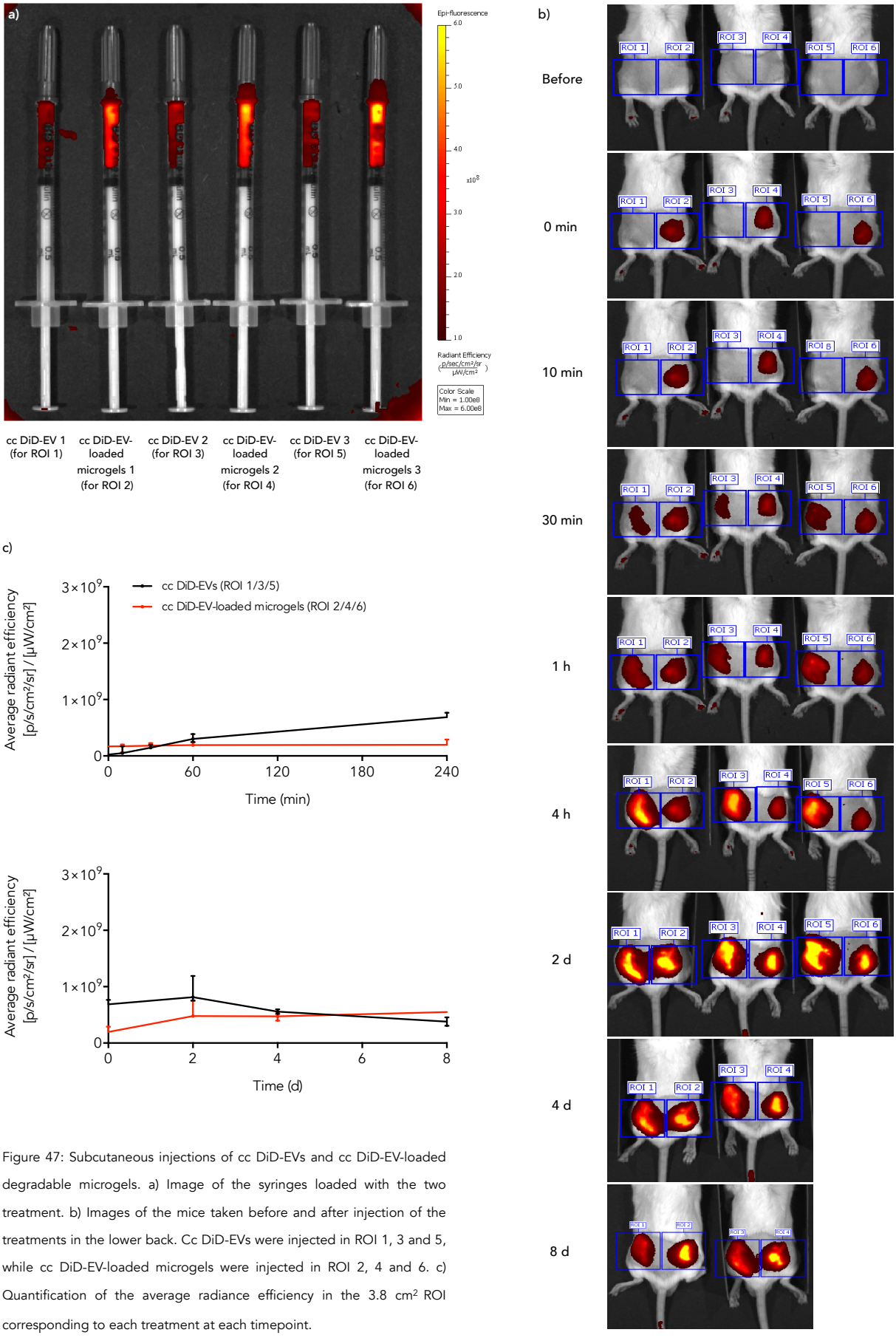


Figure 47: Subcutaneous injections of cc DiD-EVs and cc DiD-EV-loaded degradable microgels. a) Image of the syringes loaded with the two treatment. b) Images of the mice taken before and after injection of the treatments in the lower back. Cc DiD-EVs were injected in ROI 1, 3 and 5, while cc DiD-EV-loaded microgels were injected in ROI 2, 4 and 6. c) Quantification of the average radiance efficiency in the 3.8 cm^2 ROI corresponding to each treatment at each timepoint.

4. Conclusion

In this chapter, EVs were produced from HEK cells in culture, purified by UF and SEC, and characterised with NTA, dot blotting and a MicroBCA assay. A method for labelling the EVs with DiD, a fluorescent lipophilic dye, was developed. The capacity to form hydrogels in the presence of a high concentration of EVs (5 x 10^{11} EV/mL) was investigated using rheology and revealed successful hydrogel crosslinking, as well similar crosslinking kinetics and biomechanical properties between unloaded and EV-loaded hydrogels. The fabrication of EV-loaded microgels was shown to be feasible, and successful loading was confirmed by confocal fluorescence microscopy and FIB-SEM imaging. High loading of DiD-labelled EVs was dosed in patches and microgels using trypsin degradation followed by FCS analysis. FCS analysis of the degradation products revealed the presence of EVs in high amounts. An EV uptake assay was developed and used to assess the EV integrity before and after the loading and release processes. Results indicated that released DiD-EVs could be internalised by the cells but to a lower extent compared to the original DiD-EV suspension. Finally, DiD-labelled EVs and DiD-EV-loaded degradable microgels were administered subcutaneously in mice and tracked using an *in vivo* fluorescence imaging system. Results revealed that relatively low dosages of DiD-EVs could be detected (10^9). In addition, both microgel-encapsulated and non-encapsulated DiD-EVs could be detected for a period of at least 8 days.

These results provide a proof-of-concept of the possibility to fabricate microgels loaded with high amounts of EVs and releasing them upon hydrogel degradation. Moreover, DiD was found to be a good candidate for tracking EVs both *in vivo* and *in vivo*. Experiments discussed in this chapter would, however, need to be repeated using larger sample sizes and additional controls to confirm results and allow the use of more powerful statistical tests. Methods used for EV preparation and labelling also need to be refined to ensure sterility. The protocol used for hydrogel degradation and EV release should be optimised to minimise the risks of EV damage, which can be assessed using the EV uptake assay developed in this chapter. Dose matching issues observed in section 3.2.3. should be

addressed to allow head-to-head comparison between EV and encapsulated EV samples. Although *in vitro* experiments should be utilised whenever possible to reduce the number of animals used in research, certain questions can still only be answered using *in vivo* models. Future studies should include more groups and controls (*e.g.* unlabelled EVs, unloaded microgels, non-degradable DiD-labelled EV-loaded microgels) in order to decouple the effects of each of the components on the EV fate and biodistribution. Tissue should be analysed by histology to investigate the degradation kinetics of the microgels *in vivo,* determine the location of the fluorescent signal at a tissue and cellular level and look for any local immune or toxic reaction against the treatments. Finally, providing that DiD-labelled EVs are detectable when delivered into deeper tissues, subcutaneous injections should be eventually replaced by intramyocardial injections.

Chapter 5 Conclusions and future work

The work presented in this thesis was aimed at developing a minimally-invasive microgel-based EV delivery platform for heart repair. In the last decade, the discovery of EVs has opened new avenues for the development of novel cell-free cardioprotective therapies. However, like any other drug, the efficacy of therapeutic EVs is highly dependant on the modalities used for their delivery, which include the delivery route, treatment regimen and use of strategies to modify their bioavailability. It was hypothesised that enhanced beneficial effects may be achieved through a sustained release of therapeutic EVs from injectable biodegradable microgels into the surrounding damaged tissue.

In this project, a microfluidic platform was developed to allow the fabrication of monodisperse injectable microgels. An MMP-sensitive peptide crosslinker was synthesised and incorporated into the microgels to make them responsive to inflammatory signals produced by the injured heart. Fluorescent EVs were shown to be efficiently loaded and released from the microgels following enzyme-mediated degradation of the polymer backbone. An EV uptake assay was developed to assess the functionality of the EVs after encapsulation and release from the microgels, and provided evidence of the feasibility of using a degradable microgel-based approach for EV delivery. Finally, degradable microgels loaded with fluorescent EVs were successfully tracked *in vivo* for several days following subcutaneous injection.

To the best of our knowledge, only one other study has so far looked at loading EVs into microgels [210]. Published in 2019, this study showed the feasibility of entrapping osteoblast-derived EVs in alginate microgels fabricated using an electrospraying technology. These degradable microgels were shown to sustainably release EVs *in vitro* over a period of twelve days by diffusion through the gel pores, independently of any external trigger. Therefore, the present study constitutes the first use of fluorescent EVs as a model for loading and release from microgels. It also constitute the first evidence that

encapsulating EVs in enzyme-sensitive microgels can provide control over their release profile.

Shorter term future work should focus on four aspects of the project. First, all methods involved in the fabrication of the degradable EV-loaded microgels should be scaled up to allow for the conduction of larger *in vitro* and *in vivo* studies and the use of more powerful statistical tests. High-throughput peptide synthesis could be achieved using an automated microwave-assisted technology, which was shown to be able to drastically reduce synthesis time, but also increase peptide quality and yield [246]. In this project, the methods used for EV preparation were chosen for their scalability, among other reasons. Ultrafiltration could be replaced by tangential flow filtration, a very similar membrane-based separation technique that can concentrate samples ranging in volume from a few millilitres up to thousands of litres [101]. The concentrate could then be processed using large SEC columns [84]. The microgel fabrication yield could be increased by using automated high-throughput microdroplet production systems (*e.g.* Elveflow®, Elvesys), which could be used continuously and/or in parallel to maximise the output. Utilising such equipment could also contribute to reaching high levels of quality and standardisation required for the production of clinical-grade medicinal products. The methods used for the microgel phase transfer and washing steps could be replaced by industrial-scale processes that use large tanks and high-throughput liquid filtration-based methods. Finally, automated microgel size analysis could be performed using specialised equipment such as a Mastersizer 3000 (Malvern Panalytical).

The second area of improvement is related to the quality and stability of the final product. As discussed in Chapter 3, the current lack of stability of the degradable microgels is very likely to be due to contamination issues. Ensuring sterility could drastically improve microgel stability during storage, to the point that it could potentially become an off-the-shelf product. The implementation of aseptic methods and/or sterilisation steps in the EV preparation and microgel fabrication processes, which would be required before further use in clinical trials, should be sufficient to provide satisfactory levels of stability. More specifically, the equipment, consumables and materials could be bought already sterile or

sterilised using appropriate methods, and the different steps could be performed under a laminar flow hood to maintain sterility. Other preservation methods, such as freeze-drying or the use of preservative agents, could also be employed to help stability.

Thirdly, additional evidence of the microgels biocompatibility should be provided to ensure safety prior to conducting extensive *in vitro and in vivo* efficacy experiments. As mentioned in Chapter 1, a more robust validation of the washing process is required to ascertain trace levels of the oil phase components and pentane used during the microgel fabrication. Quantification of the three trace components could be performed using chromatography-based techniques [238, 239]. The effects of microgel exposure on cell phenotype should be investigated through extensive cytotoxicity experiments using a panel of assays and performed over longer periods of time [247]. Finally, *in vitro* and *in vivo* studies looking at potential immunogenic reactions against the implanted microgels should be performed, including investigations on the potential risks of immune rejection and capsule formation, which are common side effects of implants [248].

Lastly, it is essential to extend this work with additional experiments aiming at further optimising and extensively characterising EV loading, release and uptake processes both *in vitro* and *in vivo*. In addition to using confocal and electron microscopy techniques, EV-loaded microgels could be visualised using Raman imaging, a label-free method that allows to investigate the underlying chemical components (*e.g.* proteins, lipids, genetic material) of a sample according to their vibrational spectra. More specifically, in the case of EV-loaded microgels, this method should enable to visualise the peptide-crosslinked hydrogel and lipid-based vesicles [249]. The microgel degradation rate, which directly dictates the EV release kinetics, should be tuned to allow adequate and sustained EV bioavailability in the target tissue. Their degradation profile could be adapted to the infarcted heart environment to ensure that the EV release profile covers an adequate period of time to induce optimal beneficial effects. As discussed in Chapter 3, tuning the microgel degradation kinetics could be achieved using various strategies, including using blend of non-degradable and degradable crosslinker, amending the sequence of the peptide crosslinker or changing the hydrogel formulation (*e.g.* wt%, ratio polymer-crosslinker). Furthermore, the recent

development of non-invasive *in vivo* imaging tools measuring MMP activity levels could enable the implementation of precision medicine approaches, in which each patient or subpopulation of patients could be treated with a specific hydrogel formulation that is optimal for their own microenvironment [41]. The EV uptake assay used to assess the ability of the released EVs to be internalised by target cells could be further developed on other cardiac cells (*e.g.* cardiomyocytes). The internalisation pathways used by the EVs could be investigated using pathway inhibitors such as chlorpromazine, which inhibits clathrin-dependent endocytosis [250]. Finally, Regarding the *in vivo* experiments, more groups and controls (*e.g.* unlabelled EVs, unloaded microgels, non-degradable DiD-labelled EV-loaded microgels) should be included in the study design in order to be able to decouple the effects of each of the components of the biomaterial on EV biodistribution. In addition, protocols should systematically include an histological analysis of the treated tissue to investigate EV fate and microgels degradation kinetics. On the one hand, microgels could be easily visualised and localised within tissue sections by incorporating a fluorescent label in the hydrogel network during microgel preparation, such as the one used in Chapter 3. This tissue section preparation could be coupled with other stains for immune cells (*e.g.* hematoxylin/eosin satin for foreign body giant cells) and fibrosis (*e.g.* Masson's trichrome for collagen) to investigate any local rejection reaction against the treatments [251]. On the other hand, EVs could be either directly visualised using the DiD signal or detected using an EV marker-specific antibody (*e.g.* anti-CD9, -CD63 or -CD81). Furthermore, using super resolution imaging may enable to visualise individual EVs within the injected microgels or surrounding tissues [252]. Determining the location of the EV signal at a tissue and cellular level at various timepoints may allow to better assess EV fate following delivery.

The microgel platform developed in this project was designed for cardiac repair, and longer term future work would look at adapting these protocols for intramyocardial delivery of therapeutic EVs following myocardial infarction. However, once fully optimised, the microgel system could be used as a platform for virtually any type of therapeutic EVs, including those discussed in Chapter 1. Importantly, irrespective of the chosen EV type or application, developping off-the-shelf EV-based therapies may be key to their success in the clinics. Indeed, developing ready-to-use therapies has many benefits for the patient, the

pharmaceutical company and the medical team. In addition to providing a more suitable option for acute patients, manufacturing off-the-shelf medicines provides opportunities for extensive quality control testing, resulting in higher quality products being administered to the patients themselves. From an industrial point of view, accessing a larger market could contribute to higher revenues, and manufacturing off-the-shelf medicines would allow for batch production, which reduces the production costs and allows to relatively easily scale up. Finally, from a clinician's perspective, ready-to-deliver therapies are easier to adopt and implement within existing therapeutic strategies, which represents a critical parameter in a new drug's success. In this context, developing a scalable production process centred on the use of therapeutic EVs sourced from allogeneic cells and stored in a readily available bank, as well as methods ensuring long-term stability of the final EV-based product may have a great impact on our ability to bring them to the bedside.

References

1. World Health Organization (WHO). Cardiovascular diseases (CVDs) fact sheet. 2017.

2. European Heart Network (EHN). European Cardiovascular Disease Statistics. 2017.

3. Teo, K.K. and H. Dokainish, The Emerging Epidemic of Cardiovascular Risk Factors and Atherosclerotic Disease in Developing Countries. Can J Cardiol, 2017. **33**(3): p. 358-365.

4. Cook, C., et al., The annual global economic burden of heart failure. Int J Cardiol, 2014. **171**(3): p. 368-76.

5. Rahman, M.S. and K. Woollard, *Atherosclerosis.* Adv Exp Med Biol, 2017. **1003**: p. 121-144.

6. Randomised trial of cholesterol lowering in 4444 patients with coronary heart disease: the Scandinavian Simvastatin Survival Study (4S). Lancet, 1994. **344**(8934): p. 1383-9.

7. Gimbrone, M.A., Jr. and G. Garcia-Cardena, Endothelial Cell Dysfunction and the Pathobiology of Atherosclerosis. Circ Res, 2016. **118**(4): p. 620-36.

8. Itatani, K., et al., New imaging tools in cardiovascular medicine: computational fluid dynamics and 4D flow MRI. Gen Thorac Cardiovasc Surg, 2017. **65**(11): p. 611-621.

9. Stary, H.C., Natural history and histological classification of atherosclerotic lesions: an update. Arterioscler Thromb Vasc Biol, 2000. **20**(5): p. 1177-8.

10. Sen, T., et al., Which Coronary Lesions Are More Prone to Cause Acute Myocardial Infarction? Arq Bras Cardiol, 2017. **108**(2): p. 149-53.

11. Mewton, N., et al., Infarct size reduction in patients with STEMI: why we can do it! J Cardiovasc Pharmacol Ther, 2011. **16**(3-4): p. 298-303.

12. O'Gara, P.T., et al., 2013 ACCF/AHA guideline for the management of ST-elevation myocardial infarction: executive summary: a report of the American College of Cardiology Foundation/American Heart Association Task Force on Practice Guidelines. Circulation, 2013. **127**(4): p. 529-55.

13. Liehn, E.A., et al., Repair after myocardial infarction, between fantasy and reality: the role of chemokines. J Am Coll Cardiol, 2011. **58**(23): p. 2357-62.

14. Zornoff, L.A., et al., Right ventricular dysfunction and risk of heart failure and mortality after myocardial infarction. J Am Coll Cardiol, 2002. **39**(9): p. 1450-5.

15. Brodie, B.R., et al., Importance of time to reperfusion for 30-day and late survival and recovery of left ventricular function after primary angioplasty for acute myocardial infarction. J Am Coll Cardiol, 1998. **32**(5): p. 1312-9.

16. Tran, H.V., et al., Trends in Length of Hospital Stay and the Impact on Prognosis of Early Discharge After a First Uncomplicated Acute Myocardial Infarction. Am J Cardiol, 2018. **121**(4): p. 397-402.

17. Cahill, T.J., R.P. Choudhury, and P.R. Riley, Heart regeneration and repair after myocardial infarction: translational opportunities for novel therapeutics. Nat Rev Drug Discov, 2017. **16**(10): p. 699-717.

18. Ponikowski, P., et al., 2016 ESC Guidelines for the diagnosis and treatment of acute and chronic heart failure: The Task Force for the diagnosis and treatment of acute and chronic heart failure of the European Society of Cardiology (ESC)Developed with the special contribution of the Heart Failure Association (HFA) of the ESC. Eur Heart J, 2016. **37**(27): p. 2129-2200.

19. Gyongyosi, M., et al., Meta-Analysis of Cell Therapy Studies in Heart Failure and Acute Myocardial Infarction. Circ Res, 2018. **123**(2): p. 301-308.

20. Menasche, P., Cell therapy trials for heart regeneration - lessons learned and future directions. Nat Rev Cardiol, 2018. **15**(11): p. 659-671.

21. Menasche, P., et al., The Myoblast Autologous Grafting in Ischemic Cardiomyopathy (MAGIC) trial: first randomized placebo-controlled study of myoblast transplantation. Circulation, 2008. **117**(9): p. 1189-200.

22. Pokushalov, E., et al., Efficiency of intramyocardial injections of autologous bone marrow mononuclear cells in patients with ischemic heart failure: a randomized study. J Cardiovasc Transl Res, 2010. **3**(2): p. 160-8.

23. Jimenez-Quevedo, P., et al., Selected CD133(+) progenitor cells to promote angiogenesis in patients with refractory angina: final results of the PROGENITOR randomized trial. Circ Res, 2014. **115**(11): p. 950-60.

24. Gao, L.R., et al., Intracoronary infusion of Wharton's jelly-derived mesenchymal stem cells in acute myocardial infarction: double-blind, randomized controlled trial. BMC Med, 2015. **13**: p. 162.

25. Balsam, L.B., et al., Haematopoietic stem cells adopt mature haematopoietic fates in ischaemic myocardium. Nature, 2004. **428**(6983): p. 668-73.

26. Murry, C.E., et al., Haematopoietic stem cells do not transdifferentiate into cardiac myocytes in myocardial infarcts. Nature, 2004. **428**(6983): p. 664-8.

27. Barile, L., et al., Endogenous cardiac stem cells. Prog Cardiovasc Dis, 2007. **50**(1): p. 31-48.

28. Mummery, C.L., et al., Differentiation of human embryonic stem cells and induced pluripotent stem cells to cardiomyocytes: a methods overview. Circ Res, 2012. **111**(3): p. 344-58.

29. Makkar, R.R., et al., Intracoronary cardiosphere-derived cells for heart regeneration after myocardial infarction (CADUCEUS): a prospective, randomised phase 1 trial. Lancet, 2012. **379**(9819): p. 895-904.

30. Menasche, P., et al., Transplantation of Human Embryonic Stem Cell-Derived Cardiovascular Progenitors for Severe Ischemic Left Ventricular Dysfunction. J Am Coll Cardiol, 2018. **71**(4): p. 429-438.

31. Zimmermann, W.H., Remuscularization of the failing heart. J Physiol, 2017. **595**(12): p. 3685-3690.

32. Blum, B. and N. Benvenisty, The tumorigenicity of human embryonic stem cells. Adv Cancer Res, 2008. **100**: p. 133-58.

33. Chong, J.J., et al., Human embryonic-stem-cell-derived cardiomyocytes regenerate non-human primate hearts. Nature, 2014. **510**(7504): p. 273-7.

34. Malliaras, K., et al., Safety and efficacy of allogeneic cell therapy in infarcted rats transplanted with mismatched cardiosphere-derived cells. Circulation, 2012. **125**(1): p. 100-12.

35. Zhuo, Y., et al., Aging impairs the angiogenic response to ischemic injury and the activity of implanted cells: combined consequences for cell therapy in older recipients. J Thorac Cardiovasc Surg, 2010. **139**(5): p. 1286-94, 1294.e1-2.

36. Kanelidis, A.J., et al., Route of Delivery Modulates the Efficacy of Mesenchymal Stem Cell Therapy for Myocardial Infarction: A Meta-Analysis of Preclinical Studies and Clinical Trials. Circ Res, 2017. **120**(7): p. 1139-1150.

37. Hashimoto, H., E.N. Olson, and R. Bassel-Duby, Therapeutic approaches for cardiac regeneration and repair. Nat Rev Cardiol, 2018. **15**(10): p. 585-600.

38. Ahuja, P., P. Sdek, and W.R. MacLellan, Cardiac myocyte cell cycle control in development, disease, and regeneration. Physiol Rev, 2007. **87**(2): p. 521-44.

39. Bergmann, O., et al., Evidence for cardiomyocyte renewal in humans. Science, 2009. **324**(5923): p. 98-102.

40. Zacchigna, S. and M. Giacca, Extra- and intracellular factors regulating cardiomyocyte proliferation in postnatal life. Cardiovasc Res, 2014. **102**(2): p. 312-20.

41. Sahul, Z.H., et al., Targeted imaging of the spatial and temporal variation of matrix metalloproteinase activity in a porcine model of postinfarct remodeling: relationship to myocardial dysfunction. Circ Cardiovasc Imaging, 2011. **4**(4): p. 381-91.

42. Hu, X., et al., Optimal temporal delivery of bone marrow mesenchymal stem cells in rats with myocardial infarction. Eur J Cardiothorac Surg, 2007. **31**(3): p. 438-43.

43. Jiang, C.Y., et al., Optimal time for mesenchymal stem cell transplantation in rats with myocardial infarction. J Zhejiang Univ Sci B, 2008. **9**(8): p. 630-7.

44. Davis, B.H., et al., Effects of myocardial infarction on the distribution and transport of nutrients and oxygen in porcine myocardium. J Biomech Eng, 2012. **134**(10): p. 101005.

45. Li, R.K., et al., Optimal time for cardiomyocyte transplantation to maximize myocardial function after left ventricular injury. Ann Thorac Surg, 2001. **72**(6): p. 1957-63.

46. Traverse, J.H., et al., Effect of the use and timing of bone marrow mononuclear cell delivery on left ventricular function after acute myocardial infarction: the TIME randomized trial. Jama, 2012. **308**(22): p. 2380-9.

47. Huang, R., et al., Timing for intracoronary administration of bone marrow mononuclear cells after acute ST-elevation myocardial infarction: a pilot study. Stem Cell Res Ther, 2015. **6**: p. 112.

48. Surder, D., et al., Effect of Bone Marrow-Derived Mononuclear Cell Treatment, Early or Late After Acute Myocardial Infarction: Twelve Months CMR and Long-Term Clinical Results. Circ Res, 2016. **119**(3): p. 481-90.

49. Johnson, T.D. and K.L. Christman, Injectable hydrogel therapies and their delivery strategies for treating myocardial infarction. Expert Opin Drug Deliv, 2013. **10**(1): p. 59-72.

50. Hou, D., et al., Radiolabeled cell distribution after intramyocardial, intracoronary, and interstitial retrograde coronary venous delivery: implications for current clinical trials. Circulation, 2005. **112**(9 Suppl): p. I150-6.

51. Garbayo, E., et al., Catheter-based Intramyocardial Injection of FGF1 or NRG1-loaded MPs Improves Cardiac Function in a Preclinical Model of Ischemia-Reperfusion. Sci Rep, 2016. **6**: p. 25932.

52. Perin, E.C., et al., Effect of transendocardial delivery of autologous bone marrow mononuclear cells on functional capacity, left ventricular function, and perfusion in chronic heart failure: the FOCUS-CCTRN trial. Jama, 2012. **307**(16): p. 1717-26.

53. Hare, J.M., Translational development of mesenchymal stem cell therapy for cardiovascular diseases. Tex Heart Inst J, 2009. **36**(2): p. 145-7.

54. Perin, E.C., et al., A randomized study of transendocardial injection of autologous bone marrow mononuclear cells and cell function analysis in ischemic heart failure (FOCUS-HF). Am Heart J, 2011. **161**(6): p. 1078-87.e3.

55. Henry, T.D., et al., The Athena trials: Autologous adipose-derived regenerative cells for refractory chronic myocardial ischemia with left ventricular dysfunction. Catheter Cardiovasc Interv, 2017. **89**(2): p. 169-177.

56. Teerlink, J.R., et al., Benefit of cardiopoietic mesenchymal stem cell therapy on left ventricular remodelling: results from the Congestive Heart Failure Cardiopoietic Regenerative Therapy (CHART-1) study. Eur J Heart Fail, 2017. **19**(11): p. 1520-1529.

57. Vrtovec, B., et al., Effects of Repetitive Transendocardial CD34(+) Cell Transplantation in Patients With Nonischemic Dilated Cardiomyopathy. Circ Res, 2018. **123**(3): p. 389-396.

58. Kastrup, J., et al., A randomised, double-blind, placebo-controlled, multicentre study of the safety and efficacy of BIOBYPASS (AdGVVEGF121.10NH) gene therapy in patients with refractory advanced coronary artery disease: the NOVA trial. EuroIntervention, 2011. **6**(7): p. 813-8.

59. Krause, K., et al., Percutaneous intramyocardial stem cell injection in patients with acute myocardial infarction: first-in-man study. Heart, 2009. **95**(14): p. 1145-52.

60. Shiba, Y., et al., Allogeneic transplantation of iPS cell-derived cardiomyocytes regenerates primate hearts. Nature, 2016. **538**(7625): p. 388-391.

61. Uemura, R., et al., Bone marrow stem cells prevent left ventricular remodeling of ischemic heart through paracrine signaling. Circ Res, 2006. **98**(11): p. 1414-21.

62. Chimenti, I., et al., Relative roles of direct regeneration versus paracrine effects of human cardiosphere-derived cells transplanted into infarcted mice. Circ Res, 2010. **106**(5): p. 971-80.

63. Tang, X.L., et al., Long-Term Outcome of Administration of c-kit(POS) Cardiac Progenitor Cells After Acute Myocardial Infarction: Transplanted Cells Do not Become Cardiomyocytes, but Structural and Functional Improvement and Proliferation of Endogenous Cells Persist for at Least One Year. Circ Res, 2016. **118**(7): p. 1091-105.

64. Korf-Klingebiel, M., et al., Bone marrow cells are a rich source of growth factors and cytokines: implications for cell therapy trials after myocardial infarction. Eur Heart J, 2008. **29**(23): p. 2851-8.

65. Pachler, K., et al., A Good Manufacturing Practice-grade standard protocol for exclusively human mesenchymal stromal cell-derived extracellular vesicles. Cytotherapy, 2017. **19**(4): p. 458-472.

66. Beohar, N., et al., Rebuilding the damaged heart: the potential of cytokines and growth factors in the treatment of ischemic heart disease. J Am Coll Cardiol, 2010. **56**(16): p. 1287-97.

67. Lang, J.K., et al., Inhibiting Extracellular Vesicle Release from Human Cardiosphere Derived Cells with Lentiviral Knockdown of nSMase2 Differentially Effects Proliferation and Apoptosis in Cardiomyocytes, Fibroblasts and Endothelial Cells In Vitro. PLoS One, 2016. **11**(11): p. e0165926.

68. Timmers, L., et al., Reduction of myocardial infarct size by human mesenchymal stem cell conditioned medium. Stem Cell Res, 2007. **1**(2): p. 129-37.

69. Maring, J.A., et al., Cardiac Progenitor Cell-Derived Extracellular Vesicles Reduce Infarct Size and Associate with Increased Cardiovascular Cell Proliferation. J Cardiovasc Transl Res, 2019. **12**(1): p. 5-17.

70. Gupta, S. and A.A. Knowlton, HSP60 trafficking in adult cardiac myocytes: role of the exosomal pathway. Am J Physiol Heart Circ Physiol, 2007. **292**(6): p. H3052-6.

71. Pironti, G., et al., Circulating Exosomes Induced by Cardiac Pressure Overload Contain Functional Angiotensin II Type 1 Receptors. Circulation, 2015. **131**(24): p. 2120-30.

72. Song, J., et al., Cardiac endothelial cell-derived exosomes induce specific regulatory B cells. Sci Rep, 2014. **4**: p. 7583.

73. Bang, C., et al., Cardiac fibroblast-derived microRNA passenger strand-enriched exosomes mediate cardiomyocyte hypertrophy. J Clin Invest, 2014. **124**(5): p. 2136-46.

74. De Jong, O.G., et al., Extracellular vesicles: potential roles in regenerative medicine. Front Immunol, 2014. **5**: p. 608.

75. Montecalvo, A., et al., Mechanism of transfer of functional microRNAs between mouse dendritic cells via exosomes. Blood, 2012. **119**(3): p. 756-66.

76. Yanez-Mo, M., et al., Biological properties of extracellular vesicles and their physiological functions. J Extracell Vesicles, 2015. **4**: p. 27066.

77. Morelli, A.E., et al., Endocytosis, intracellular sorting, and processing of exosomes by dendritic cells. Blood, 2004. **104**(10): p. 3257-66.

78. Turturici, G., et al., Extracellular membrane vesicles as a mechanism of cell-to-cell communication: advantages and disadvantages. Am J Physiol Cell Physiol, 2014. **306**(7): p. C621-33.

79. Robbins, P.D. and A.E. Morelli, Regulation of immune responses by extracellular vesicles. Nat Rev Immunol, 2014. **14**(3): p. 195-208.

80. Holm, M.M., J. Kaiser, and M.E. Schwab, Extracellular Vesicles: Multimodal Envoys in Neural Maintenance and Repair. Trends Neurosci, 2018. **41**(6): p. 360-372.

81. Becker, A., et al., Extracellular Vesicles in Cancer: Cell-to-Cell Mediators of Metastasis. Cancer Cell, 2016. **30**(6): p. 836-848.

82. Sluijter, J.P.G., et al., Extracellular vesicles in diagnostics and therapy of the ischaemic heart: Position Paper from the Working Group on Cellular Biology of the Heart of the European Society of Cardiology. Cardiovasc Res, 2018. **114**(1): p. 19-34.

83. Mirotsou, M., A. Blusztanj, and I. Tremmel, Repeated doses of cardiosphere-derived cell extracellular vesicles are hypo-immunogenic., in 4th International Meeting of ISEV (ISEV '15). 2015: Washington, DC, USA.

84. Paganini, C., et al., Scalable Production and Isolation of Extracellular Vesicles: Available Sources and Lessons from Current Industrial Bioprocesses. Biotechnol J, 2019: p. e1800528.

85. Vlassov, A.V., et al., Exosomes: current knowledge of their composition, biological functions, and diagnostic and therapeutic potentials. Biochim Biophys Acta, 2012. **1820**(7): p. 940-8.

86. Akers, J.C., et al., Optimizing preservation of extracellular vesicular miRNAs derived from clinical cerebrospinal fluid. Cancer Biomark, 2016. **17**(2): p. 125-32.

87. Charoenviriyakul, C., et al., Preservation of exosomes at room temperature using lyophilization. Int J Pharm, 2018. **553**(1-2): p. 1-7.

88. Frank, J., et al., Extracellular vesicles protect glucuronidase model enzymes during freeze-drying. Sci Rep, 2018. **8**(1): p. 12377.

89. Coumans, F.A.W., et al., Methodological Guidelines to Study Extracellular Vesicles. Circ Res, 2017. **120**(10): p. 1632-1648.

90. Shelke, G.V., et al., Importance of exosome depletion protocols to eliminate functional and RNA-containing extracellular vesicles from fetal bovine serum. J Extracell Vesicles, 2014. **3**.

91. Kornilov, R., et al., Efficient ultrafiltration-based protocol to deplete extracellular vesicles from fetal bovine serum. J Extracell Vesicles, 2018. **7**(1): p. 1422674.

92. Gyorgy, B., et al., Detection and isolation of cell-derived microparticles are compromised by protein complexes resulting from shared biophysical parameters. Blood, 2011. **117**(4): p. e39-48.

93. Yuana, Y., et al., Co-isolation of extracellular vesicles and high-density lipoproteins using density gradient ultracentrifugation. J Extracell Vesicles, 2014. **3**.

94. Baranyai, T., et al., Isolation of Exosomes from Blood Plasma: Qualitative and Quantitative Comparison of Ultracentrifugation and Size Exclusion Chromatography Methods. PLoS One, 2015. **10**(12): p. e0145686.

95. Linares, R., et al., High-speed centrifugation induces aggregation of extracellular vesicles. J Extracell Vesicles, 2015. **4**: p. 29509.

96. Lobb, R.J., et al., Optimized exosome isolation protocol for cell culture supernatant and human plasma. J Extracell Vesicles, 2015. **4**: p. 27031.

97. Monguio-Tortajada, M., et al., Extracellular vesicle isolation methods: rising impact of size-exclusion chromatography. Cell Mol Life Sci, 2019. **76**(12): p. 2369-2382.

98. Nordin, J.Z., et al., Ultrafiltration with size-exclusion liquid chromatography for high yield isolation of extracellular vesicles preserving intact biophysical and functional properties. Nanomedicine, 2015. **11**(4): p. 879-83.

99. Benedikter, B.J., et al., Ultrafiltration combined with size exclusion chromatography efficiently isolates extracellular vesicles from cell culture media for compositional and functional studies. Sci Rep, 2017. **7**(1): p. 15297.

100. Guerreiro, E.M., et al., Efficient extracellular vesicle isolation by combining cell media modifications, ultrafiltration, and size-exclusion chromatography. PLoS One, 2018. **13**(9): p. e0204276.

101. Busatto, S., et al., Tangential Flow Filtration for Highly Efficient Concentration of Extracellular Vesicles from Large Volumes of Fluid. Cells, 2018. **7**(12).

102. Welton, J.L., et al., Ready-made chromatography columns for extracellular vesicle isolation from plasma, in J Extracell Vesicles. 2015: Sweden. p. 27269.

103. Lotvall, J., et al., Minimal experimental requirements for definition of extracellular vesicles and their functions: a position statement from the International Society for Extracellular Vesicles. J Extracell Vesicles, 2014. **3**: p. 26913.

104. Van Deun, J., et al., EV-TRACK: transparent reporting and centralizing knowledge in extracellular vesicle research. Nat Methods, 2017. **14**(3): p. 228-232.

105. Cruz, L., et al., Evidence of Extracellular Vesicles Biogenesis and Release in Mouse Embryonic Stem Cells. Stem Cell Rev, 2018. **14**(2): p. 262-276.

106. Pan, B.T., et al., Electron microscopic evidence for externalization of the transferrin receptor in vesicular form in sheep reticulocytes. J Cell Biol, 1985. **101**(3): p. 942-8.

107. Fischer, K., et al., High pressure freezing/freeze substitution fixation improves the ultrastructural assessment of Wolbachia endosymbiont-filarial nematode host interaction. PLoS One, 2014. **9**(1): p. e86383.

108. Carnell-Morris, P., et al., Analysis of Extracellular Vesicles Using Fluorescence Nanoparticle Tracking Analysis. Methods Mol Biol, 2017. **1660**: p. 153-173.

109. Maas, S.L., J. De Vrij, and M.L. Broekman, Quantification and size-profiling of extracellular vesicles using tunable resistive pulse sensing. J Vis Exp, 2014(92): p. e51623.

110. Hill, A.F., et al., ISEV position paper: extracellular vesicle RNA analysis and bioinformatics. J Extracell Vesicles, 2013. **2**.

111. Coumans, F.A.W., E.L. Gool, and R. Nieuwland, Bulk immunoassays for analysis of extracellular vesicles. Platelets, 2017. **28**(3): p. 242-248.

112. Nolan, J.P., Flow Cytometry of Extracellular Vesicles: Potential, Pitfalls, and Prospects. Curr Protoc Cytom, 2015. **73**: p. 13.14.1-16.

113. Welsh, J.A., et al., Extracellular Vesicle Flow Cytometry Analysis and Standardization. Front Cell Dev Biol, 2017. **5**: p. 78.

114. Altadill, T., et al., Enabling Metabolomics Based Biomarker Discovery Studies Using Molecular Phenotyping of Exosome-Like Vesicles. PLoS One, 2016. **11**(3): p. e0151339.

115. Pittenger, M.F., et al., Multilineage potential of adult human mesenchymal stem cells. Science, 1999. **284**(5411): p. 143-7.

116. Lin, Y., et al., Multilineage differentiation of adipose-derived stromal cells from GFP transgenic mice. Mol Cell Biochem, 2006. **285**(1-2): p. 69-78.

117. Faiella, W. and R. Atoui, Immunotolerant Properties of Mesenchymal Stem Cells: Updated Review. Stem Cells Int, 2016. **2016**.

118. Lai, R.C., et al., Exosome secreted by MSC reduces myocardial ischemia/reperfusion injury. Stem Cell Res, 2010. **4**(3): p. 214-22.

119. Arslan, F., et al., Mesenchymal stem cell-derived exosomes increase ATP levels, decrease oxidative stress and activate PI3K/Akt pathway to enhance myocardial viability and prevent adverse remodeling after myocardial ischemia/reperfusion injury. Stem Cell Res, 2013. **10**(3): p. 301-12.

120. Bian, S., et al., Extracellular vesicles derived from human bone marrow mesenchymal stem cells promote angiogenesis in a rat myocardial infarction model. J Mol Med (Berl), 2014. **92**(4): p. 387-97.

121. Zhao, Y., et al., Exosomes Derived from Human Umbilical Cord Mesenchymal Stem Cells Relieve Acute Myocardial Ischemic Injury. Stem Cells Int, 2015. **2015**: p. 761643.

122. Zhang, H., et al., Inhibition of Myocardial Ischemia/Reperfusion Injury by Exosomes Secreted from Mesenchymal Stem Cells. Stem Cells Int, 2016. **2016**: p. 4328362.

123. Chen, L., et al., Cardiac progenitor-derived exosomes protect ischemic myocardium from acute ischemia/reperfusion injury. Biochem Biophys Res Commun, 2013. **431**(3): p. 566-71.

124. Barile, L., et al., Extracellular vesicles from human cardiac progenitor cells inhibit cardiomyocyte apoptosis and improve cardiac function after myocardial infarction. Cardiovasc Res, 2014. **103**(4): p. 530-41.

125. Ibrahim, A.G., K. Cheng, and E. Marban, Exosomes as critical agents of cardiac regeneration triggered by cell therapy. Stem Cell Reports, 2014. **2**(5): p. 606-19.

126. Agarwal, U., et al., Experimental, Systems, and Computational Approaches to Understanding the MicroRNA-Mediated Reparative Potential of Cardiac Progenitor Cell-Derived Exosomes From Pediatric Patients. Circ Res, 2017. **120**(4): p. 701-712.

127. Gallet, R., et al., Exosomes secreted by cardiosphere-derived cells reduce scarring, attenuate adverse remodelling, and improve function in acute and chronic porcine myocardial infarction. Eur Heart J, 2017. **38**(3): p. 201-211.

128. Barile, L., et al., Cardioprotection by cardiac progenitor cell-secreted exosomes: role of pregnancy-associated plasma protein-A. Cardiovasc Res, 2018. **114**(7): p. 992-1005.

129. Kervadec, A., et al., Cardiovascular progenitor-derived extracellular vesicles recapitulate the beneficial effects of their parent cells in the treatment of chronic heart failure. J Heart Lung Transplant, 2016. **35**(6): p. 795-807.

130. Liu, B., et al., Cardiac recovery via extended cell-free delivery of extracellular vesicles secreted by cardiomyocytes derived from induced pluripotent stem cells. Nat Biomed Eng, 2018. **2**(5): p. 293-303.

131. Adamiak, M. and S. Sahoo, Exosomes in Myocardial Repair: Advances and Challenges in the Development of Next-Generation Therapeutics. Mol Ther, 2018. **26**(7): p. 1635-1643.

132. Gimona, M., et al., Manufacturing of Human Extracellular Vesicle-Based Therapeutics for Clinical Use. Int J Mol Sci, 2017. **18**(6).

133. Lener, T., et al., Applying extracellular vesicles based therapeutics in clinical trials - an ISEV position paper. J Extracell Vesicles, 2015. **4**: p. 30087.

134. Lai, C.P., et al., Dynamic biodistribution of extracellular vesicles in vivo using a multimodal imaging reporter. ACS Nano, 2014. **8**(1): p. 483-494.

135. Grossman, P.M., et al., Incomplete retention after direct myocardial injection. Catheter Cardiovasc Interv, 2002. **55**(3): p. 392-7.

136. Fernandez-Aviles, F., et al., Global position paper on cardiovascular regenerative medicine. Eur Heart J, 2017. **38**(33): p. 2532-2546.

137. Parhi, R., Cross-Linked Hydrogel for Pharmaceutical Applications: A Review. Adv Pharm Bull, 2017. **7**(4): p. 515-530.

138. Lin, C.C., Recent advances in crosslinking chemistry of biomimetic poly(ethylene glycol) hydrogels. RSC Adv, 2015. **5**(50): p. 39844-398583.

139. Annabi, N., et al., Controlling the porosity and microarchitecture of hydrogels for tissue engineering. Tissue Eng Part B Rev, 2010. **16**(4): p. 371-83.

140. Kamath, K.R. and K. Park, Biodegradable hydrogels in drug delivery. Adv. Drug Deliv. Rev, 1993. **11**(1-2): p. 59-84.

141. Yang, J., et al., Cell-laden hydrogels for osteochondral and cartilage tissue engineering. Acta Biomater, 2017. **57**: p. 1-25.

142. Frey, N., et al., Intracoronary delivery of injectable bioabsorbable scaffold (IK-5001) to treat left ventricular remodeling after ST-elevation myocardial infarction: a first-in-man study. Circ Cardiovasc Interv, 2014. **7**(6): p. 806-12.

143. Saludas, L., et al., Hydrogel based approaches for cardiac tissue engineering. Int J Pharm, 2017. **523**(2): p. 454-475.

144. Rao, S.V., et al., Bioabsorbable Intracoronary Matrix for Prevention of Ventricular Remodeling After Myocardial Infarction. J Am Coll Cardiol, 2016. **68**(7): p. 715-23.

145. Anker, S.D., et al., A prospective comparison of alginate-hydrogel with standard medical therapy to determine impact on functional capacity and clinical outcomes in patients with advanced heart failure (AUGMENT-HF trial). Eur Heart J, 2015. **36**(34): p. 2297-309.

146. Lee, R.J., et al., The feasibility and safety of Algisyl-LVR as a method of left ventricular augmentation in patients with dilated cardiomyopathy: initial first in man clinical results. Int J Cardiol, 2015. **199**: p. 18-24.

147. Mann, D.L., et al., One-year follow-up results from AUGMENT-HF: a multicentre randomized controlled clinical trial of the efficacy of left ventricular augmentation with Algisyl in the treatment of heart failure. Eur J Heart Fail, 2016. **18**(3): p. 314-25.

148. Takehara, N., et al., The ALCADIA (autologous Human Cardiac-derived Stem Cell To Treat Ischemic Cardiomyopathy) Trial, in Scientific Sessions of the American-Heart-Association. 2012: Los Angeles, CA, USA.

149. Nicodemus, G.D. and S.J. Bryant, Cell encapsulation in biodegradable hydrogels for tissue engineering applications. Tissue Eng Part B Rev, 2008. **14**(2): p. 149-65.

150. Rane, A.A., et al., Increased infarct wall thickness by a bio-inert material is insufficient to prevent negative left ventricular remodeling after myocardial infarction. PLoS One, 2011. **6**(6): p. e21571.

151. Scott, M.D. and K.L. Murad, Cellular camouflage: fooling the immune system with polymers. Curr Pharm Des, 1998. **4**(6): p. 423-38.

152. Alcantar, N.A., E.S. Aydil, and J.N. Israelachvili, *Polyethylene glycol-coated biocompatible surfaces.* J Biomed Mater Res, 2000. **51**(3): p. 343-51.

153. Csucs, G., et al., Microcontact printing of novel co-polymers in combination with proteins for cell-biological applications. Biomaterials, 2003. **24**(10): p. 1713-20.

154. Jeon, S.I., et al., Protein—surface interactions in the presence of polyethylene oxide. Journal of Colloid and Interface Science, 2019.

155. Klopfleisch, R. and F. Jung, The pathology of the foreign body reaction against biomaterials. J Biomed Mater Res A, 2017. **105**(3): p. 927-940.

156. Abuchowski, A., et al., Alteration of immunological properties of bovine serum albumin by covalent attachment of polyethylene glycol. J Biol Chem, 1977. **252**(11): p. 3578-81.

157. Kim, T.H., H. Lee, and T.G. Park, Pegylated recombinant human epidermal growth factor (rhEGF) for sustained release from biodegradable PLGA microspheres. Biomaterials, 2002. **23**(11): p. 2311-7.

158. Bozzoli, V., et al., Four doses of unpegylated versus one dose of pegylated filgrastim as supportive therapy in R-CHOP-14 for elderly patients with diffuse large B-cell lymphoma. Br J Haematol, 2015. **169**(6): p. 787-94.

159. Peppas, N.A., et al., Poly(ethylene glycol)-containing hydrogels in drug delivery. J Control Release, 1999. **62**(1-2): p. 81-7.

160. Kade, M.J., Burke, D. J., Hawker, C. J., *The power of thiol–ene chemistry.* J. Polym. Sci. A Polym. Chem., 2010. **48**(4): p. 743-750.

161. Hoyle, C.E., A.B. Lowe, and C.N. Bowman, Thiol-click chemistry: a multifaceted toolbox for small molecule and polymer synthesis. Chem Soc Rev, 2010. **39**(4): p. 1355-87.

162. Nguyen, L.T., Gokmen M.T., Du Prez F.E., Kinetic comparison of 13 homogeneous thiol–X reactions. Polym. Chem., 2013(4): p. 5527-5536.

163. Nguyen, K.T. and J.L. West, Photopolymerizable hydrogels for tissue engineering applications. Biomaterials, 2002. **23**(22): p. 4307-14.

164. Kharkar, P.M., et al., Thiol-ene click hydrogels for therapeutic delivery. ACS Biomater Sci Eng, 2016. **2**(2): p. 165-179.

165. Malkoch, M., et al., Synthesis of well-defined hydrogel networks using click chemistry. Chem Commun (Camb), 2006(26): p. 2774-6.

166. Peppas, N.A., et al., Hydrogels in pharmaceutical formulations. Eur J Pharm Biopharm, 2000. **50**(1): p. 27-46.

167. Lin, C.C. and A.T. Metters, Hydrogels in controlled release formulations: network design and mathematical modeling. Adv Drug Deliv Rev, 2006. **58**(12-13): p. 1379-408.

168. Zustiak, S.P. and J.B. Leach, Hydrolytically degradable poly(ethylene glycol) hydrogel scaffolds with tunable degradation and mechanical properties. Biomacromolecules, 2010. **11**(5): p. 1348-57.

169. Lee, S., X. Tong, and F. Yang, The effects of varying poly(ethylene glycol) hydrogel crosslinking density and the crosslinking mechanism on protein accumulation in three-dimensional hydrogels. Acta Biomater, 2014. **10**(10): p. 4167-74.

170. Kloxin, A.M., et al., Photodegradable hydrogels for dynamic tuning of physical and chemical properties. Science, 2009. **324**(5923): p. 59-63.

171. Lin, C.C. and K.S. Anseth, PEG hydrogels for the controlled release of biomolecules in regenerative medicine. Pharm Res, 2009. **26**(3): p. 631-43.

172. Saini, P., M. Arora, and M. Kumar, Poly(lactic acid) blends in biomedical applications. Adv Drug Deliv Rev, 2016. **107**: p. 47-59.

173. Kloxin, A.M., et al., Tunable hydrogels for external manipulation of cellular microenvironments through controlled photodegradation. Adv Mater, 2010. **22**(1): p. 61-6.

174. McKinnon, D.D., et al., Design and characterization of a synthetically accessible, photodegradable hydrogel for user-directed formation of neural networks. Biomacromolecules, 2014. **15**(7): p. 2808-16.

175. Ash, C., et al., Effect of wavelength and beam width on penetration in light-tissue interaction using computational methods, in Lasers Med Sci. 2017. p. 1909-18.

176. Patterson, J. and J.A. Hubbell, Enhanced proteolytic degradation of molecularly engineered PEG hydrogels in response to MMP-1 and MMP-2. Biomaterials, 2010. **31**(30): p. 7836-45.

177. Lutolf, M.P. and J.A. Hubbell, Synthesis and physicochemical characterization of end-linked poly(ethylene glycol)-co-peptide hydrogels formed by Michael-type addition. Biomacromolecules, 2003. **4**(3): p. 713-22.

178. Lutolf, M.P., et al., Synthetic matrix metalloproteinase-sensitive hydrogels for the conduction of tissue regeneration: engineering cell-invasion characteristics. Proc Natl Acad Sci U S A, 2003. **100**(9): p. 5413-8.

179. Squire, I.B., et al., Plasma MMP-9 and MMP-2 following acute myocardial infarction in man: correlation with echocardiographic and neurohumoral parameters of left ventricular dysfunction. J Card Fail, 2004. **10**(4): p. 328-33.

180. Chen, J., et al., Near-infrared fluorescent imaging of matrix metalloproteinase activity after myocardial infarction. Circulation, 2005. **111**(14): p. 1800-5.

181. Kraehenbuehl, T.P., et al., Human embryonic stem cell-derived microvascular grafts for cardiac tissue preservation after myocardial infarction. Biomaterials, 2011. **32**(4): p. 1102-9.

182. Anderson, S.B., et al., The performance of human mesenchymal stem cells encapsulated in cell-degradable polymer-peptide hydrogels. Biomaterials, 2011. **32**(14): p. 3564-74.

183. Li, J. and D.J. Mooney, Designing hydrogels for controlled drug delivery. Nat Rev Mater, 2016. **1**(12).

184. Huang, X. and C.S. Brazel, On the importance and mechanisms of burst release in matrix-controlled drug delivery systems. J Control Release, 2001. **73**(2-3): p. 121-36.

185. Andreopoulos, F.M. and I. Persaud, Delivery of basic fibroblast growth factor (bFGF) from photoresponsive hydrogel scaffolds. Biomaterials, 2006. **27**(11): p. 2468-76.

186. Fishburn, C.S., The pharmacology of PEGylation: balancing PD with PK to generate novel therapeutics. J Pharm Sci, 2008. **97**(10): p. 4167-83.

187. Zisch, A.H., et al., Cell-demanded release of VEGF from synthetic, biointeractive cell ingrowth matrices for vascularized tissue growth. Faseb j, 2003. **17**(15): p. 2260-2.

188. Temenoff, J.S., et al., In vitro cytotoxicity of redox radical initiators for cross-linking of oligo(poly(ethylene glycol) fumarate) macromers. Biomacromolecules, 2003. **4**(6): p. 1605-13.

189. De France, K.J., F. Xu, and T. Hoare, Structured Macroporous Hydrogels: Progress, Challenges, and Opportunities. Adv Healthc Mater, 2018. **7**(1).

190. Guvendiren, M., H.D. Lu, and J.A. Burdick, Shear-thinning hydrogels for biomedical applications. 2011.

191. Pacheco, P., D. White, and T. Sulchek, Effects of microparticle size and Fc density on macrophage phagocytosis. PLoS One, 2013. **8**(4): p. e60989.

192. Foster, G.A., et al., Protease-degradable microgels for protein delivery for vascularization. Biomaterials, 2017. **113**: p. 170-175.

193. Tobita, H., Kumagai, M., Aoyagi, N., Microgel formation in emulsion polymerization. Polymer, 2000. **41**(2): p. 481-487.

194. Serrano-Medina, A., J.M. Cornejo-Bravo, and A. Licea-Claverie, Synthesis of pH and temperature sensitive, core-shell nano/microgels, by one pot, soap-free emulsion polymerization. J Colloid Interface Sci, 2012. **369**(1): p. 82-90.

195. Siltanen, C., et al., Microfluidic fabrication of bioactive microgels for rapid formation and enhanced differentiation of stem cell spheroids. Acta Biomater, 2016. **34**: p. 125-132.

196. Meng, Z., Smith, M.H., Lyon, L.A., Temperature-programmed synthesis of micron-sized multi-responsive microgels. Colloid Polym. Sci, 2009. **287**(3): p. 277–285.

197. Flake, M.M., et al., Poly(ethylene glycol) microparticles produced by precipitation polymerization in aqueous solution. Biomacromolecules, 2011. **12**(3): p. 844-50.

198. Panda, P., et al., Stop-flow lithography to generate cell-laden microgel particles. Lab Chip, 2008. **8**(7): p. 1056-61.

199. Barron, C. and J.Q. He, Alginate-based microcapsules generated with the coaxial electrospray method for clinical application. J Biomater Sci Polym Ed, 2017. **28**(13): p. 1245-1255.

200. Wright, E.J., et al., Encapsulated glucagon-like peptide-1-producing mesenchymal stem cells have a beneficial effect on failing pig hearts. Stem Cells Transl Med, 2012. **1**(10): p. 759-69.

201. Yang, Y., et al., MRI study of cryoinjury infarction in pig hearts: i. Effects of intrapericardial delivery of bFGF/VEGF embedded in alginate beads. NMR Biomed, 2012. **25**(1): p. 177-88.

202. Cavalieri, F., et al., Novel PVA-based hydrogel microparticles for doxorubicin delivery. Biomacromolecules, 2008. **9**(7): p. 1967-73.

203. Wanakule, P., et al., Nano-inside-micro: Disease-responsive microgels with encapsulated nanoparticles for intracellular drug delivery to the deep lung. J Control Release, 2012. **162**(2): p. 429-37.

204. Das, A., et al., Delivery of bioactive lipids from composite microgel-microsphere injectable scaffolds enhances stem cell recruitment and skeletal repair. PLoS One, 2014. **9**(7): p. e101276.

205. Houtgraaf, J.H., et al., Feasibility of intracoronary GLP-1 eluting CellBead infusion in acute myocardial infarction. Cell Transplant, 2013. **22**(3): p. 535-43.

206. Lopez, J.J. and M. Simons, Local Extravascular Growth Factor Delivery in Myocardial Ischemia. Drug Deliv, 1996. **3**(3): p. 143-7.

207. Stenekes, R.J., et al., Degradable dextran microspheres for the controlled release of liposomes. Int J Pharm, 2001. **214**(1-2): p. 17-20.

208. Feng, S.S., G. Ruan, and Q.T. Li, Fabrication and characterizations of a novel drug delivery device liposomes-in-microsphere (LIM). Biomaterials, 2004. **25**(21): p. 5181-9.

209. Guo, X., et al., Continuous delivery of propranolol from liposomes-in-microspheres significantly inhibits infantile hemangioma growth. Int J Nanomedicine, 2017. **12**: p. 6923-6936.

210. Nikravesh, N., et al., Physical Structuring of Injectable Polymeric Systems to Controllably Deliver Nanosized Extracellular Vesicles. Adv Healthc Mater, 2019. **8**(9): p. e1801604.

211. Liu, X., et al., Integration of stem cell-derived exosomes with in situ hydrogel glue as a promising tissue patch for articular cartilage regeneration. Nanoscale, 2017. **9**(13): p. 4430-4438.

212. Zhang, Y., et al., Exosomes from human umbilical cord mesenchymal stem cells enhance fracture healing through HIF-1alpha-mediated promotion of angiogenesis in a rat model of stabilized fracture. Cell Prolif, 2019. **52**(2): p. e12570.

213. Zhang, K., et al., Enhanced Therapeutic Effects of Mesenchymal Stem Cell-Derived Exosomes with an Injectable Hydrogel for Hindlimb Ischemia Treatment. ACS Appl Mater Interfaces, 2018. **10**(36): p. 30081-30091.

214. Cittadini, A., et al., Complementary therapeutic effects of dual delivery of insulin-like growth factor-1 and vascular endothelial growth factor by gelatin microspheres in experimental heart failure. Eur J Heart Fail, 2011. **13**(12): p. 1264-74.

215. Feyen, D.A., et al., Gelatin Microspheres as Vehicle for Cardiac Progenitor Cells Delivery to the Myocardium. Adv Healthc Mater, 2016. **5**(9): p. 1071-9.

216. Cui, X., et al., NIPAM-based Microgel Microenvironment Regulates the Therapeutic Function of Cardiac Stromal Cells. ACS Appl Mater Interfaces, 2018. **10**(44): p. 37783-37796.

217. Ruvinov, E., J. Leor, and S. Cohen, The promotion of myocardial repair by the sequential delivery of IGF-1 and HGF from an injectable alginate biomaterial in a model of acute myocardial infarction. Biomaterials, 2011. **32**(2): p. 565-78.

218. Hoshino, K., et al., Three catheter-based strategies for cardiac delivery of therapeutic gelatin microspheres. Gene Ther, 2006. **13**(18): p. 1320-7.

219. Iwakura, A., et al., Intramyocardial sustained delivery of basic fibroblast growth factor improves angiogenesis and ventricular function in a rat infarct model. Heart Vessels, 2003. **18**(2): p. 93-9.

220. Yamamoto, T., et al., Intramyocardial delivery of basic fibroblast growth factor-impregnated gelatin hydrogel microspheres enhances collateral circulation to infarcted canine myocardium. Jpn Circ J, 2001. **65**(5): p. 439-44.

221. Peng, L., et al., The effect of interfacial tension on droplet formation in flow-focusing microfluidic device. Biomed Microdevices, 2011. **13**(3): p. 559-64.

222. Allazetta, S., T.C. Hausherr, and M.P. Lutolf, Microfluidic synthesis of cell-type-specific artificial extracellular matrix hydrogels. Biomacromolecules, 2013. **14**(4): p. 1122-31.

223. Zhu, P. and L. Wang, Passive and active droplet generation with microfluidics: a review. Lab Chip, 2016. **17**(1): p. 34-75.

224. Christopher, G.F. and S.L. Anna, Microfluidic methods for generating continuous droplet streams - IOPscience. J. Phys. D, 2007. **40**(19).

225. Thorsen, T., et al., Dynamic pattern formation in a vesicle-generating microfluidic device. Phys Rev Lett, 2001. **86**(18): p. 4163-6.

226. Ward, T., et al., Microfluidic flow focusing: drop size and scaling in pressure versus flow-rate-driven pumping. Electrophoresis, 2005. **26**(19): p. 3716-24.

227. Dang, T.D., Y.H. Kim, Kim, G.G., and G.M. Kim, Preparation of monodisperse PEG hydrogel microparticles using a microfluidic flow-focusing device. J. Ind. Eng. Chem., 2012. **18**(4): p. 1308-1313.

228. Layani, M., X. Wang, and S. Magdassi, Novel Materials for 3D Printing by Photopolymerization. Adv Mater, 2018. **30**(41): p. e1706344.

229. Roberts, C.C., et al., Circulation within confined droplets in Hele-Shaw channels. Phys. Fluids, 2014. **26**.

230. Takeuchi, Y., et al., A comparative study of the toxicity of n-pentane, n-hexane, and n-heptane to the peripheral nerve of the rat. Clin Toxicol, 1981. **18**(12): p. 1395-402.

231. Femmer, T., et al., High-Throughput Generation of Emulsions and Microgels in Parallelized Microfluidic Drop-Makers Prepared by Rapid Prototyping. ACS Appl Mater Interfaces, 2015. **7**(23): p. 12635-8.

232. Wagner, J.C., D.I. Adler, and D.N. Fuller, Foreign body granulomata of the lungs due to liquid paraffin. Thorax, 1955. **10**(2): p. 157-70.

233. Henriksen, T.F., J.B. Lovenwald, and S.H. Matzen, [Paraffin oil injection in bodybuilders calls for preventive action]. Ugeskr Laeger, 2010. **172**(3): p. 219-20.

234. Barp, L., et al., Accumulation of mineral oil saturated hydrocarbons (MOSH) in female Fischer 344 rats: Comparison with human data and consequences for risk assessment. Sci Total Environ, 2017. **575**: p. 1263-1278.

235. Goshman, L.M., Clinical Toxicology of Commercial Products, 5th ed. Journal of pharmaceutical sciences., 1985. **74**(10): p. 1139-1139.

236. Cressey, B.D., N. Kumar, and P.L. Scheinman, *Contact allergy to sorbitans: a follow-up study.* Dermatitis, 2012. **23**(4): p. 158-61.

237. McKee, R., et al., Toxicology of n-pentane (CAS no. 109-66-0). J Appl Toxicol, 1998. **18**(6): p. 431-42.

238. Shi, S., et al., A Highly Sensitive Method for the Quantitation of Polysorbate 20 and 80 to Study the Compatibility between Polysorbates and m-Cresol in the Peptide Formulation. Journal of Analytical & Bioanalytical Techniques, 2015. **6**(3): p. 1.

239. Weber, S., et al., Analytical Methods for the Determination of Mineral Oil Saturated Hydrocarbons (MOSH) and Mineral Oil Aromatic Hydrocarbons (MOAH)-A Short Review. Anal Chem Insights, 2018. **13**: p. 1177390118777757.

240. Fukuda, D., et al., Comparison of levels of serum matrix metalloproteinase-9 in patients with acute myocardial infarction versus unstable angina pectoris versus stable angina pectoris. Am J Cardiol, 2006. **97**(2): p. 175-80.

241. Gilbert, P.M., et al., Substrate elasticity regulates skeletal muscle stem cell self-renewal in culture. Science, 2010. **329**(5995): p. 1078-81.

242. DeCoux, A., et al., Myocardial matrix metalloproteinase-2: inside out and upside down. J Mol Cell Cardiol, 2014. **77**: p. 64-72.

243. PicoQuant. *Absolute Diffusion Coefficients: Compilation of Reference Data for FCS Calibration | PicoQuant*. 2019; Available from: https://www.picoquant.com/scientific/technical-and-application-notes/category/technical_notes_techniques_and_methods/details/absolute-diffusion-coefficients-compilation-reference-fcs-data.

244. Muller, P., P. Schwille, and T. Weidemann, PyCorrFit-generic data evaluation for fluorescence correlation spectroscopy. Bioinformatics, 2014. **30**(17): p. 2532-3.

245. Troiber, C., et al., Comparison of four different particle sizing methods for siRNA polyplex characterization. Eur J Pharm Biopharm, 2013. **84**(2): p. 255-64.

246. Mäde, V., S. Els-Heindl, and A.G. Beck-Sickinger, Automated solid-phase peptide synthesis to obtain therapeutic peptides. Beilstein J Org Chem, 2014. **10**: p. 1197-212.

247. Adan, A., Y. Kiraz, and Y. Baran, Cell Proliferation and Cytotoxicity Assays. Curr Pharm Biotechnol, 2016. **17**(14): p. 1213-1221.

248. Lock, A., J. Cornish, and D.S. Musson, The Role of In Vitro Immune Response Assessment for Biomaterials, in J Funct Biomater. 2019.

249. Smith, R., K.L. Wright, and L. Ashton, Raman spectroscopy: an evolving technique for live cell studies. Analyst, 2016. **141**(12): p. 3590-600.

250. Costa Verdera, H., et al., Cellular uptake of extracellular vesicles is mediated by clathrin-independent endocytosis and macropinocytosis. J Control Release, 2017. **266**: p. 100-108.

251. Ibrahim, M., et al., Characterization of the Foreign Body Response to Common Surgical Biomaterials in a Murine Model. Eur J Plast Surg, 2017. **40**(5): p. 383-392.

252. Nizamudeen, Z., et al., Rapid and accurate analysis of stem cell-derived extracellular vesicles with super resolution microscopy and live imaging. Biochim Biophys Acta Mol Cell Res, 2018. **1865**(12): p. 1891-1900.